



Long-range angular correlations of charged particles in high multiplicity e^+e^- collisions using archived data from the ALEPH detector at LEP

Anthony Badea, Austin Baty, Gian Michele Innocenti, Yen-Jie Lee,
Christopher McGinn, Bibek Pandit, Michael Peters, and Jesse Thaler

Massachusetts Institute of Technology

Paoti Chang and Tzu-An Sheng

National Taiwan University

Marcello Maggi

Universita degli Studi di Bari

(Dated: March 9, 2018)

Abstract

First results on two-particle angular correlations for charged particles emitted in e^+e^- collisions using 730 pb^{-1} of data collected between 91 and 209 GeV with the ALEPH detector at LEP are presented. With the archived data, the correlation functions are studied over a broad range of pseudorapidity η (rapidity y) and azimuthal angle ϕ with respect to the electron-positron beam axis, the event thrust axis and a dijet axis. Short-range correlations in $\Delta\eta$ (Δy), which are studied with e^+e^- annihilations which reveal jet-like correlations. Long-range azimuthal correlations are studied differentially as a function of charged particle multiplicity. Those results are compared to event generators and are complementary to the particle correlation analyses in high multiplicity proton-proton, proton-nucleus and nucleus-nucleus collisions at the RHIC and the LHC.

CONTENTS

I. Introduction	3
II. Data Sample	4
III. Data Quality Checks	4
A. LEP1 vs LEP1 Monte-Carlo	5
B. LEP2 vs LEP2 Monte-Carlo	13
C. LEP1 vs LEP2 (event energy > 100GeV)	21
IV. Multiplicity Distributions	29
V. Analysis	32
VI. Thrust and sphericity axes	32
VII. Winner-Take-All Axis	34
VIII. Event Selection	34
IX. Thrust distribution	34
X. Two-Particle Correlation Function	35
A. Analysis for 2018.01.26 production	38
B. Analysis for 2018.02.XX production	56
XI. Systematical Uncertainties	56
XII. Summary	56
XIII. Appendix	56
A. Cross-check analysis with independent macros	56
B. Comparison of Raw Spectra	64
C. Raw data	65
References	73

I. INTRODUCTION

This analysis note presents the measurements of two-particle angular correlations of charged hadrons produced in e^+e^- collisions as a function of charged hadron multiplicity, using 730 pb^{-1} of archived data collected between 91 and 209 GeV with the ALEPH detector at LEP. Two-particle correlations in high-energy collisions provide valuable information for characterizing Quantum Chromodynamics and have been studied previously for a broad range of collision energies in proton-proton (pp) [1], proton-nucleus (pA) [2–4], and nucleus-nucleus (AA) [5, 6] collisions. Such measurements can elucidate the underlying mechanism of particle production and reveal possible collective effects resulting from the high particle densities accessible in these collisions.

Studies of two-particle angular correlations in pp, pA and AA collisions are typically performed using two-dimensional $\Delta\eta - \Delta\phi$ correlation functions, where $\Delta\phi$ is the difference in the azimuthal angle ϕ between the two particles and $\Delta\eta$ is the difference in pseudorapidity $\eta = -\ln(\tan(\theta/2))$. The polar angle θ is defined relative to the counterclockwise hadron beam direction.

Of particular interest in studies of collective effects is the long-range (large $|\Delta\eta|$) structure of the two-particle correlation functions. In this region, the function is less susceptible to other known sources of correlations such as resonance decays and fragmentation function of energetic jets. Measurements in high-energy AA collisions have shown significant modification of the long-range structure compared with minimum-bias pp collisions, over a very wide range of collision energies [7–10]. The long-range correlations are commonly interpreted as a consequence of the hydrodynamical flow of the produced strongly interacting medium [11] and usually characterized by the Fourier components of the azimuthal particle distributions. The extraction of the second and third Fourier components, usually referred to as elliptic and triangular flow, is of great interest because it is closely related to initial collision geometry and its fluctuation [12]. Those measurements allow the extraction of the fundamental transport properties of the medium using hydrodynamic models.

Recently, measurements in pp [1] and pPb collisions [2–4] have revealed the emergence of long-range, near-side ($\Delta\phi \sim 0$) correlations in the selection of collisions with very high number of final state particles. This “ridge-like” correlation has inspired a large variety of theoretical models [13, 14]. The physical origin of the phenomenon is not yet fully

understood. Moreover, it was found that the elliptic flow signal exists even at the lowest nucleon-nucleon center-of-mass energy of 7.7 GeV in AA collisions at the Relativistic Heavy Ion Collider [15].

Due to the complexity of the hadron-hadron collisions, possible initial state correlations of the partons, such as those arise from color-glass condensate [16, 17], could complicate the interpretation of the pp and pA data. Studies of high multiplicity e^+e^- collision, where the initial kinematics of the collisions are well-controlled, could bring significant insights about the observed phenomenon. These measurements will also enable a direct comparison between different collision systems for the first time. The studies of ridge signal in e^+e^- collisions will bring significant impact to the field of relativistic heavy ion collisions, either change completely the interpretation of the ridge in pp, pA and AA collisions if a significant signal is observed, or serve as an important reference for the final state effect observed in high multiplicity hadron-hadron scatterings if no long-range correlation signal was detected.

With the archived data from ALEPH collaboration, the correlation functions are studied over a broad range of pseudorapidity η (rapidity y) and azimuthal angle ϕ with respect to the electron-positron beam axis. In addition, the correlation functions are also studied using azimuthal and polar angles calculated with respect to the event thrust axis and a dijet axis in order to follow the direction of the extending color strings.

II. THE ALEPH DETECTOR

III. DATA SAMPLE

The ALEPH archived data used in this analysis will be documented in this section, which include both LEP1 and LEP2 period.

IV. DATA QUALITY CHECKS

This section documents the basic data quality checks for ALEPH archived data collected in the LEP1 and LEP2 period. In additional to the raw spectra from the data, jet and particle spectra are compared to the predictions from PYTHIA8 event generator (Version 8.230 Default Tune).

A. LEP1 vs LEP1 Monte-Carlo

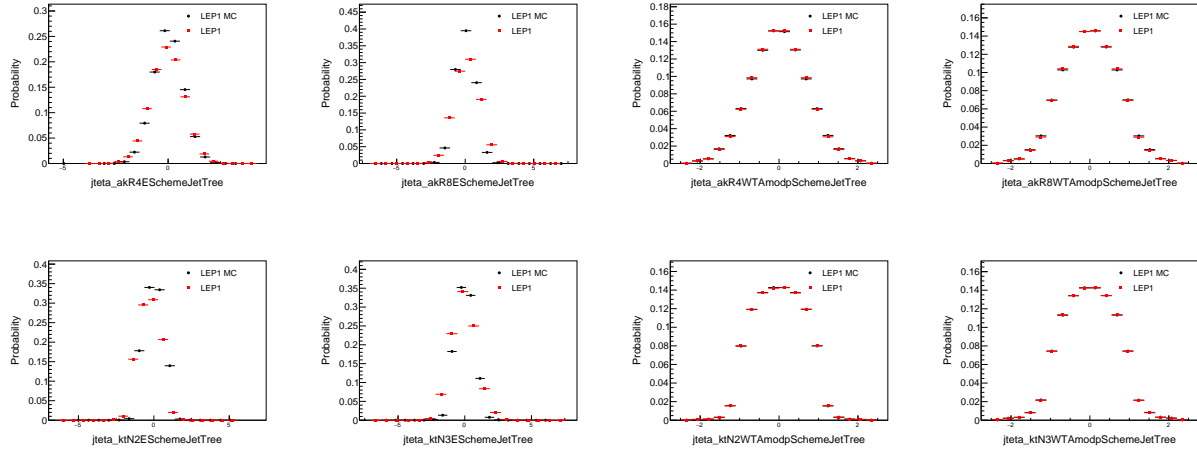


FIG. 1: LEP1 vs LEP1 MC Jet η distributions. Top row: anti- k_t , left to right: $R = 0.4$, E scheme; $R = 0.8$, E scheme; $R = 0.4$, WTA mod p scheme; $R = 0.8$, WTA mod p scheme. Bottom row: k_t , left to right: $N = 2$, E scheme; $N = 3$, E scheme; $N = 2$, WTA mod p scheme; $N = 3$; WTA mod p scheme.

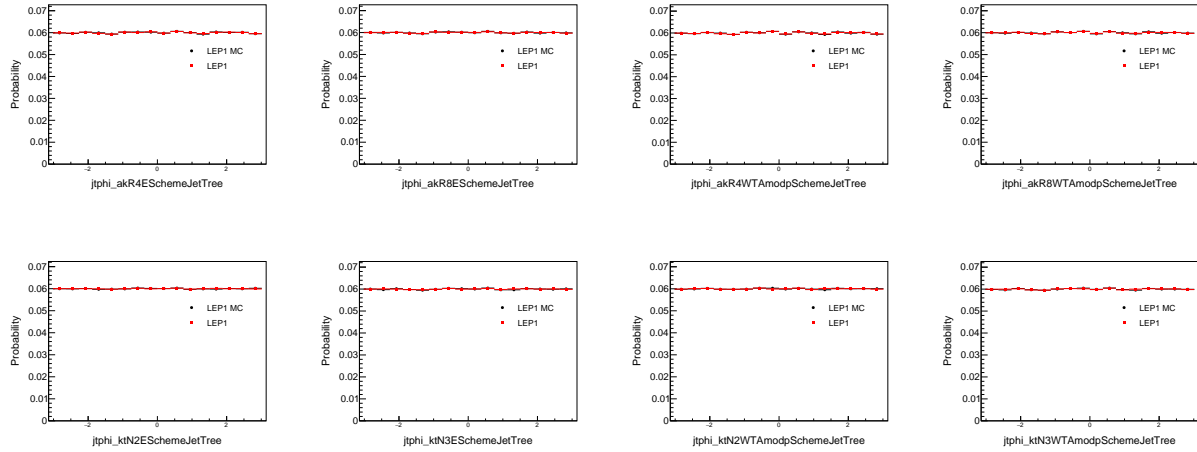


FIG. 2: LEP1 vs LEP1 MC Jet ϕ distributions. Top row: anti- k_t , left to right: $R = 0.4$, E scheme; $R = 0.8$, E scheme; $R = 0.4$, WTA mod p scheme; $R = 0.8$, WTA mod p scheme. Bottom row: k_t , left to right: $N = 2$, E scheme; $N = 3$, E scheme; $N = 2$, WTA mod p scheme; $N = 3$; WTA mod p scheme.

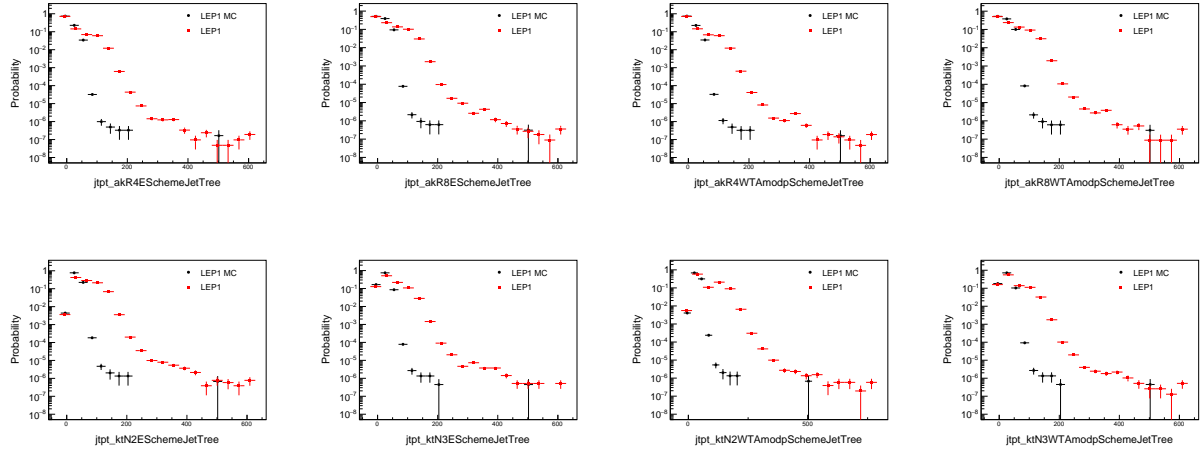


FIG. 3: LEP1 vs LEP1 MC Jet p_t distributions. Top row: anti- k_t , left to right: $R = 0.4$, E scheme; $R = 0.8$, E scheme; $R = 0.4$, WTA mod p scheme; $R = 0.8$, WTA mod p scheme. Bottom row: k_t , left to right: $N = 2$, E scheme; $N = 3$, E scheme; $N = 2$, WTA mod p scheme; $N = 3$; WTA mod p scheme.

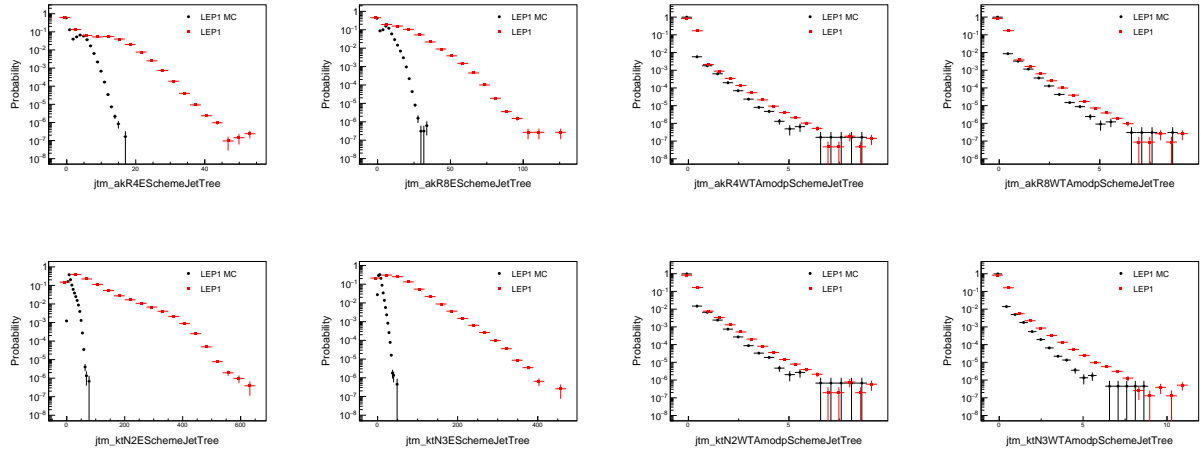


FIG. 4: LEP1 vs LEP1 MC Jet mass distributions. Top row: anti- k_t , left to right: $R = 0.4$, E scheme; $R = 0.8$, E scheme; $R = 0.4$, WTA mod p scheme; $R = 0.8$, WTA mod p scheme. Bottom row: k_t , left to right: $N = 2$, E scheme; $N = 3$, E scheme; $N = 2$, WTA mod p scheme; $N = 3$; WTA mod p scheme.

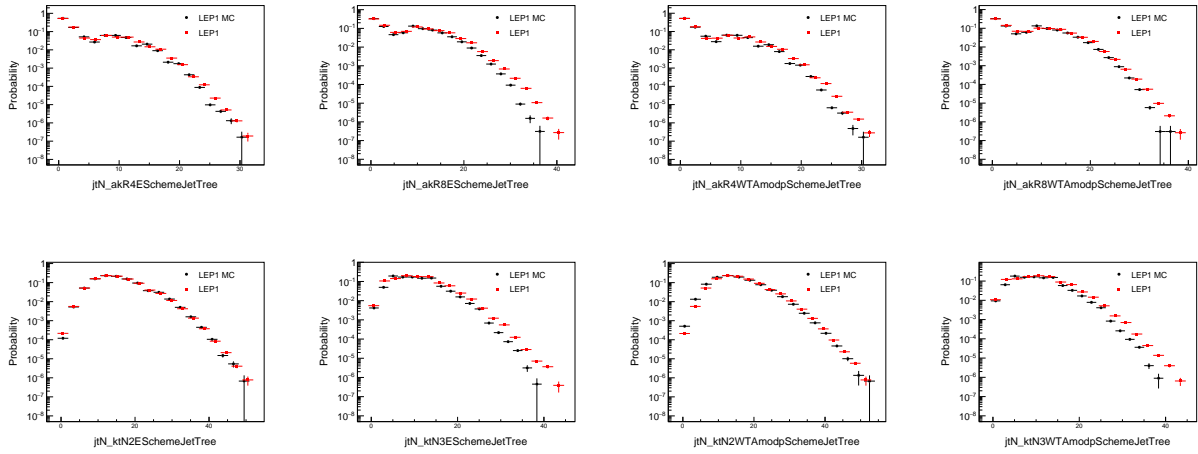


FIG. 5: LEP1 vs LEP1 MC Jet N distributions. Top row: anti- k_t , left to right: $R = 0.4$, E scheme; $R = 0.8$, E scheme; $R = 0.4$, WTA mod p scheme; $R = 0.8$, WTA mod p scheme. Bottom row: k_t , left to right: $N = 2$, E scheme; $N = 3$, E scheme; $N = 2$, WTA mod p scheme; $N = 3$; WTA mod p scheme.

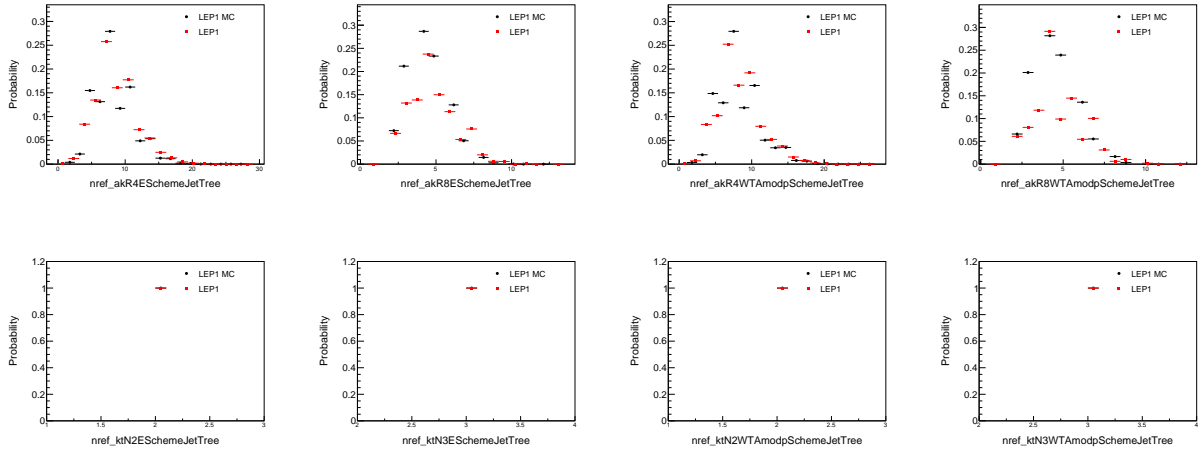


FIG. 6: LEP1 vs LEP1 MC Jet nref distributions. Top row: anti- k_t , left to right: $R = 0.4$, E scheme; $R = 0.8$, E scheme; $R = 0.4$, WTA mod p scheme; $R = 0.8$, WTA mod p scheme. Bottom row: k_t , left to right: $N = 2$, E scheme; $N = 3$, E scheme; $N = 2$, WTA mod p scheme; $N = 3$; WTA mod p scheme.

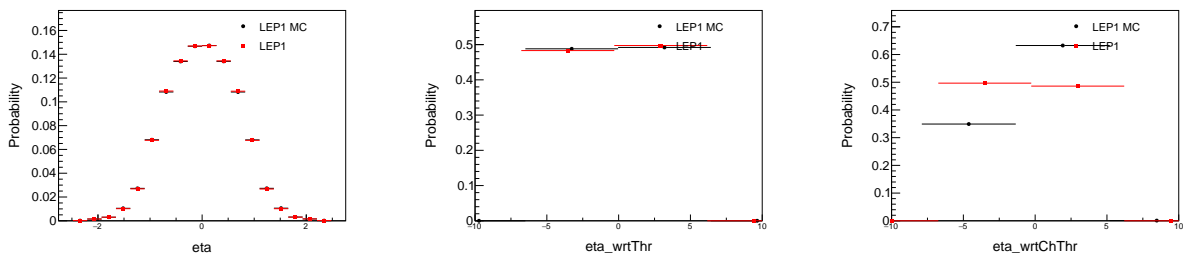


FIG. 7: LEP1 vs LEP1 MC η distributions. Left to right: η ; η with respect to thrust axis; η with respect to charged thrust axis.

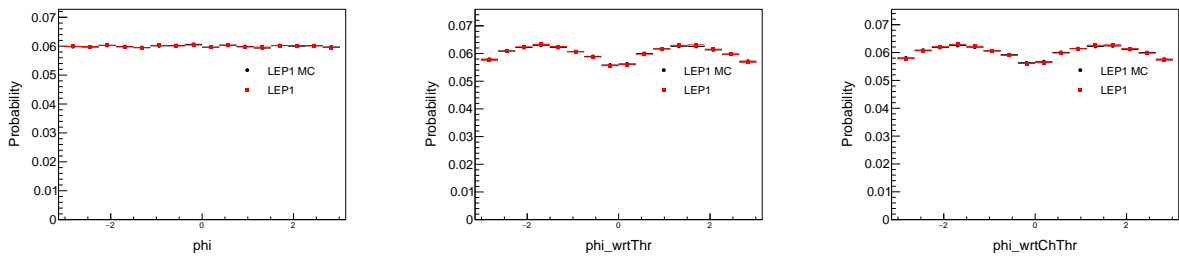


FIG. 8: LEP1 vs LEP1 MC ϕ distributions. Left to right: ϕ ; ϕ with respect to thrust axis; ϕ with respect to charged thrust axis.

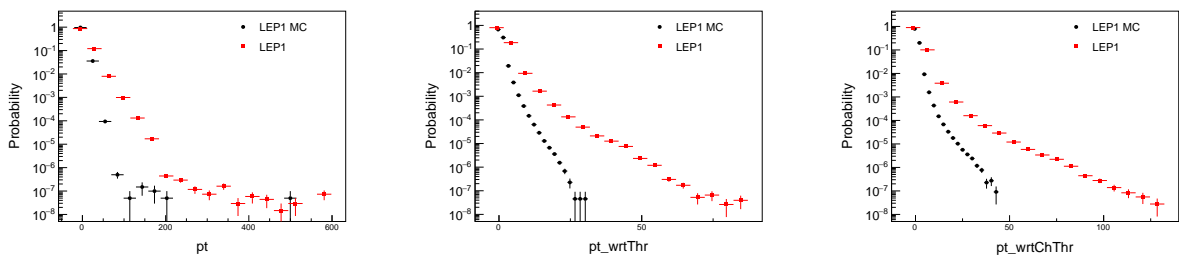


FIG. 9: LEP1 vs LEP1 MC p_t distributions. Left to right: p_t ; p_t with respect to thrust axis; p_t with respect to charged thrust axis.

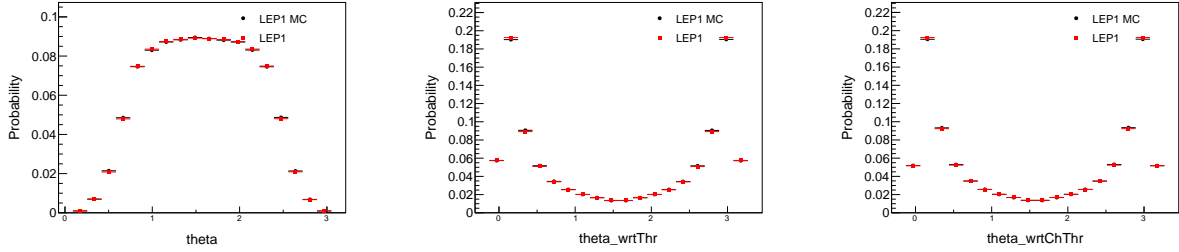


FIG. 10: LEP1 vs LEP1 MC θ distributions. Left to right: θ ; θ with respect to thrust axis; θ with respect to charged thrust axis.

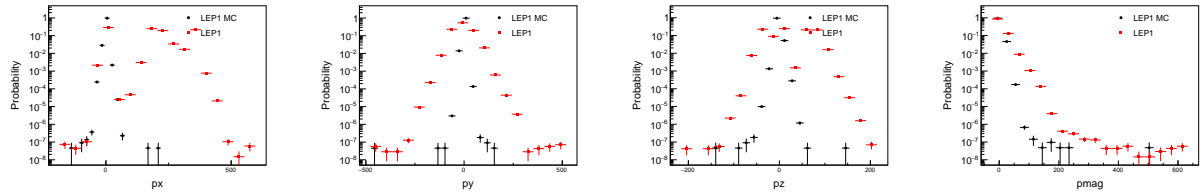


FIG. 11: LEP1 vs LEP1 MC p_x , p_y , p_z , and $|\vec{p}|$ distributions.

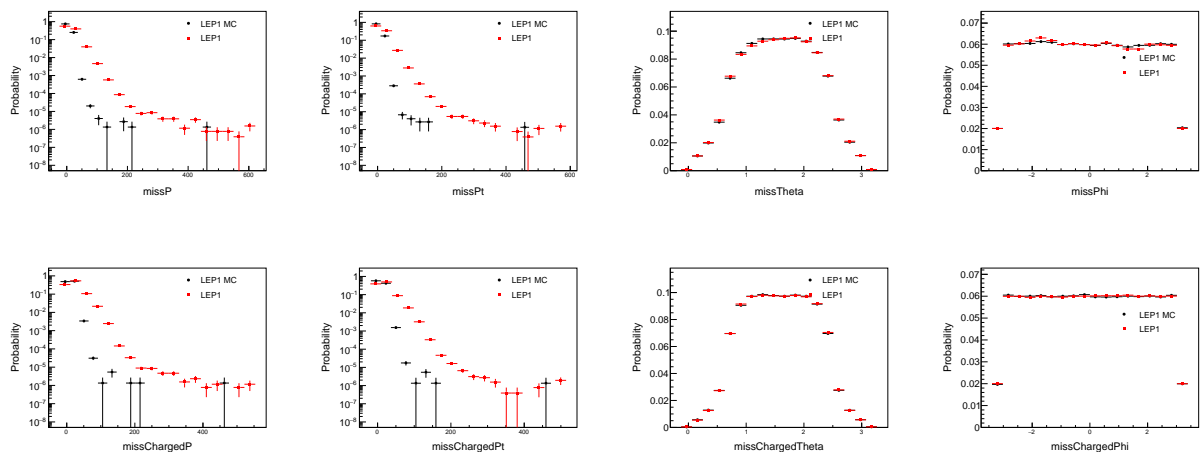


FIG. 12: LEP1 vs LEP1 MC missing quantities distribution. Left to right: missing P ; missing p_t ; missing θ ; missing ϕ . Top to bottom: All; charged.

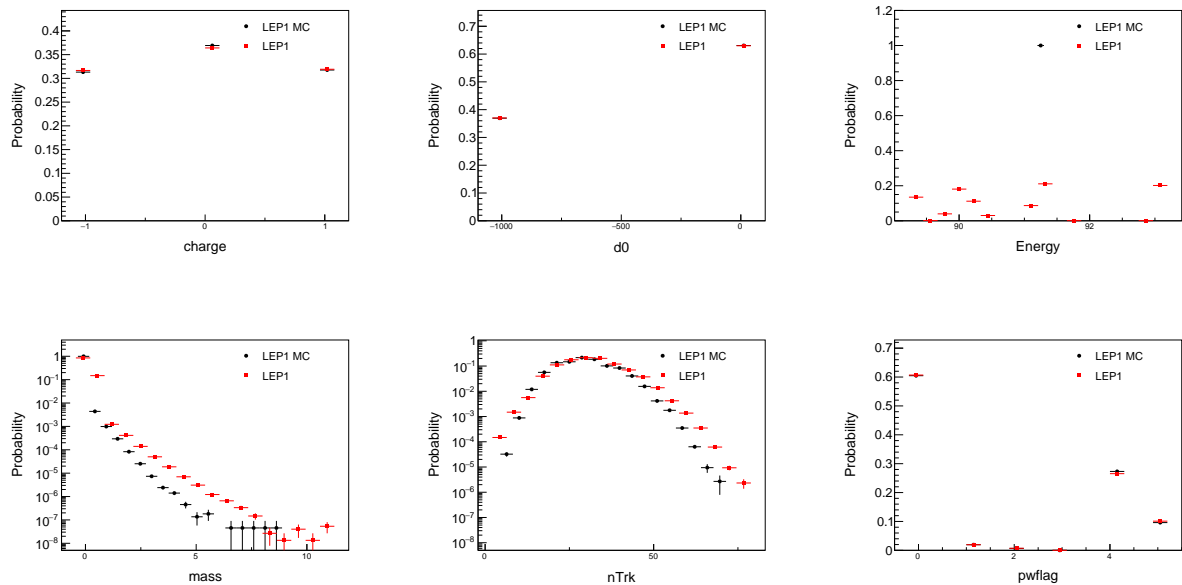


FIG. 13: Left to right: Top row: LEP1 vs LEP1 MC charge, d_0 , and energy distributions. Bottom row: LEP1MC mass, particle multiplicity, and pwflag distributions.

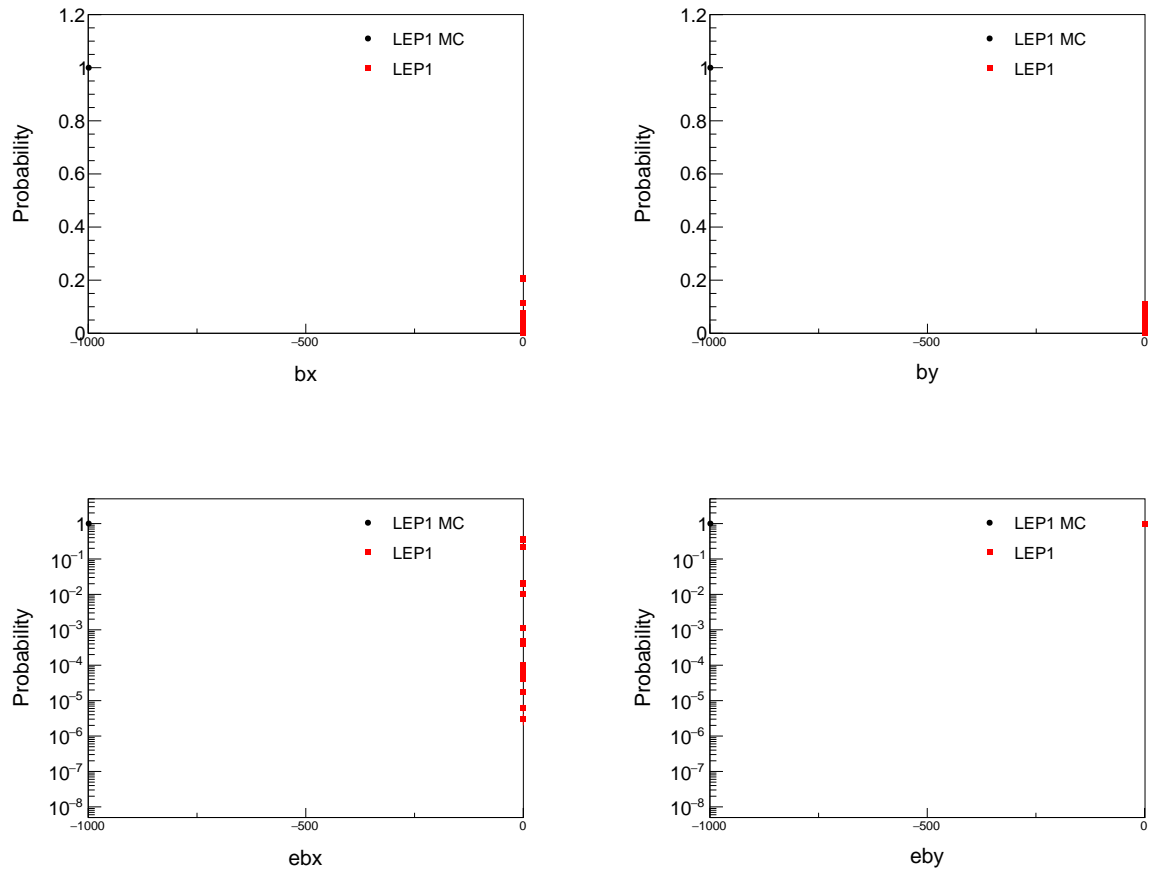


FIG. 14: Top row: LEP1 vs LEP1 MC beamspot x and y . Bottom row: Error in beamspot x and y .

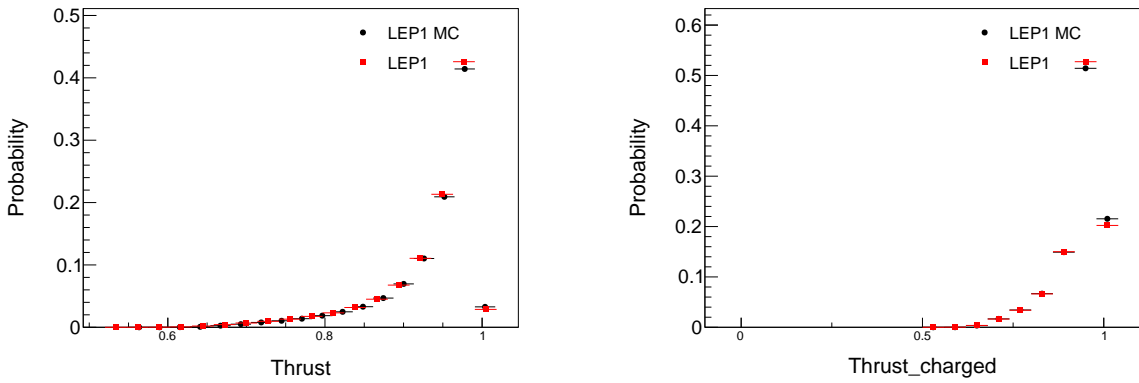


FIG. 15: Left: LEP1 vs LEP1 MC thrust distribution. Right: LEP1 vs LEP1 MC charged thrust distribution.

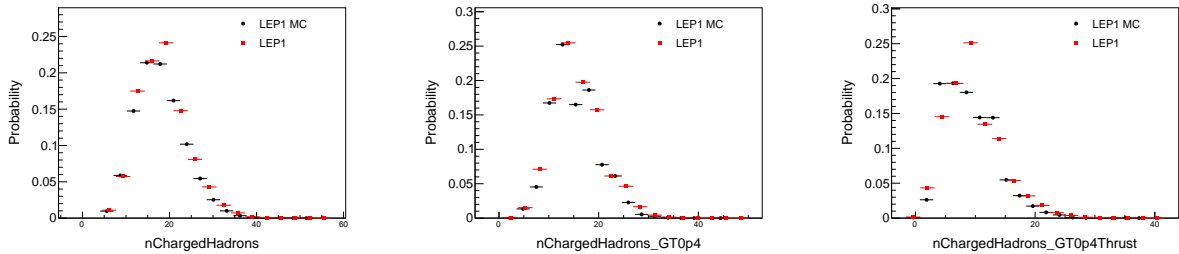


FIG. 16: LEP1 vs LEP1 MC charged hadron multiplicity distributions. Left to right: charged hadron multiplicity; charged hadron multiplicity (GT0p4); charged hadron multiplicity (GT0p4Thrust).

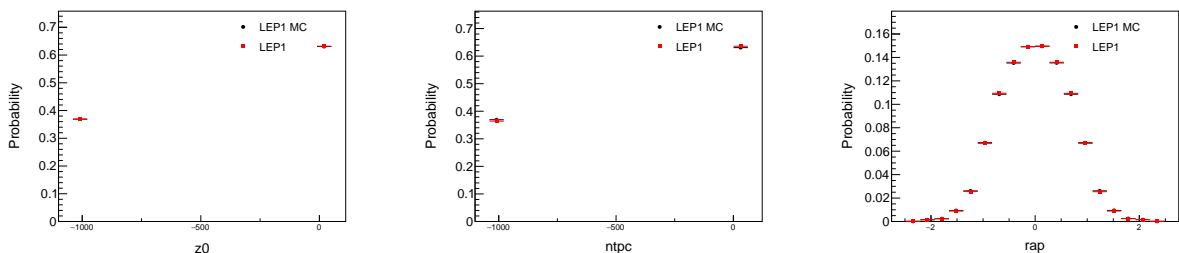


FIG. 17: Left: LEP1 vs LEP1 MC z_0 distribution. Center: LEP1 vs LEP1 MC TPC hits distribution. Right: LEP1MC rapidity distribution.

B. LEP2 vs LEP2 Monte-Carlo

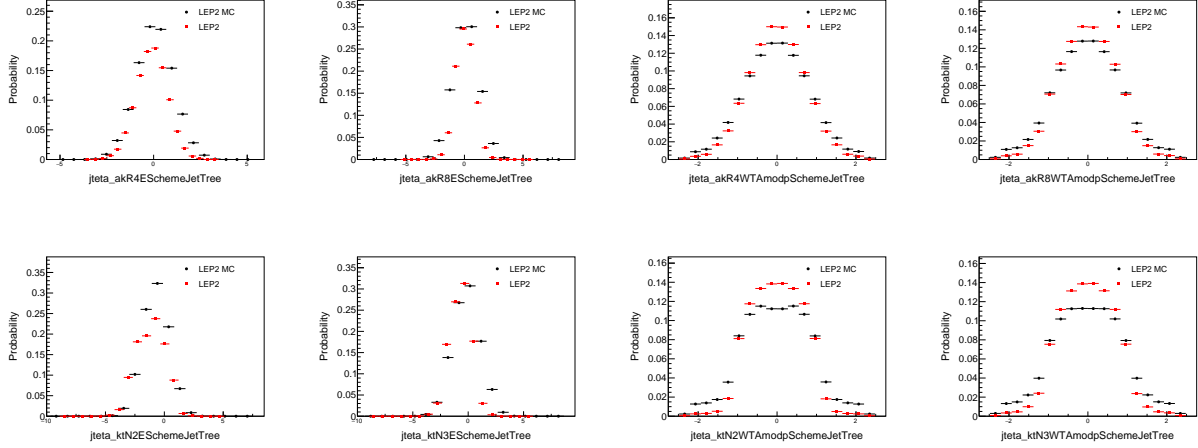


FIG. 18: LEP2 vs LEP2 MC Jet η distributions. Top row: anti- k_t , left to right: $R = 0.4$, E scheme; $R = 0.8$, E scheme; $R = 0.4$, WTA mod p scheme; $R = 0.8$, WTA mod p scheme. Bottom row: k_t , left to right: $N = 2$, E scheme; $N = 3$, E scheme; $N = 2$, WTA mod p scheme; $N = 3$; WTA mod p scheme.

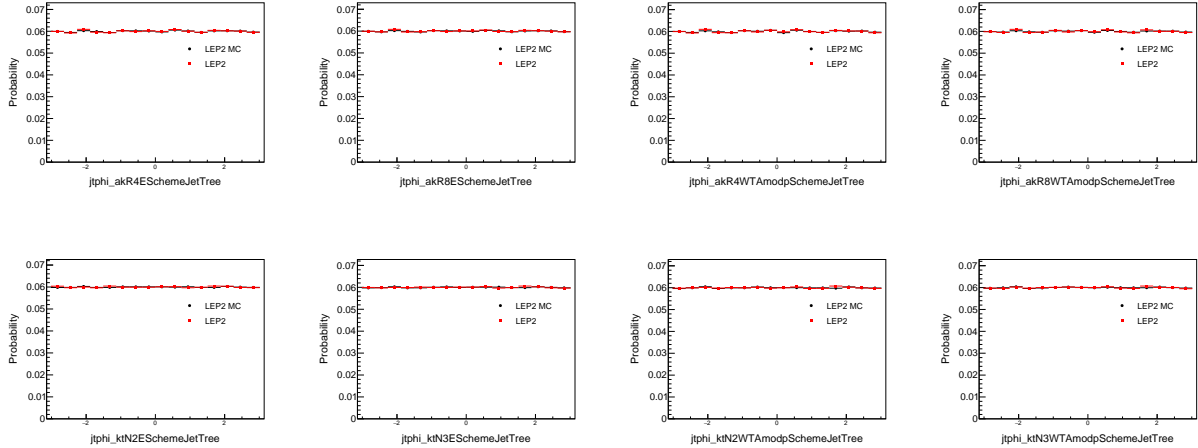


FIG. 19: LEP2 vs LEP2 MC Jet ϕ distributions. Top row: anti- k_t , left to right: $R = 0.4$, E scheme; $R = 0.8$, E scheme; $R = 0.4$, WTA mod p scheme; $R = 0.8$, WTA mod p scheme. Bottom row: k_t , left to right: $N = 2$, E scheme; $N = 3$, E scheme; $N = 2$, WTA mod p scheme; $N = 3$; WTA mod p scheme.

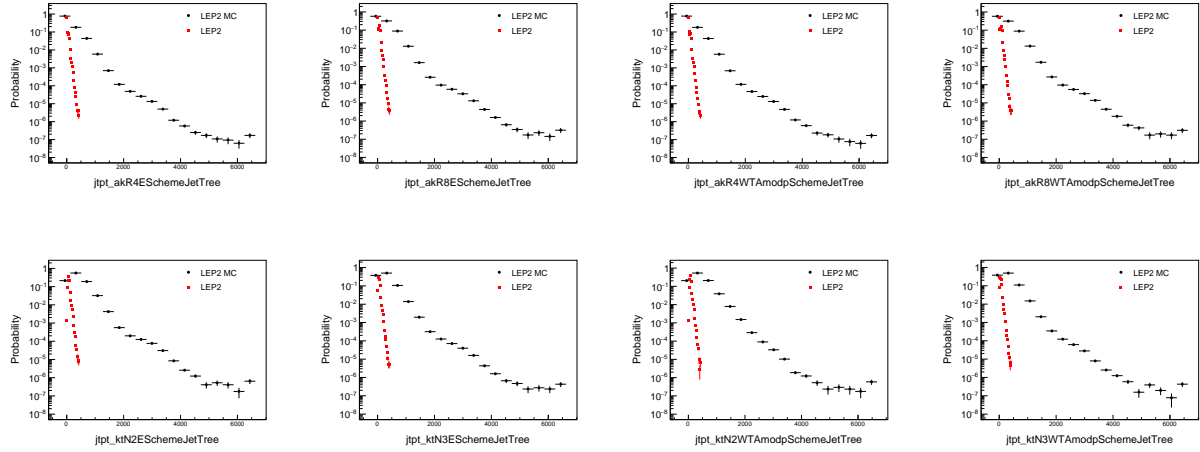


FIG. 20: LEP2 vs LEP2 MC Jet p_t distributions. Top row: anti- k_t , left to right: $R = 0.4$, E scheme; $R = 0.8$, E scheme; $R = 0.4$, WTA mod p scheme; $R = 0.8$, WTA mod p scheme. Bottom row: k_t , left to right: $N = 2$, E scheme; $N = 3$, E scheme; $N = 2$, WTA mod p scheme; $N = 3$; WTA mod p scheme.

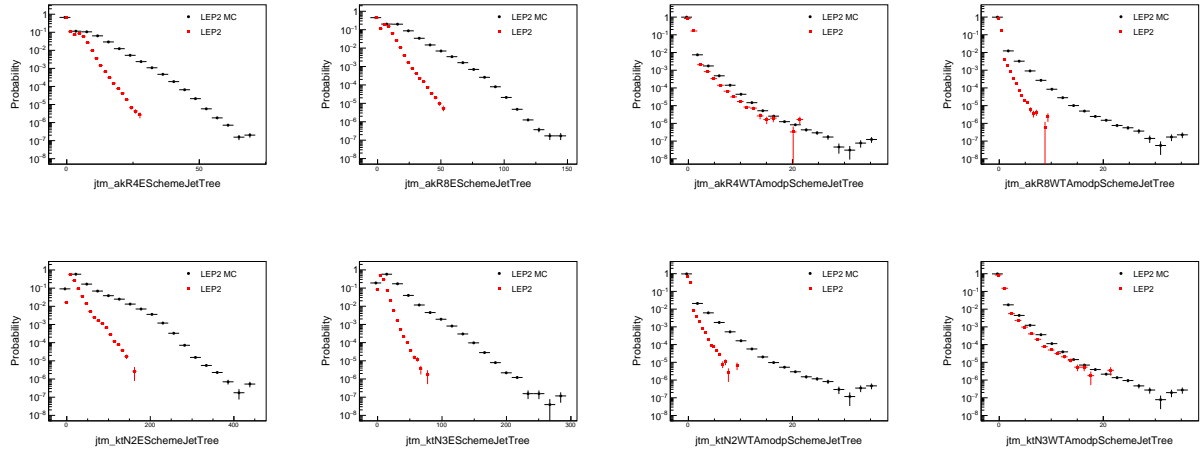


FIG. 21: LEP2 vs LEP2 MC Jet mass distributions. Top row: anti- k_t , left to right: $R = 0.4$, E scheme; $R = 0.8$, E scheme; $R = 0.4$, WTA mod p scheme; $R = 0.8$, WTA mod p scheme. Bottom row: k_t , left to right: $N = 2$, E scheme; $N = 3$, E scheme; $N = 2$, WTA mod p scheme; $N = 3$; WTA mod p scheme.

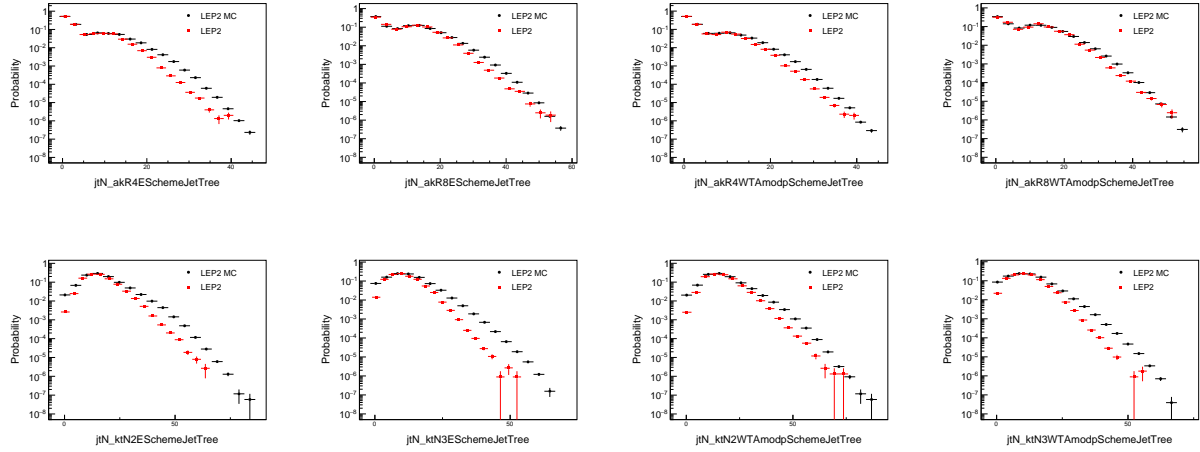


FIG. 22: LEP2 vs LEP2 MC Jet N distributions. Top row: anti- k_t , left to right: $R = 0.4$, E scheme; $R = 0.8$, E scheme; $R = 0.4$, WTA mod p scheme; $R = 0.8$, WTA mod p scheme. Bottom row: k_t , left to right: $N = 2$, E scheme; $N = 3$, E scheme; $N = 2$, WTA mod p scheme; $N = 3$; WTA mod p scheme.

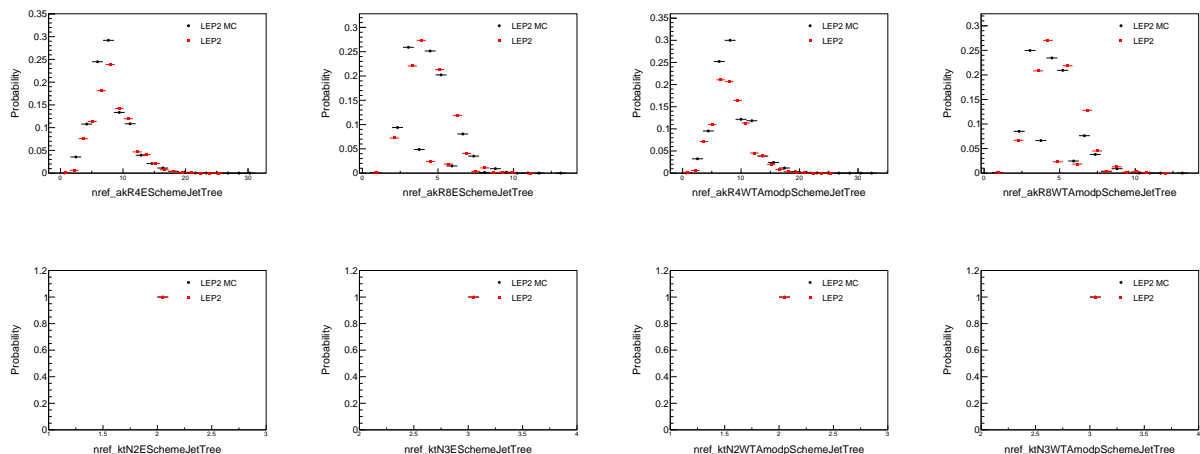


FIG. 23: LEP2 vs LEP2 MC Jet nref distributions. Top row: anti- k_t , left to right: $R = 0.4$, E scheme; $R = 0.8$, E scheme; $R = 0.4$, WTA mod p scheme; $R = 0.8$, WTA mod p scheme. Bottom row: k_t , left to right: $N = 2$, E scheme; $N = 3$, E scheme; $N = 2$, WTA mod p scheme; $N = 3$; WTA mod p scheme.

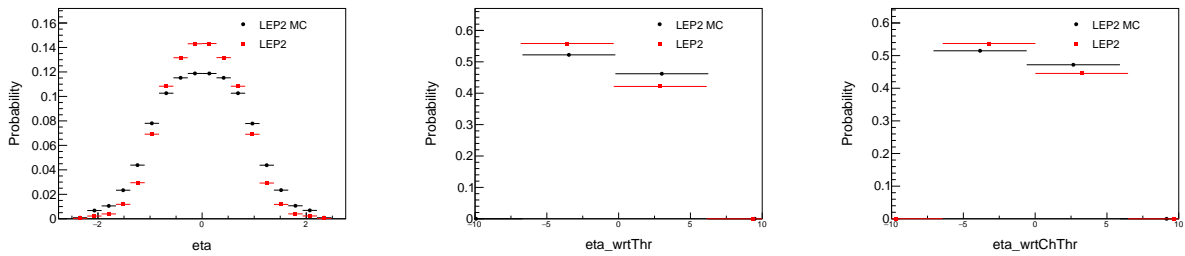


FIG. 24: LEP2 vs LEP2 MC η distributions. Left to right: η ; η with respect to thrust axis; η with respect to charged thrust axis.

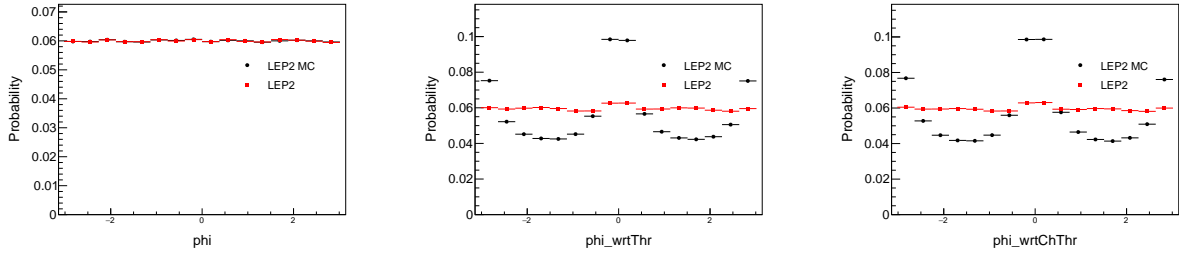


FIG. 25: LEP2 vs LEP2 MC ϕ distributions. Left to right: ϕ ; ϕ with respect to thrust axis; ϕ with respect to charged thrust axis.

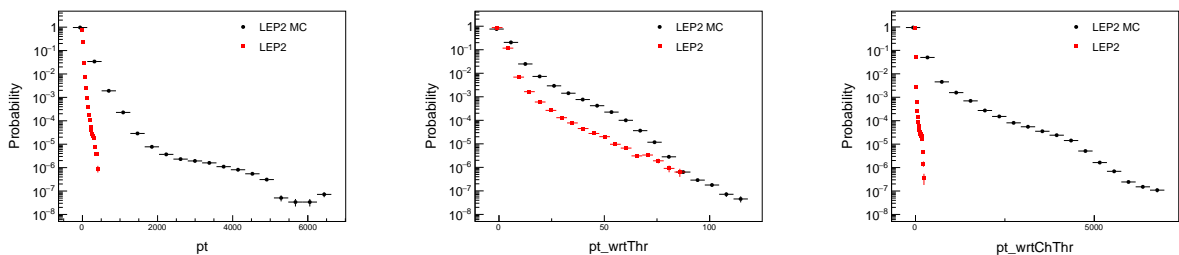


FIG. 26: LEP2 vs LEP2 MC p_t distributions. Left to right: p_t ; p_t with respect to thrust axis; p_t with respect to charged thrust axis.

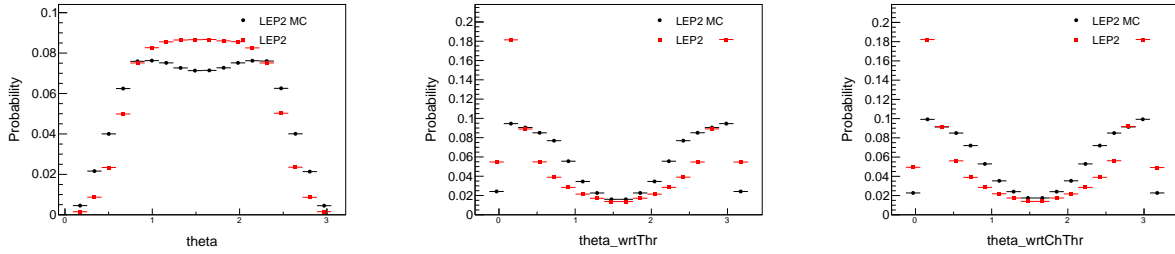


FIG. 27: LEP2 vs LEP2 MC θ distributions. Left to right: θ ; θ with respect to thrust axis; θ with respect to charged thrust axis.

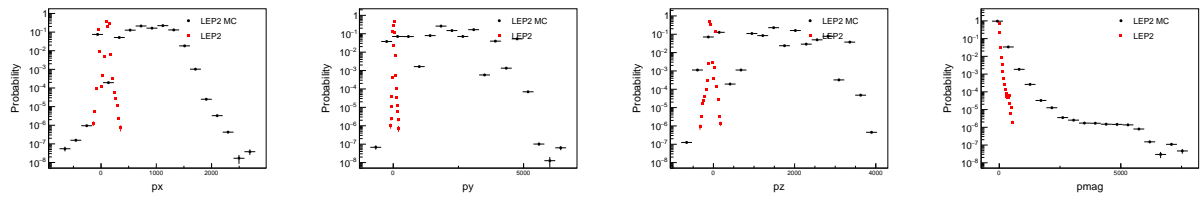


FIG. 28: LEP2 vs LEP2 MC p_x , p_y , p_z , and $|\vec{p}|$ distributions.

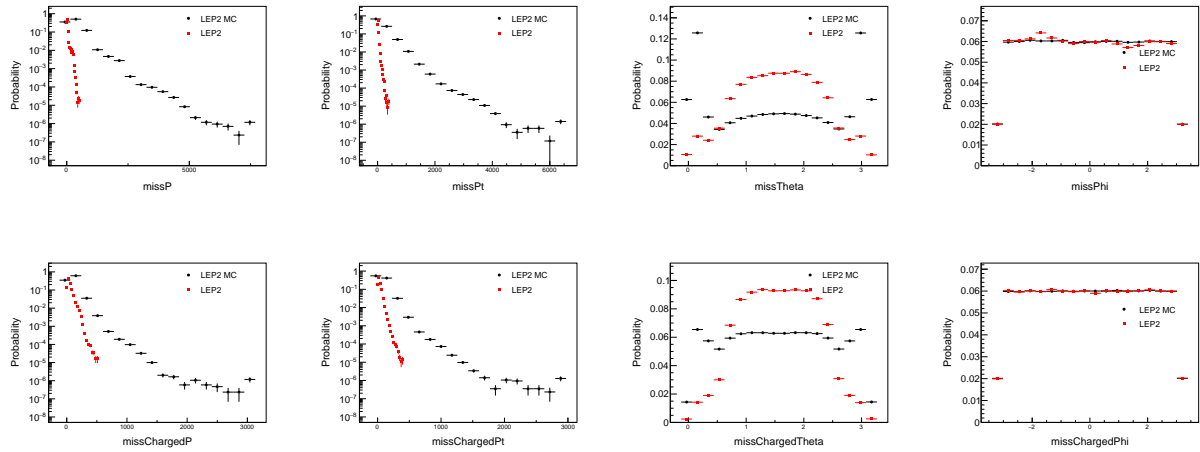


FIG. 29: LEP2 vs LEP2 MC missing quantities distribution. Left to right: missing P ; missing p_t ; missing θ ; missing ϕ . Top to bottom: All; charged.

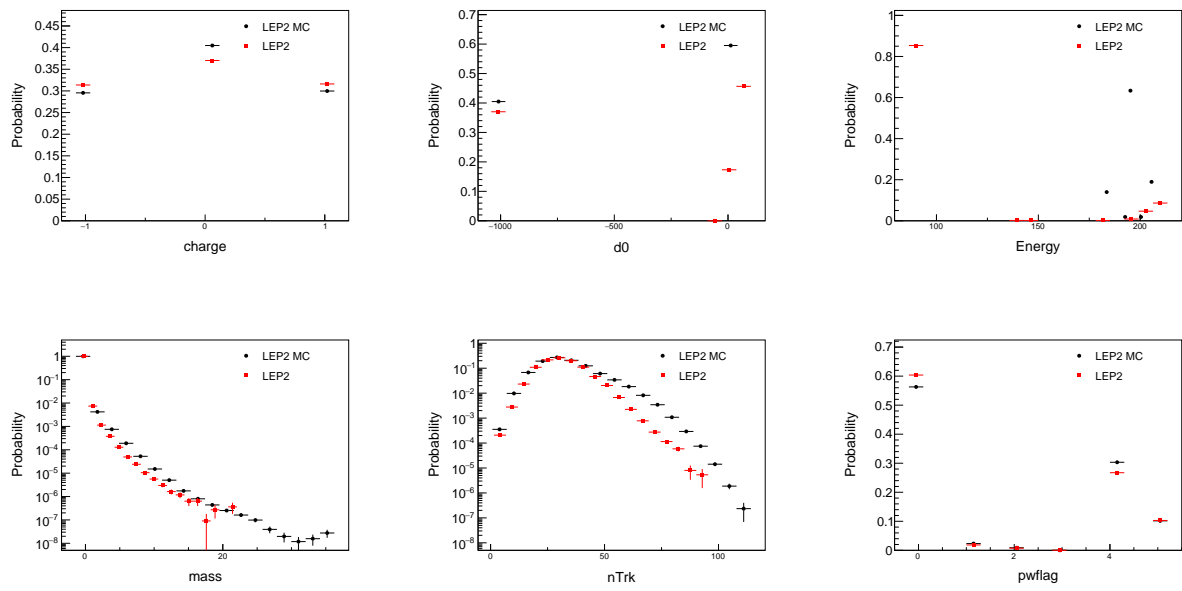


FIG. 30: Left to right: Top row: LEP2 vs LEP2 MC charge, d_0 , and energy distributions. Bottom row: LEP2MC mass, particle multiplicity, and pwflag distributions.

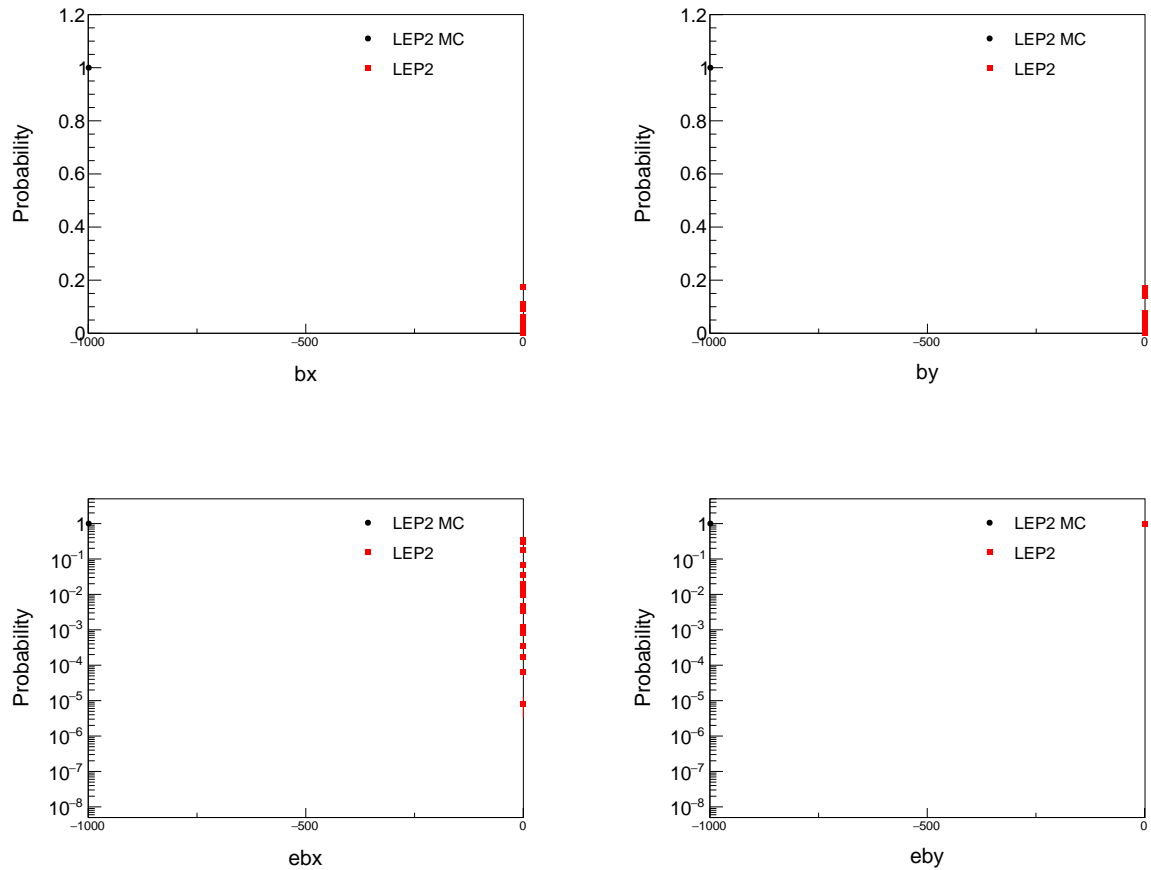


FIG. 31: Top row: LEP2 vs LEP2 MC beamspot x and y . Bottom row: Error in beamspot x and y .

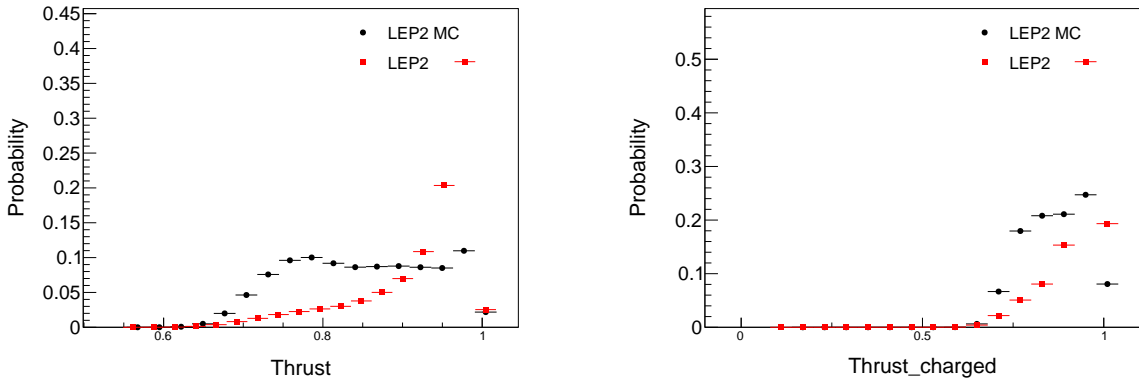


FIG. 32: Left: LEP2 vs LEP2 MC thrust distribution. Right: LEP2 vs LEP2 MC charged thrust distribution.

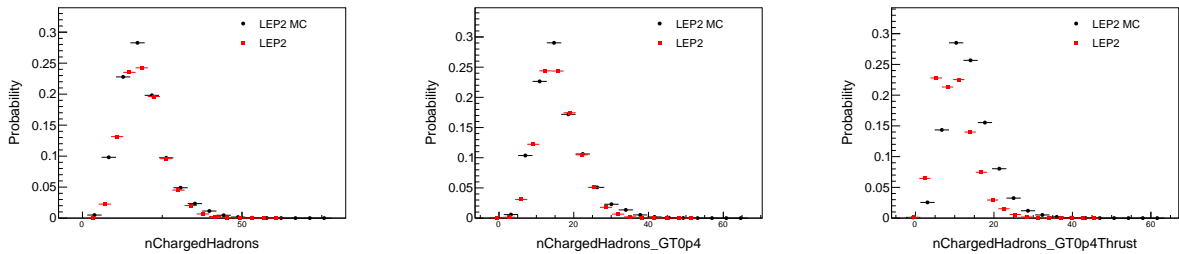


FIG. 33: LEP2 vs LEP2 MC charged hadron multiplicity distributions. Left to right: charged hadron multiplicity; charged hadron multiplicity (GT0p4); charged hadron multiplicity (GT0p4Thrust).

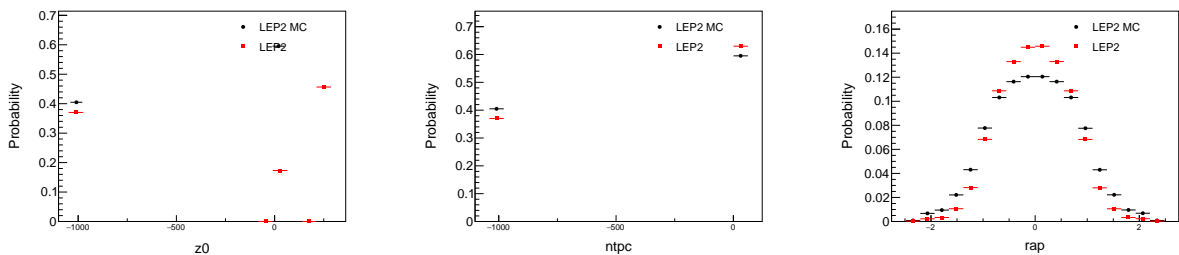


FIG. 34: Left: LEP2 vs LEP2 MC z_0 distribution. Center: LEP2 vs LEP2 MC TPC hits distribution. Right: LEP2MC rapidity distribution.

C. LEP1 vs LEP2 (event energy > 100GeV)

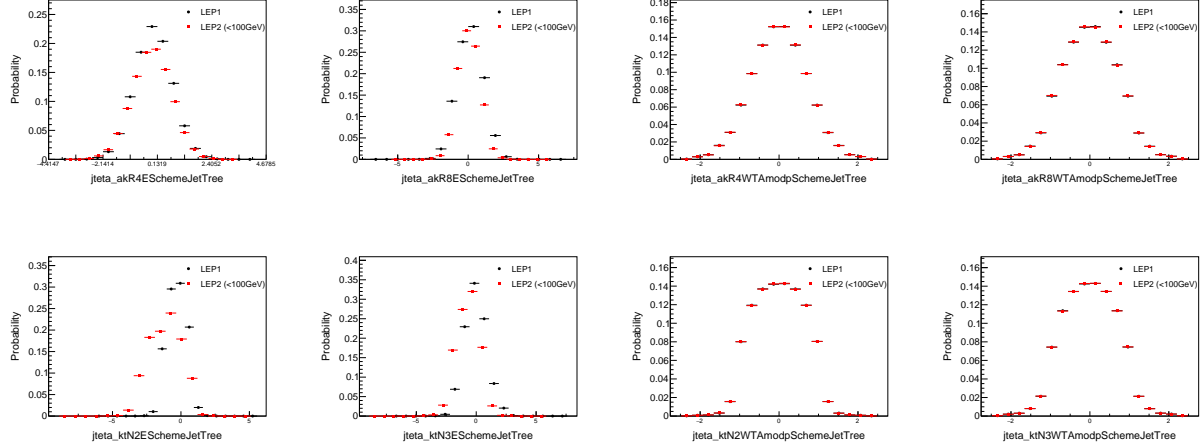


FIG. 35: LEP1 vs LEP2 (event energy > 100GeV) Jet η distributions. Top row: anti- k_t , left to right: $R = 0.4$, E scheme; $R = 0.8$, E scheme; $R = 0.4$, WTA mod p scheme; $R = 0.8$, WTA mod p scheme. Bottom row: k_t , left to right: $N = 2$, E scheme; $N = 3$, E scheme; $N = 2$, WTA mod p scheme; $N = 3$; WTA mod p scheme.

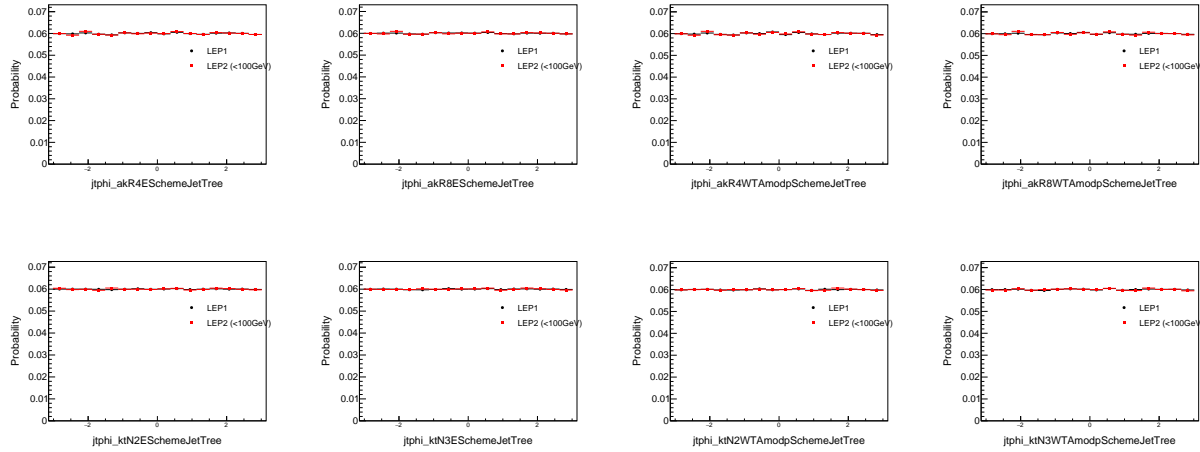


FIG. 36: LEP1 vs LEP2 (event energy > 100GeV) Jet ϕ distributions. Top row: anti- k_t , left to right: $R = 0.4$, E scheme; $R = 0.8$, E scheme; $R = 0.4$, WTA mod p scheme; $R = 0.8$, WTA mod p scheme. Bottom row: k_t , left to right: $N = 2$, E scheme; $N = 3$, E scheme; $N = 2$, WTA mod p scheme; $N = 3$; WTA mod p scheme.

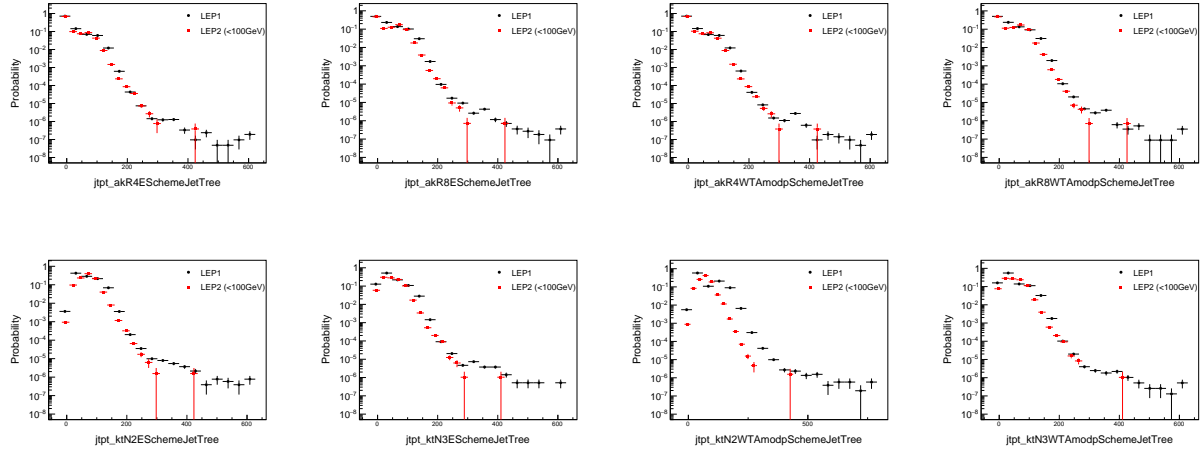


FIG. 37: LEP1 vs LEP2 (event energy $> 100\text{GeV}$) Jet p_t distributions. Top row: anti- k_t , left to right: $R = 0.4$, E scheme; $R = 0.8$, E scheme; $R = 0.4$, WTA mod p scheme; $R = 0.8$, WTA mod p scheme. Bottom row: k_t , left to right: $N = 2$, E scheme; $N = 3$, E scheme; $N = 2$, WTA mod p scheme; $N = 3$; WTA mod p scheme.

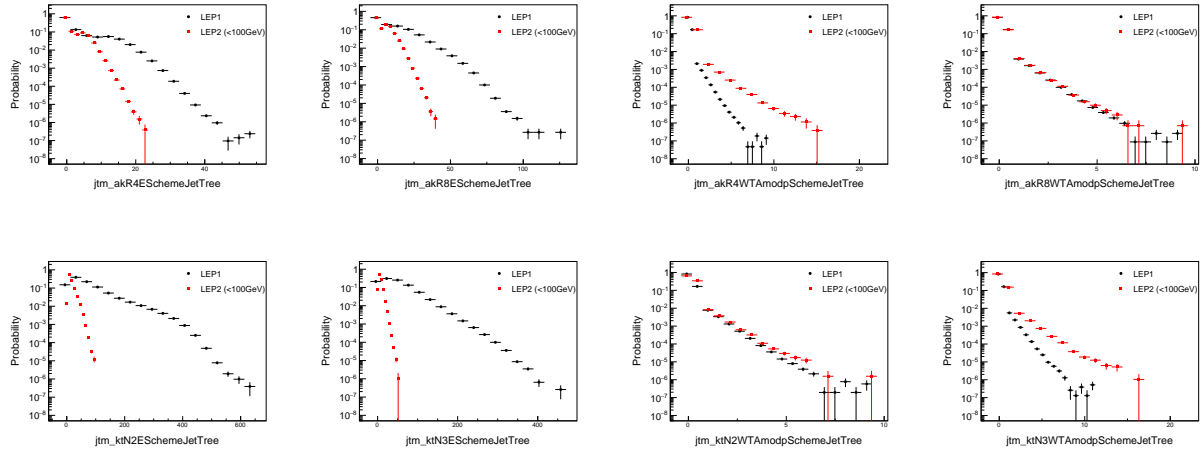


FIG. 38: LEP1 vs LEP2 (event energy $> 100\text{GeV}$) Jet mass distributions. Top row: anti- k_t , left to right: $R = 0.4$, E scheme; $R = 0.8$, E scheme; $R = 0.4$, WTA mod p scheme; $R = 0.8$, WTA mod p scheme. Bottom row: k_t , left to right: $N = 2$, E scheme; $N = 3$, E scheme; $N = 2$, WTA mod p scheme; $N = 3$; WTA mod p scheme.

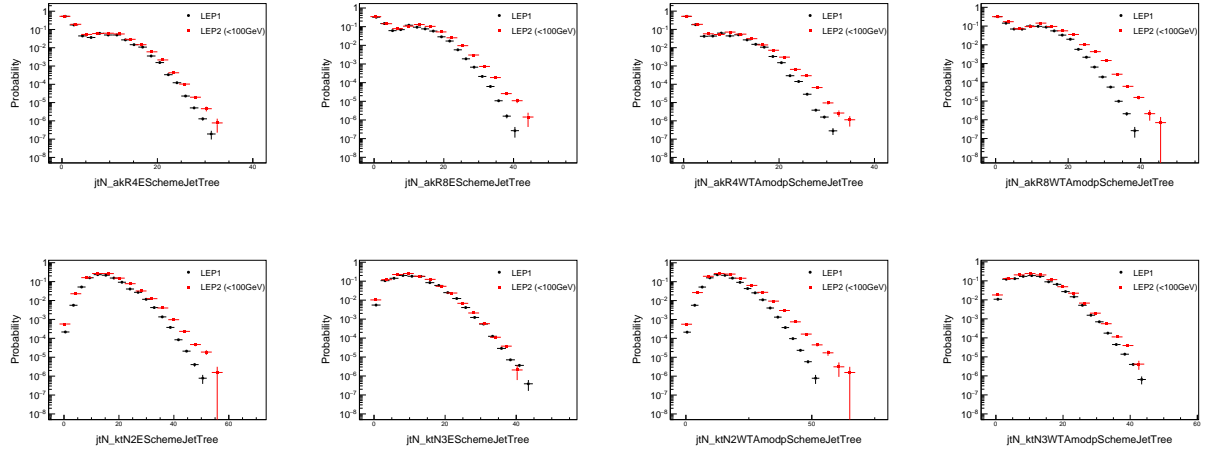


FIG. 39: LEP1 vs LEP2 (event energy $> 100\text{GeV}$) Jet N distributions. Top row: anti- k_t , left to right: $R = 0.4$, E scheme; $R = 0.8$, E scheme; $R = 0.4$, WTA mod p scheme; $R = 0.8$, WTA mod p scheme. Bottom row: k_t , left to right: $N = 2$, E scheme; $N = 3$, E scheme; $N = 2$, WTA mod p scheme; $N = 3$; WTA mod p scheme.

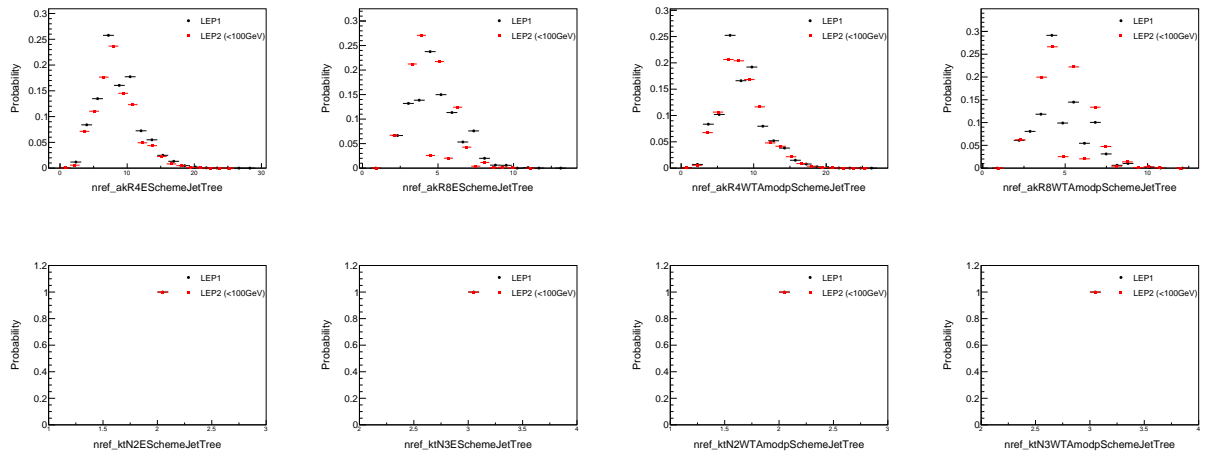


FIG. 40: LEP1 vs LEP2 (event energy $> 100\text{GeV}$) Jet n_{ref} distributions. Top row: anti- k_t , left to right: $R = 0.4$, E scheme; $R = 0.8$, E scheme; $R = 0.4$, WTA mod p scheme; $R = 0.8$, WTA mod p scheme. Bottom row: k_t , left to right: $N = 2$, E scheme; $N = 3$, E scheme; $N = 2$, WTA mod p scheme; $N = 3$; WTA mod p scheme.

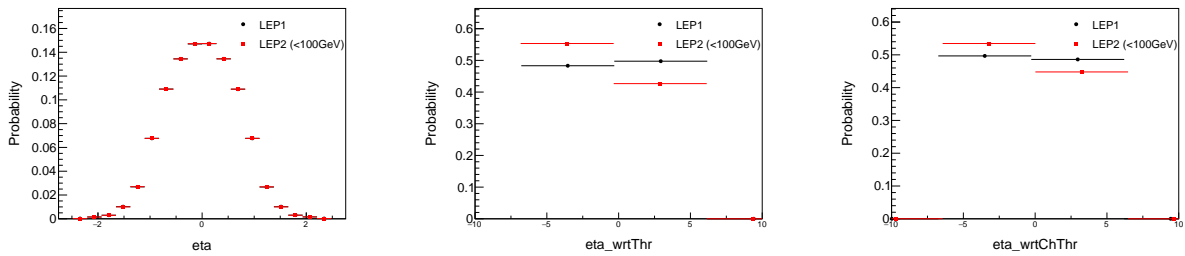


FIG. 41: LEP1 vs LEP2 (event energy > 100GeV) η distributions. Left to right: η ; η with respect to thrust axis; η with respect to charged thrust axis.

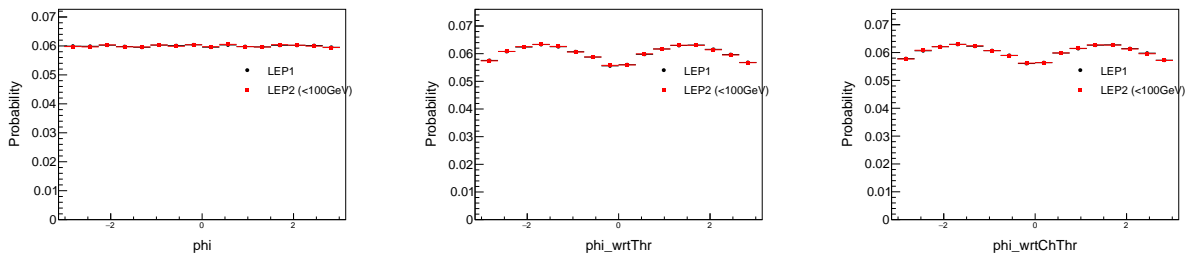


FIG. 42: LEP1 vs LEP2 (event energy > 100GeV) ϕ distributions. Left to right: ϕ ; ϕ with respect to thrust axis; ϕ with respect to charged thrust axis.

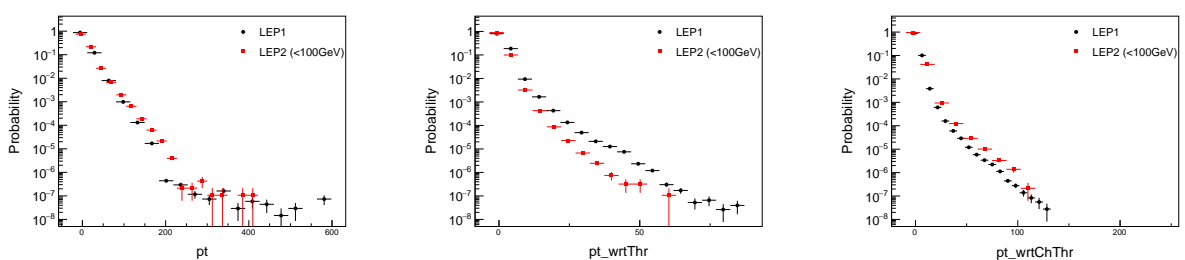


FIG. 43: LEP1 vs LEP2 (event energy > 100GeV) p_t distributions. Left to right: p_t ; p_t with respect to thrust axis; p_t with respect to charged thrust axis.

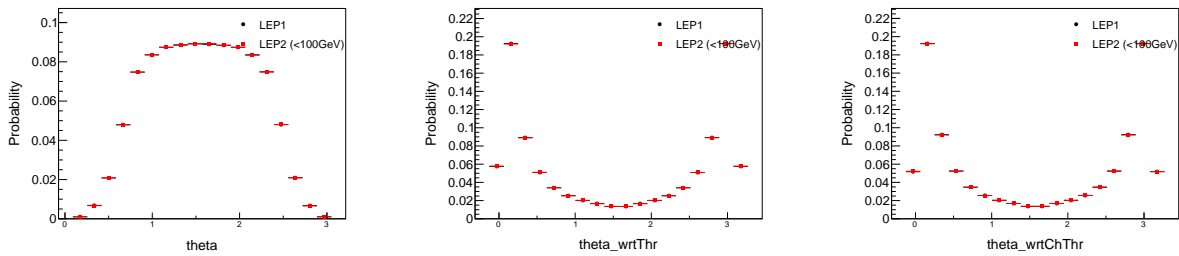


FIG. 44: LEP1 vs LEP2 (event energy > 100GeV) θ distributions. Left to right: θ ; θ with respect to thrust axis; θ with respect to charged thrust axis.

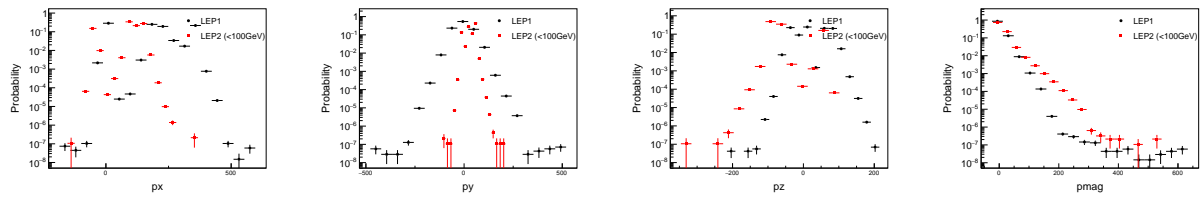


FIG. 45: LEP1 vs LEP2 (event energy > 100GeV) p_x , p_y , p_z , and $|\vec{p}|$ distributions.

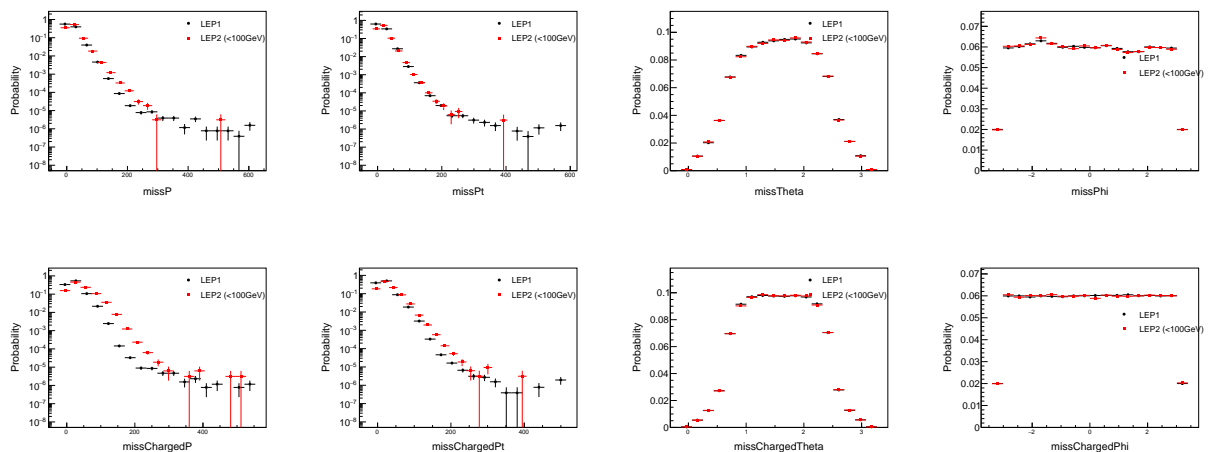


FIG. 46: LEP1 vs LEP2 (event energy > 100GeV) missing quantities distribution. Left to right: missing P ; missing p_t ; missing θ ; missing ϕ . Top to bottom: All; charged.

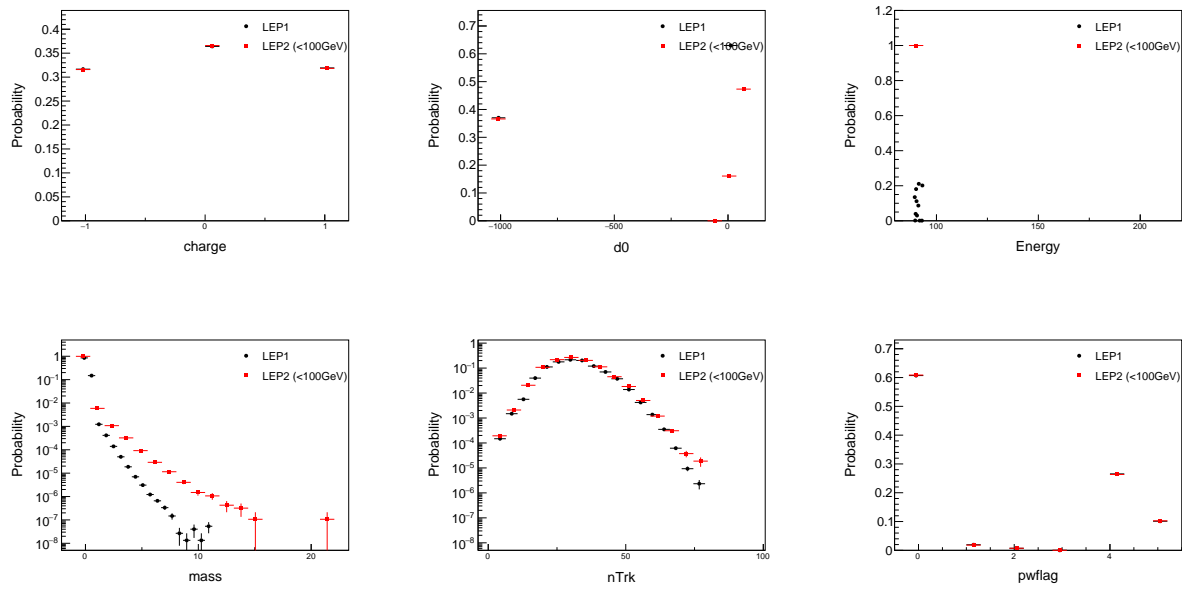


FIG. 47: Left to right: Top row: LEP1 vs LEP2 (event energy $> 100\text{GeV}$) charge, d_0 , and energy distributions. Bottom row: LEP1 vs LEP2 (event energy $> 100\text{GeV}$) mass, particle multiplicity, and pwflag distributions.

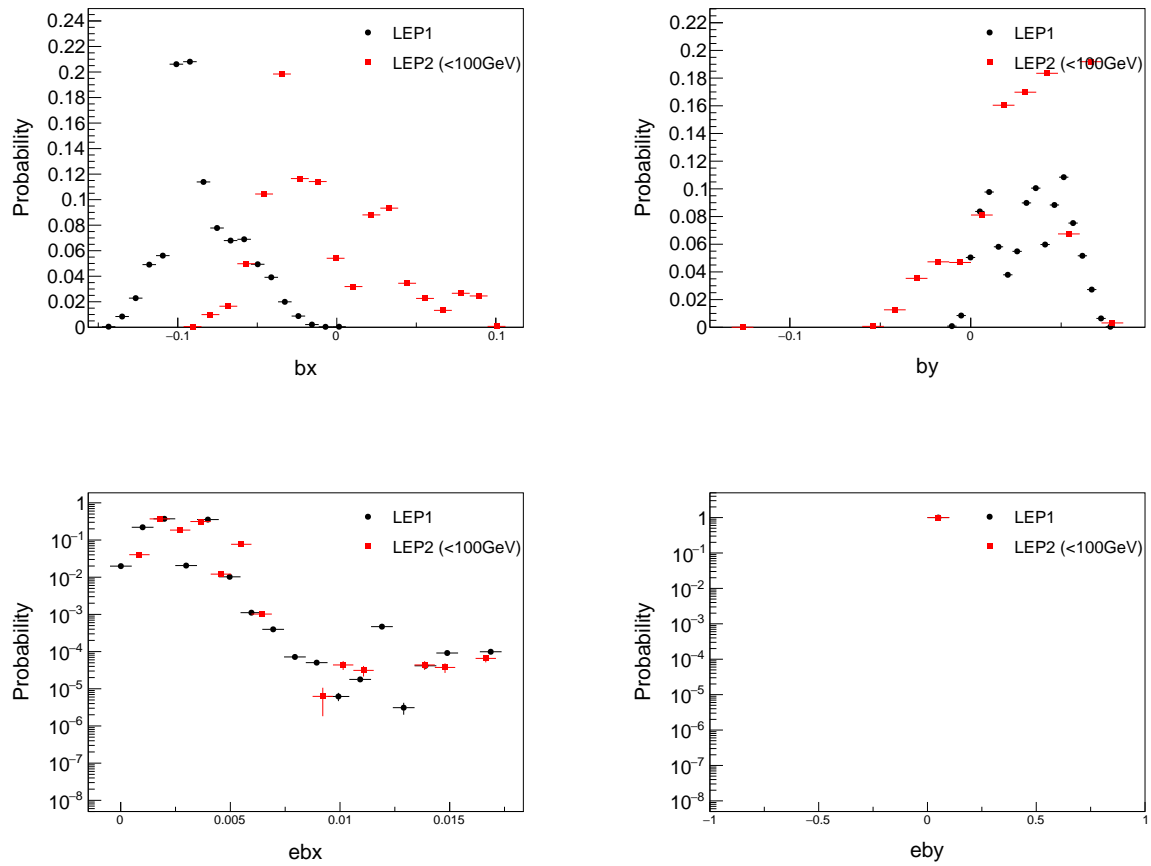


FIG. 48: Top row: LEP1 vs LEP2 (event energy $> 100\text{GeV}$) beamspot x and y . Bottom row: Error in beamspot x and y .

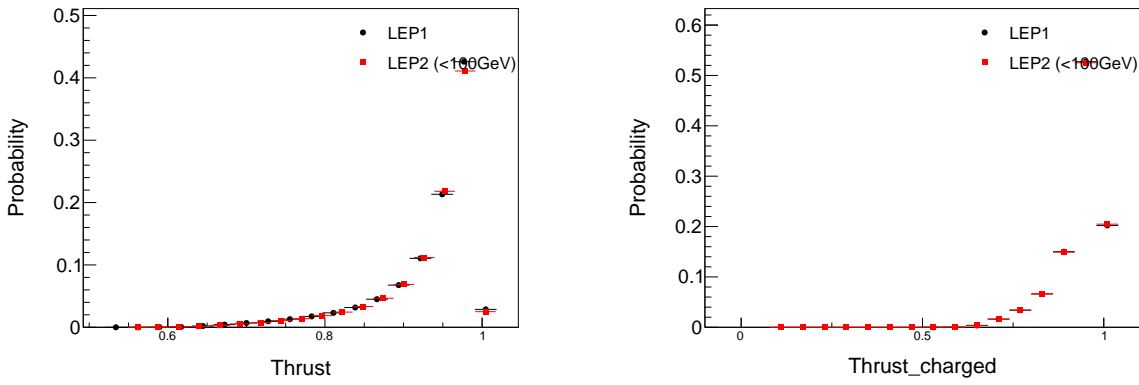


FIG. 49: Left: LEP1 vs LEP2 (event energy > 100GeV) thrust distribution. Right: LEP1 vs LEP2 (event energy > 100GeV) charged thrust distribution.

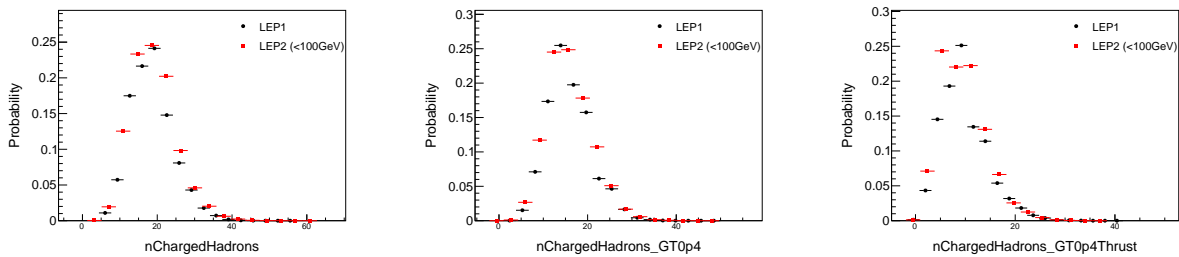


FIG. 50: LEP1 vs LEP2 (event energy > 100GeV) charged hadron multiplicity distributions. Left to right: charged hadron multiplicity; charged hadron multiplicity (GT0p4); charged hadron multiplicity (GT0p4Thrust).

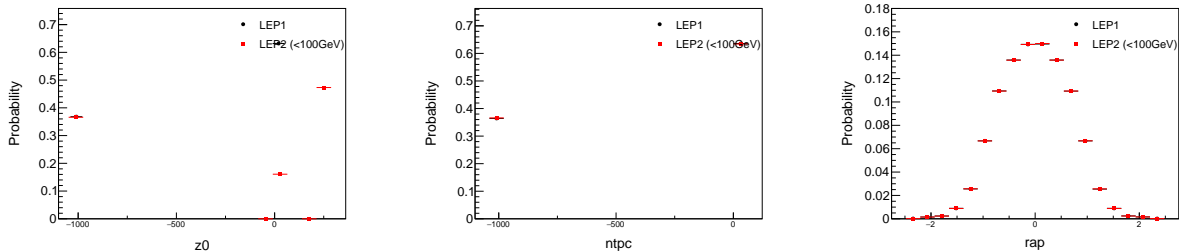


FIG. 51: Left: LEP1 vs LEP2 (event energy $> 100\text{GeV}$) z_0 distribution. Center: LEP1 vs LEP2 (event energy $> 100\text{GeV}$) TPC hits distribution. Right: LEP1 vs LEP2 (event energy $> 100\text{GeV}$) rapidity distribution.

V. MULTIPLICITY DISTRIBUTIONS

Previous measurements of two particle correlations have been done at hadron collider experiments, such as CMS. These measurements typically are typically done in bins of event multiplicity in order to quantify the activity in a set of events. Because ALEPH has a different acceptance than the CMS detector, and because e^+e^- collisions have different kinematics than those at hadron colliders, some conversion needs to be done in order to compare events of a given multiplicity in ALEPH with those in CMS. For the studies done here, we require charged tracks to have $p_T < 0.2 \text{ GeV}$ and $|\eta| < 1.8$ in ALEPH, and $p_T < 0.4$ and $|\eta| < 2.4$ in CMS. The latter requirement is identical to the cuts used in all CMS papers on two particle correlations. The multiplicity distribution in LEP1 ALEPH events can be seen in Fig. 52. The tracking efficiency as a function of event multiplicity can be seen in Fig. 53, calculated by matching reconstructed tracks to generator-level particles in ALEPH Monte Carlo. The dip at low multiplicity is most likely due to a self-bias causing low-efficiency events to also have low multiplicity. After taking into account both the efficiency and acceptance of the ALEPH detector, the total fraction of charged particles reconstructed is shown in Fig. 54. In the highest multiplicity events, the ALEPH detector reconstructions around 50% of all the charged particles in an event.

The acceptance of the CMS detector, as calculated by seeing how many generator-level charged particles pass the η cut, in pp pythia Monte Carlo events is shown in Fig. 55. This is done as a function of generator-level multiplicity. Roughly 30% of all charged particles can be reconstructed in CMS for pp collisions. Using Fig. 54 and Fig. 55, a conversion

factor can be calculated to convert the reconstructed ALEPH multiplicity to an equivalent corrected multiplicity for a hadron collider. This conversion factor is shown in Fig. 56, and the mapping from ALEPH multiplicities to CMS multiplicities is shown in Fig. 57. The behavior at low multiplicities is caused by the self-bias of the efficiency and acceptances with the multiplicity calculation. However, this analysis is mostly interested in events having high multiplicity, where the conversion factor converges to a reasonable factor of around 0.7. After applying this mapping to the distribution in Fig. 52, the multiplicity distribution that can be used for comparing with CMS results is shown in Fig. 58.

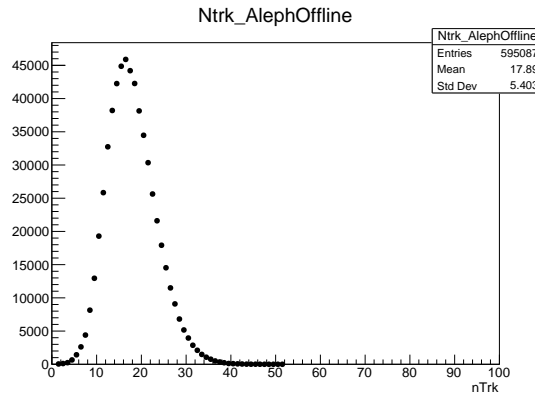


FIG. 52: LEP1 Multiplicity Distribution

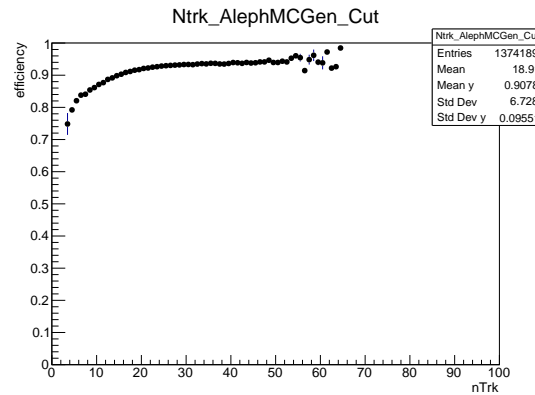


FIG. 53: LEP1 Efficiency Distribution vs Multiplicity

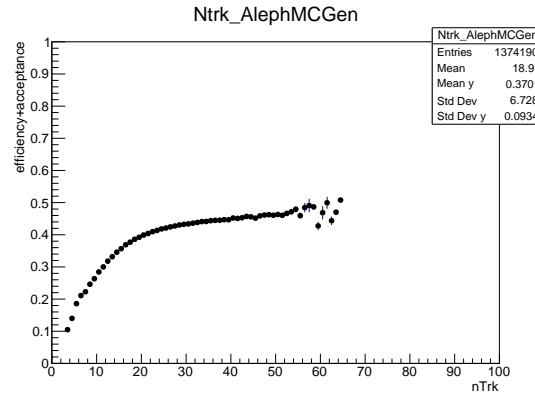


FIG. 54: LEP1 Efficiency+Acceptance Distribution vs Multiplicity

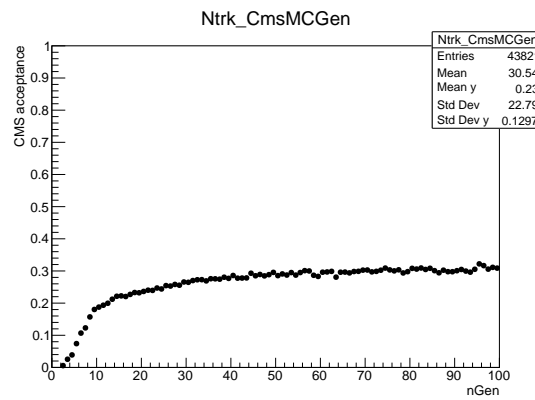


FIG. 55: CMS Acceptance Distribution vs generator-level Multiplicity

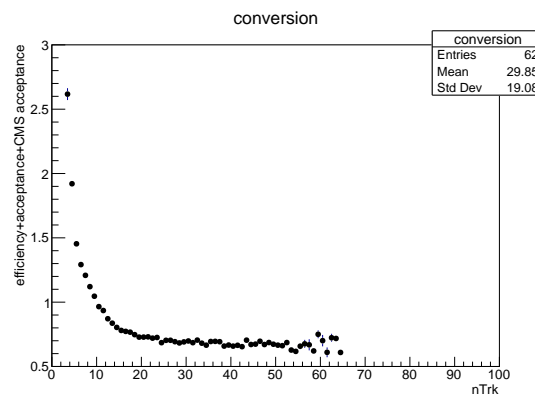


FIG. 56: Conversion factor from ALEPH to CMS multiplicity

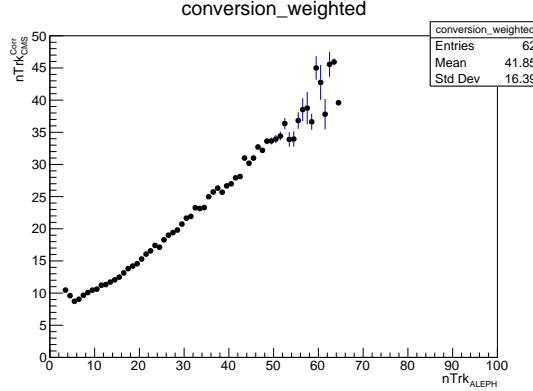


FIG. 57: Conversion mapping from ALEPH to CMS multiplicity

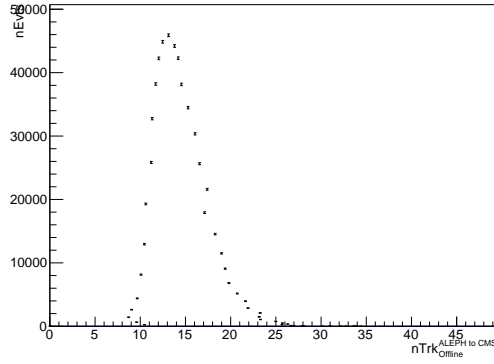


FIG. 58: Scaled ALEPH multiplicity for comparing to CMS

VI. ANALYSIS

VII. THRUST AND SPHERICITY AXES

The thrust T , and the thrust axis, \hat{n} , are defined as using the vector which maximizes the sum of the projection of the momenta of all particles in the event onto the axis:

$$T = \max_{\hat{n}} \frac{\sum_i |\hat{p}_i \cdot \hat{n}|}{\sum_i |\hat{p}_i|}. \quad (1)$$

Events which are 'pencil-like' in shape are expected to have T close to unity, while events in which the particles are distributed rather isotropically are expected to have T close to 0.5.

The thrust is calculated for an event having n particles, each having a momentum \vec{p}_i ,

using an iterative procedure. The initial thrust axis, \vec{T}_0 is first taken to be a unit vector along the axis of any particle. The thrust axis is then updated according to

$$\vec{T}_{i+1} = \vec{T}_i + \sum_{j=1}^n \text{sign}(\vec{p}_j \cdot \vec{T}_i) \vec{p}_j. \quad (2)$$

This procedure is repeated until there have either been n iterations, or when the sign of $\vec{p}_j \cdot \vec{T}_i$ does not change for every particle between the i and $i + 1$ iterations. The resulting vector, \vec{T}_{cand} , is then stored as a thrust axis candidate. The entire procedure is then repeated n times, each time starting with a new initial particle, to give n thrust axis candidates. The candidate which maximizes the quantity T is then chosen as the final thrust axis.

Another event shape variable used in this analysis is the sphericity axis. The sphericity tensor is defined as

$$S^{\alpha\beta} = \frac{\sum_i p_i^\alpha p_i^\beta}{\sum_i |p_i|^2}, \quad (3)$$

where α and β can take on values of one to three, corresponding to the x , y , and z axes. This can be diagonalized and three eigenvalues, $\lambda_1 \geq \lambda_2 \geq \lambda_3$ can be found, whose sum is unity. The sphericity is defined as

$$S = \frac{3}{2}(\lambda_2 + \lambda_3). \quad (4)$$

It is bound between zero and one, with zero corresponding to a 'pencil-like' event and one corresponding to an isotropic event. A related variable, the Aplanarity is defined as

$$A = \frac{3}{2}(\lambda_3). \quad (5)$$

A planar event has $A = 0$, while an isotropic one has $A = 0.5$.

The sphericity axis, \vec{S} is simply defined as the eigenvector corresponding to λ_1 .

VIII. WINNER-TAKE-ALL AXIS

IX. EVENT SELECTION

X. THRUST DISTRIBUTION

In order to validate the ALEPH archived data sample and our understanding, an analysis of the thrust distribution (T) is performed with LEP1 archived data. The distributions are corrected for the detector response by ALEPH MC produced in 1994. The correction factors, which are obtained from ratio of generator level and detector level Thrust spectra, are shown in Figure 59. The size of the correction factor is small in the mid- T and becomes larger as we go to smaller T or larger T regions.

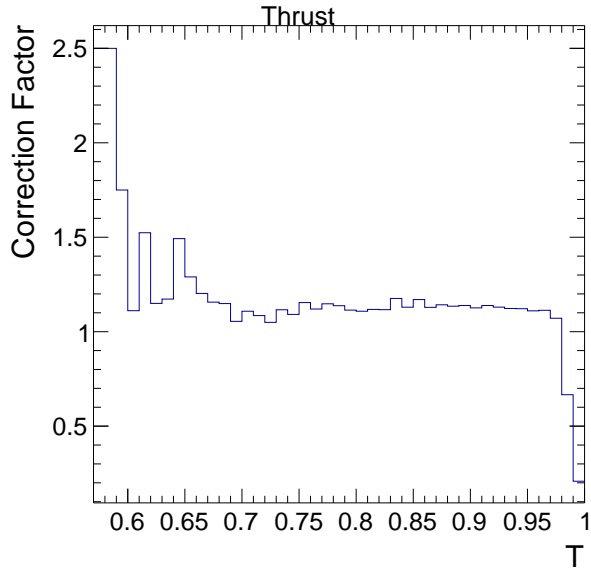


FIG. 59: The correction factor for the Thrust distribution measurement obtained from ALEPH MC.

Figure 60 shows the corrected thrust distribution from ALEPH archived data. The results are compared to ALEPH publications [? ?]. As shown in the figure, a very good agreement between ALEPH archived data from this note and ALEPH publications in the low T region. In the $T \sim 1$ region, some disagreement at the level of 10% is observed between this work and the ALEPH publication in 2004 [?]. This is probably due to the hadronization correction which is not applied in ref. [?] and this work.

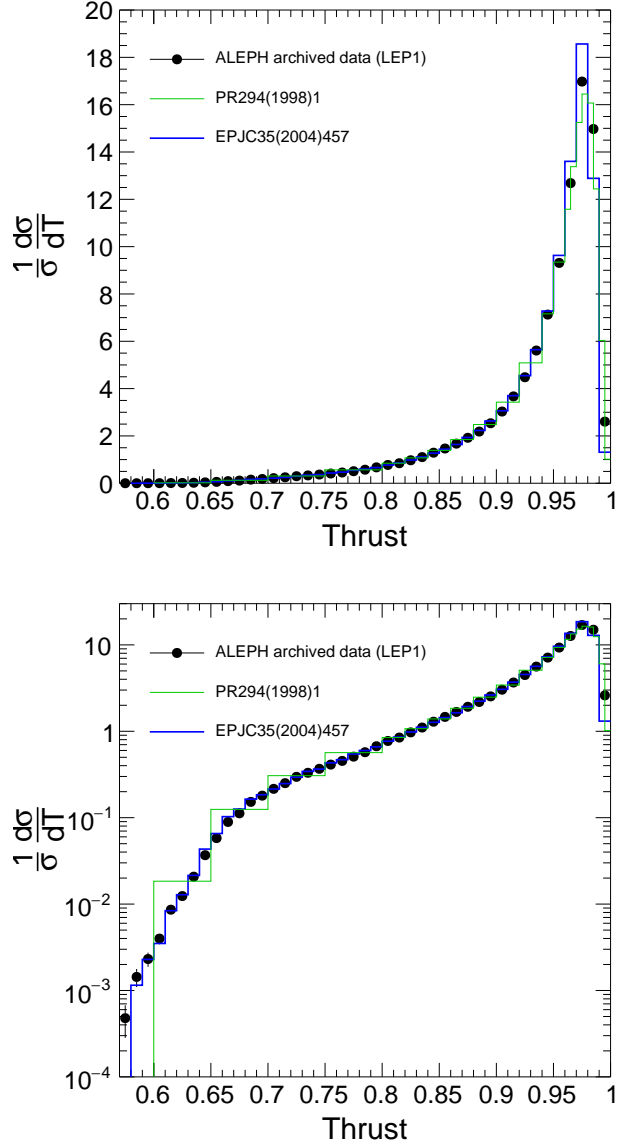


FIG. 60: The corrected thrust distribution from ALEPH archived data compared to previous publications in linear and log scale.

XI. TWO-PARTICLE CORRELATION FUNCTION

In this analysis with ALEPH open data, charged particles with transverse momentum between 0.1 and 4.0 GeV/ c are selected for the correlation function analysis. High multiplicity events are sampled using the total number of selected proton, pions and kaons (hadron multiplicity N) in each event. The first step in extracting the correlation function was to divide the sample into bins in the hadron multiplicity. For each hadron multiplicity class, “trig-

ger” particles are defined as charged hadrons in the selected transverse momentum range (0.1 and 4.0 GeV/ c). Particle pairs are then formed by associating every trigger particle with the remaining charged hadrons in the same p_T interval as the trigger particle. The per-trigger-particle associated yield is defined as:

$$\frac{1}{N_{\text{trig}}} \frac{d^2N^{\text{pair}}}{d\Delta\eta d\Delta\phi} = B(0, 0) \times \frac{S(\Delta\eta, \Delta\phi)}{B(\Delta\eta, \Delta\phi)} \quad (6)$$

where N_{trig} is the number of trigger particles in the event, $\Delta\eta$ and $\Delta\phi$ are the differences in η and ϕ of the pair. The signal distribution, $S(\Delta\eta, \Delta\phi)$, is the per-trigger-particle yield of particle pairs in the same event:

$$S(\Delta\eta, \Delta\phi) = \frac{1}{N_{\text{trig}}} \frac{d^2N^{\text{same}}}{d\Delta\eta d\Delta\phi} \quad (7)$$

The mixed-event background distribution, used to account for random combinatorial background, is defined as

$$B(\Delta\eta, \Delta\phi) = \frac{1}{N_{\text{trig}}} \frac{d^2N^{\text{mix}}}{d\Delta\eta d\Delta\phi} \quad (8)$$

and is constructed by pairing the trigger particles from two random events in the same hadron multiplicity interval. The symbol N^{mix} denotes the number of pairs taken from the mixed event, while $B(0, 0)$ represents the mixed-event associated yield for both particles of the pair going in the same direction and thus having full pair acceptance. Therefore, the ratio $B(0, 0)/B(\Delta\eta, \Delta\phi)$ represents the pair-acceptance correction factor used to derive the corrected per-trigger-particle associated yield distribution. The signal and background distributions are first calculated for each event and then averaged over all the events within the track multiplicity class.

In the full data analysis, a matching between particles and the primary vertex should be performed so that the studies are done with primary hadrons from a single primary vertex. This matching requirement is not yet included in this preliminary analysis due to the limited information in the Belle open data.

Two particle correlation functions for the LEP1 and LEP2 data sets analyzed in the beam, thrust, and winner-take-all (WTA) axes are shown below. The first row contains events with $n_{\text{Trk}} < 20$, the second with $20 \leq n_{\text{Trk}} < 30$, and third with $30 \leq n_{\text{Trk}}$.

Date	Axis	p_T	$ \eta $	θ	p	$ dxy $	$ dz $	nTPC
2018.01.26	Beam	≥ 0.4	<1.8	off	off	off	off	off
	Thrust	≥ 0.4	<5.0	off	off	off	off	off
	WTA	≥ 0.4	<5.0	off	off	off	off	off
2018.02.XX	Beam	≥ 0.4	<1.8	[20,160]	>0.2	<3.0	<5.0	≥ 4.0
	Thrust	≥ 0.4	<5.0	[20,160]	>0.2	<3.0	<5.0	≥ 4.0
	WTA	≥ 0.4	<5.0	[20,160]	>0.2	<3.0	<5.0	≥ 4.0

TABLE I: Track cuts for Beam, Thrust, and WTA axes.

Date	Axis	WW	p_{miss}	2-Jet	p_{miss}^{rel}	3rd-Jet	$p_{1,2}^{rel}$	N_{trk}
2018.01.26	Beam	off	off	off	off	off	off	>1
	Thrust	off	off	off	off	off	off	>1
	WTA	off	off	off	off	off	off	>1
2018.02.XX	Beam	off	≤ 20	0.1	0.03	0.03	0.03	>1
	Thrust	off	≤ 20	0.1	0.03	0.03	0.03	>1
	WTA	off	≤ 20	0.1	0.03	0.03	0.03	>1

TABLE II: Event cuts for Beam, Thrust, and WTA axes.

A. Analysis for 2018.01.26 production

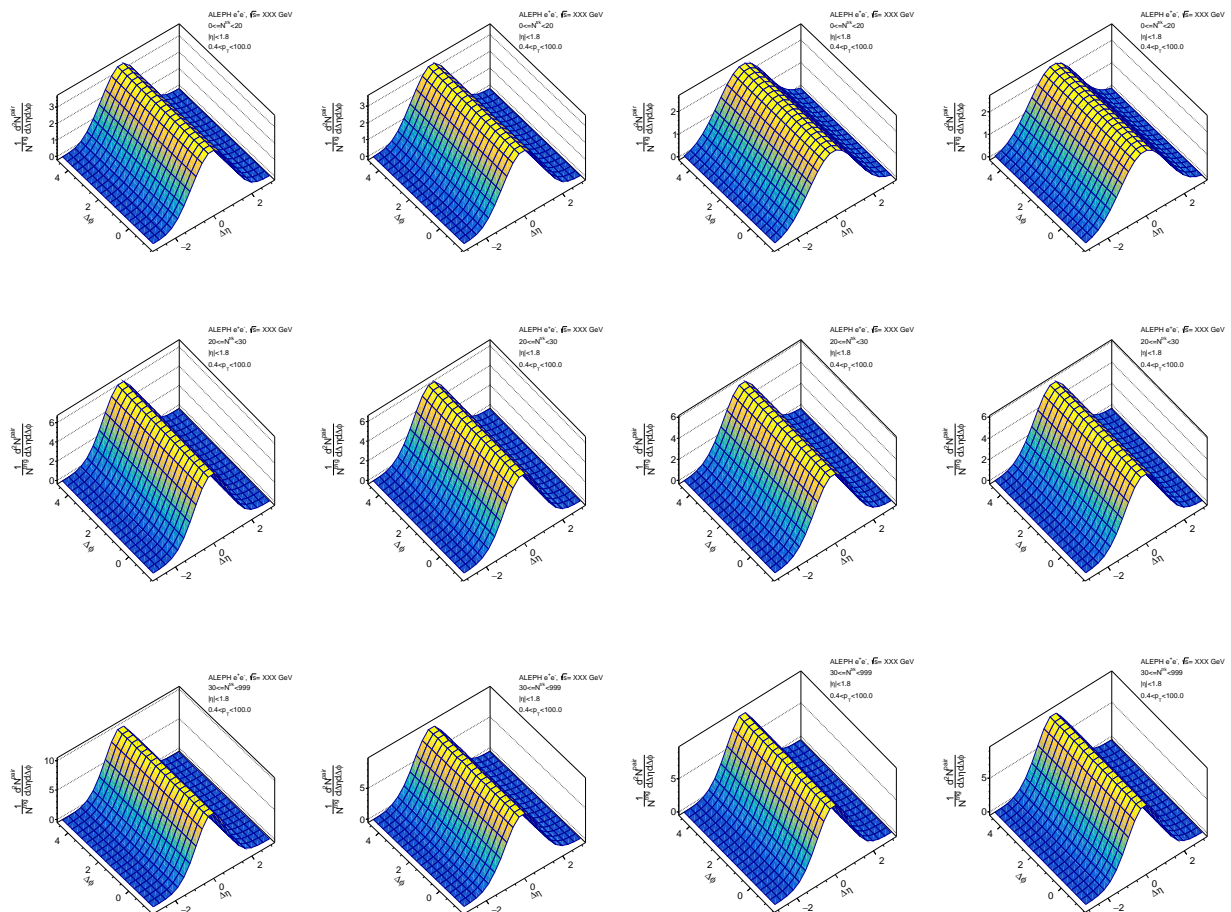


FIG. 61: Background function for beam axis. Left to right: LEP1, LEP2, PYTHIA8, PYTHIA8 rope walk. Top to bottom: multiplicity 0-20, 20-30, 30-999.

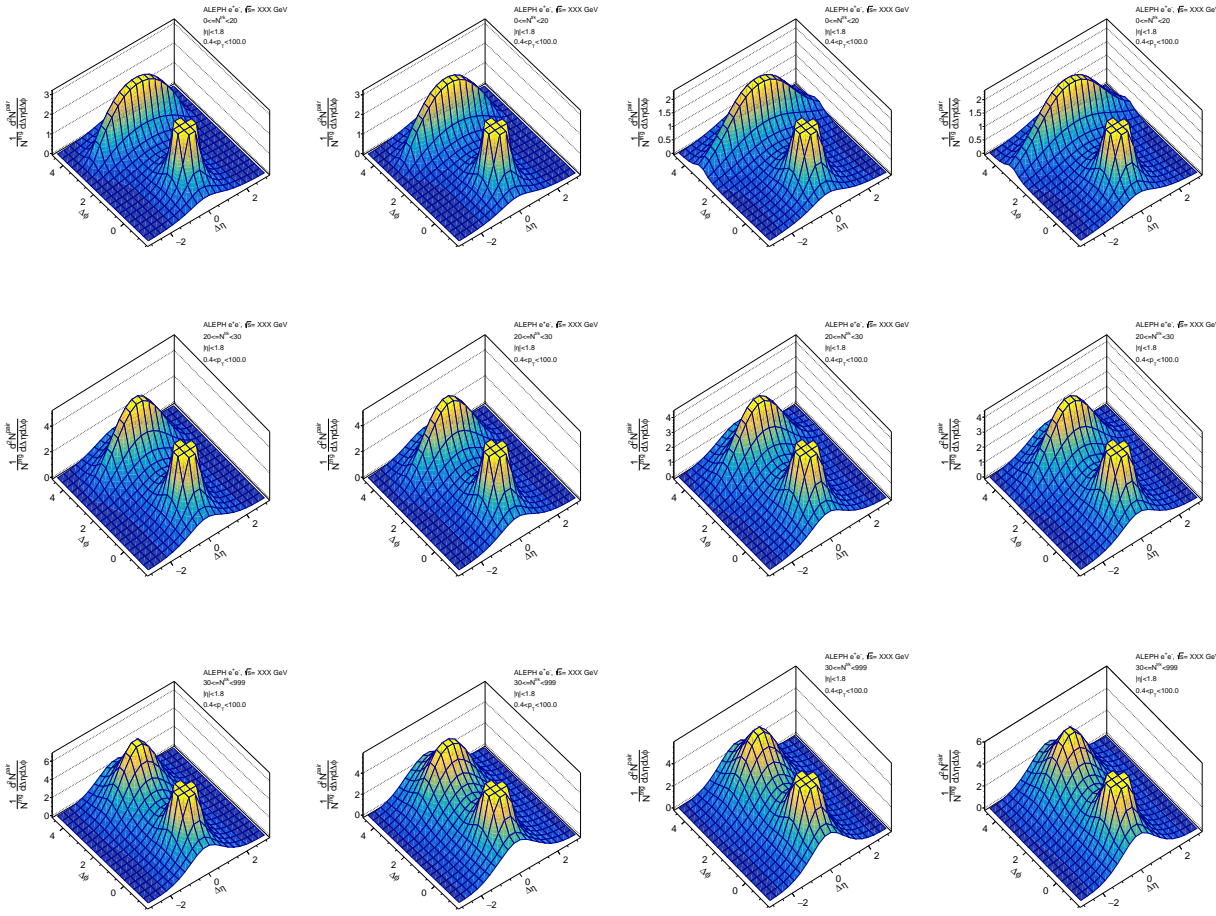


FIG. 62: Signal function for beam axis. Left to right: LEP1, LEP2, PYTHIA8, PYTHIA8 rope walk. Top to bottom: multiplicity 0-20, 20-30, 30-999.

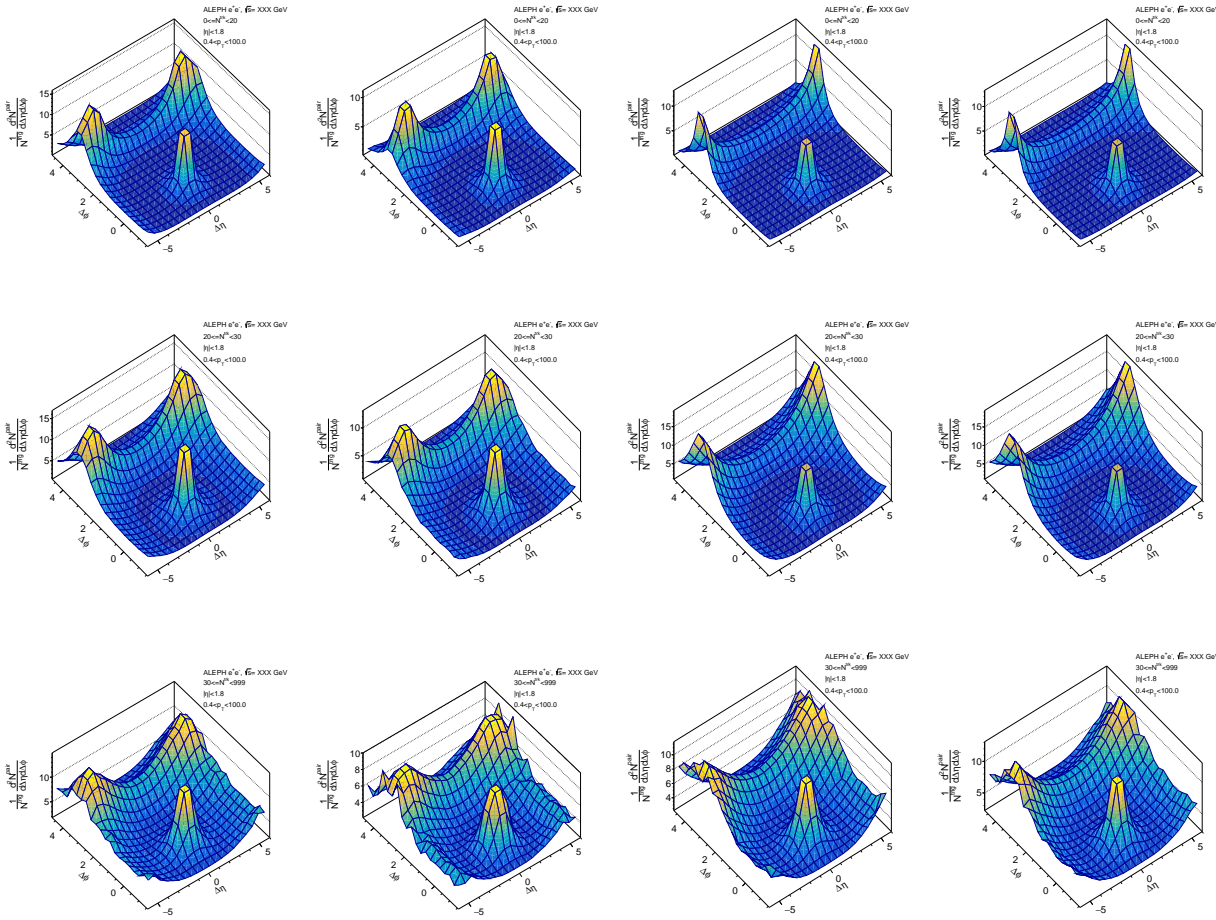


FIG. 63: Ratio function for beam axis. Left to right: LEP1, LEP2, PYTHIA8, PYTHIA8 rope walk. Top to bottom: multiplicity 0-20, 20-30, 30-999.

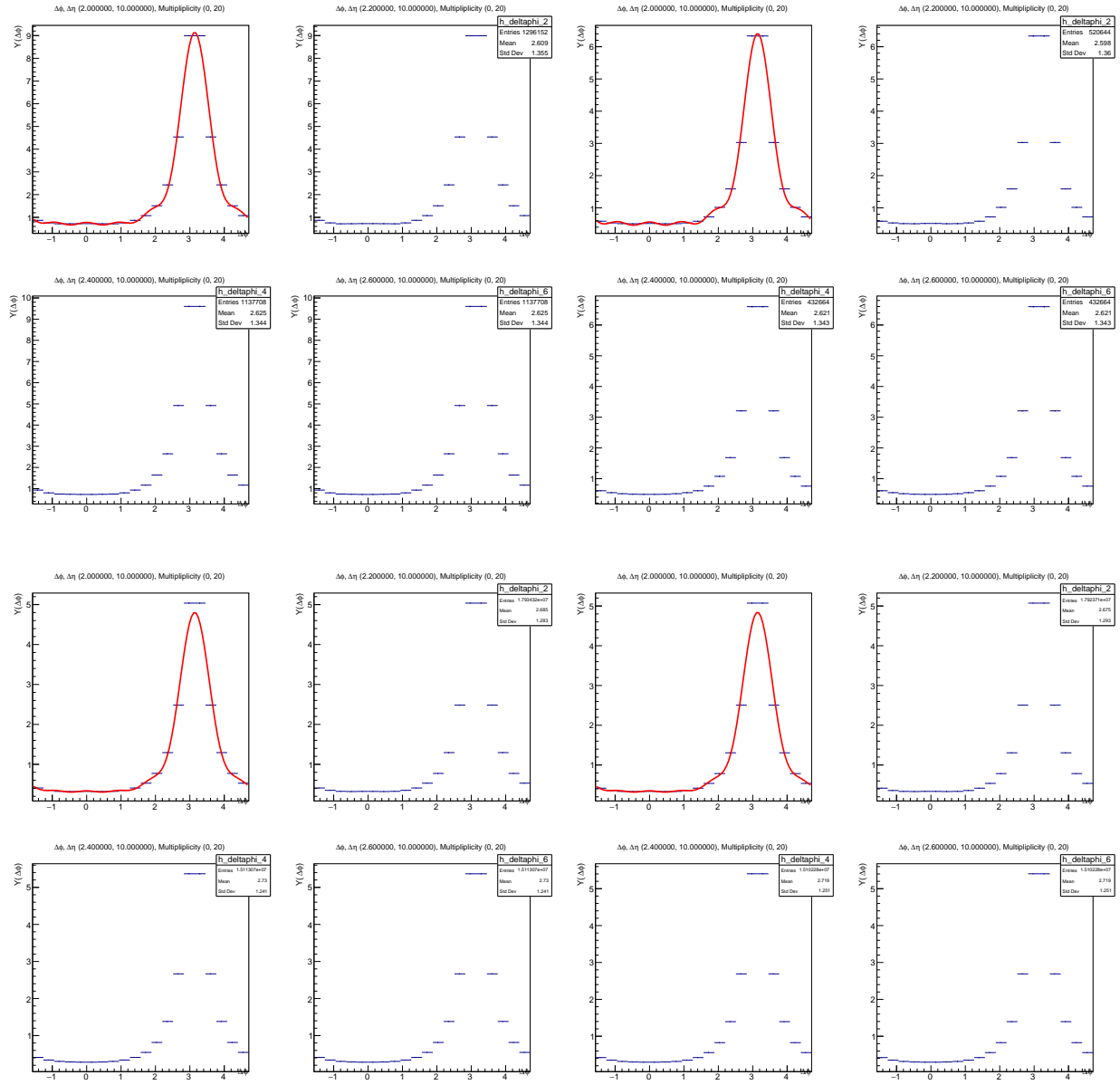


FIG. 64: Long range yield function for beam axis. Top row is LEP1 and LEP2, bottom row PYTHIA8 and PYTHIA8 rope walk. Multiplicity 0-20.

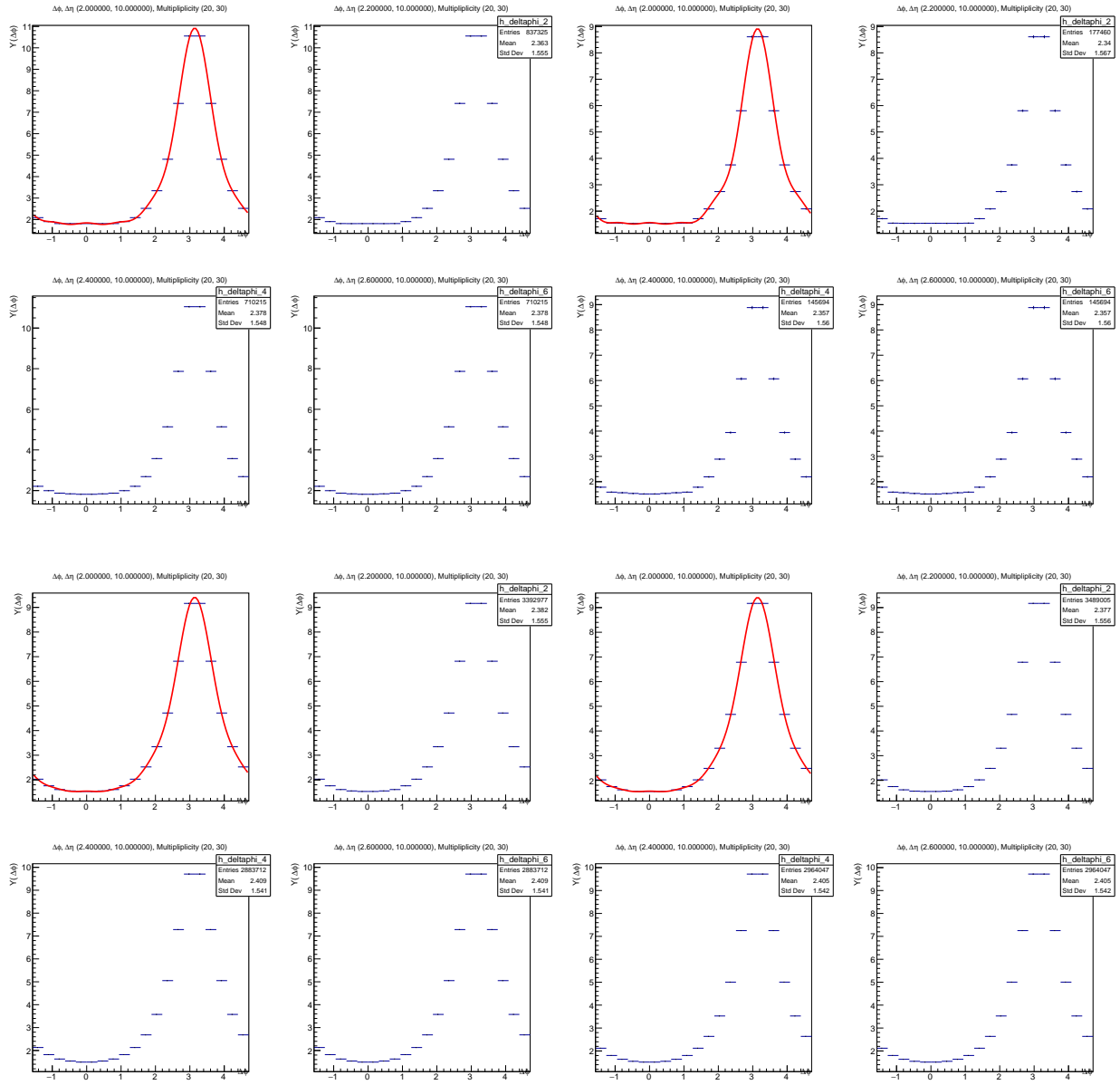


FIG. 65: Long range yield function for beam axis. Top row is LEP1 and LEP2, bottom row PYTHIA8 and PYTHIA8 rope walk. Multiplicity 20-30.

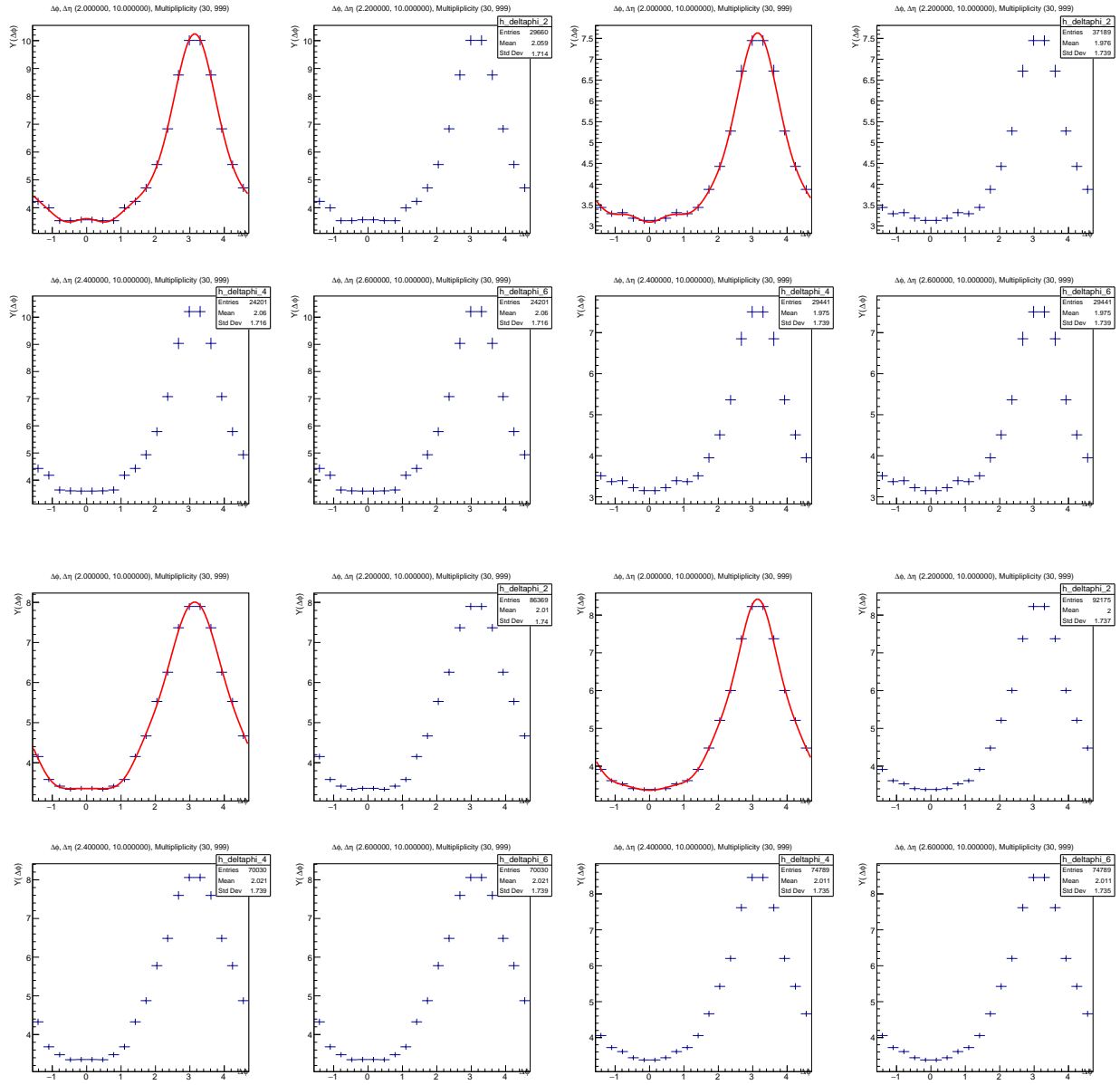


FIG. 66: Long range yield function for beam axis. Top row is LEP1 and LEP2, bottom row PYTHIA8 and PYTHIA8 rope walk. Multiplicity 30-999.

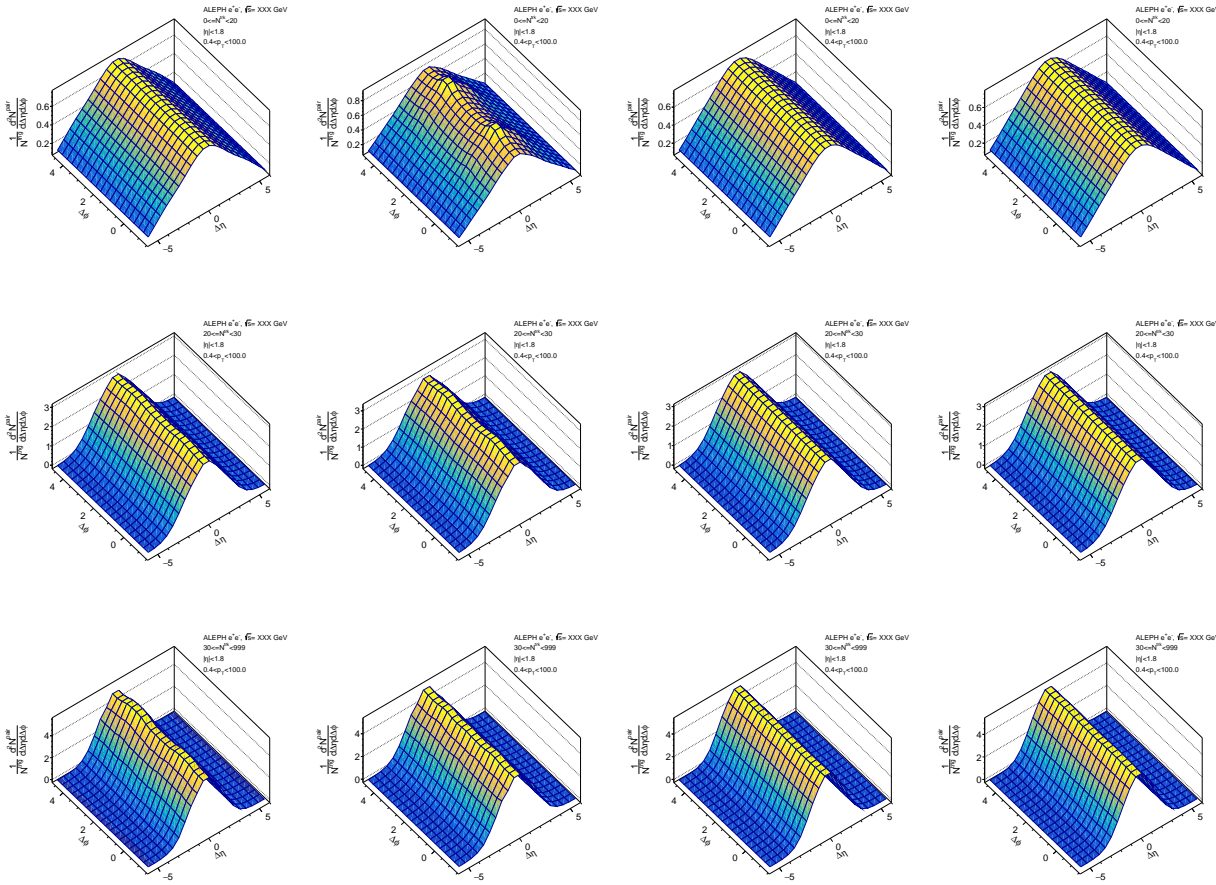


FIG. 67: Background function for thrust axis. Left to right: LEP1, LEP2, PYTHIA8, PYTHIA8 rope walk. Top to bottom: multiplicity 0-20, 20-30, 30-999.

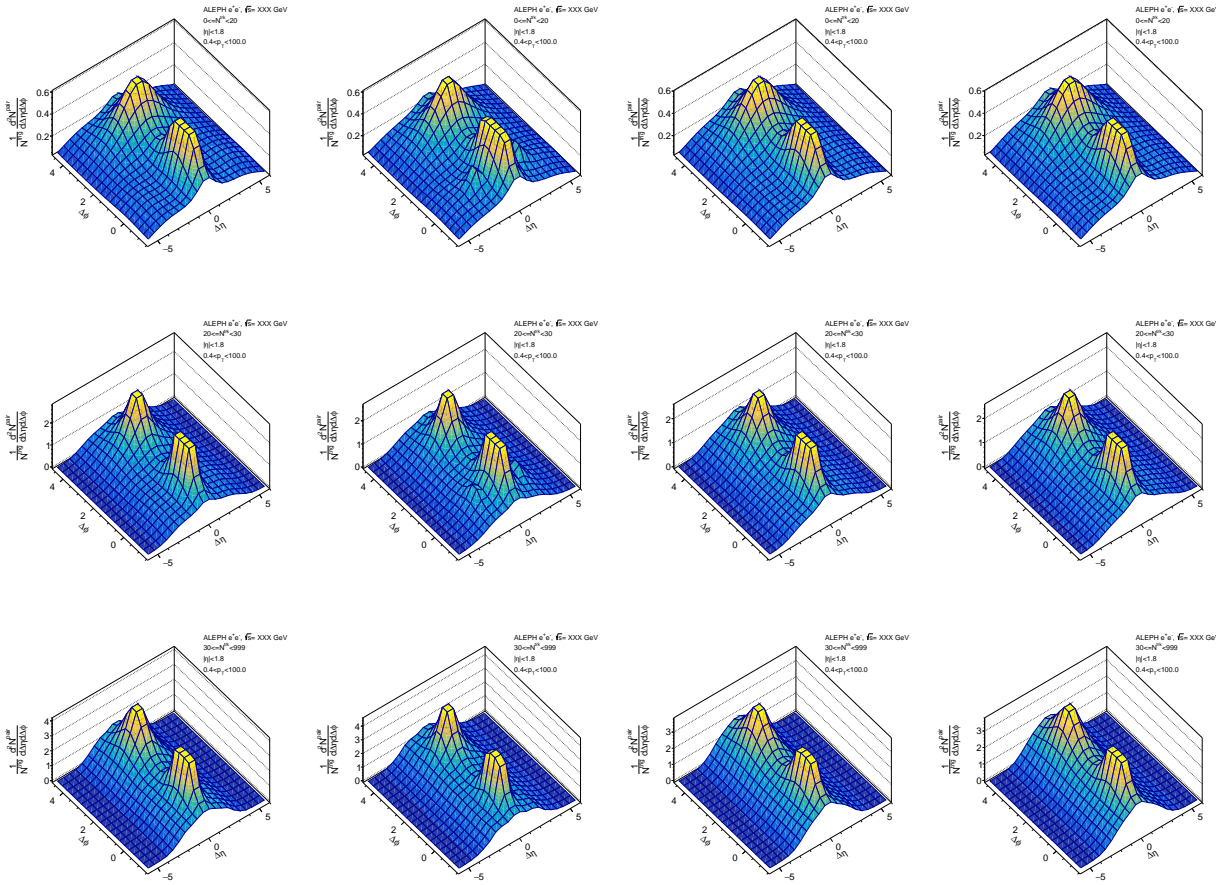


FIG. 68: Signal function for thrust axis. Left to right: LEP1, LEP2, PYTHIA8, PYTHIA8 rope walk. Top to bottom: multiplicity 0-20, 20-30, 30-999.

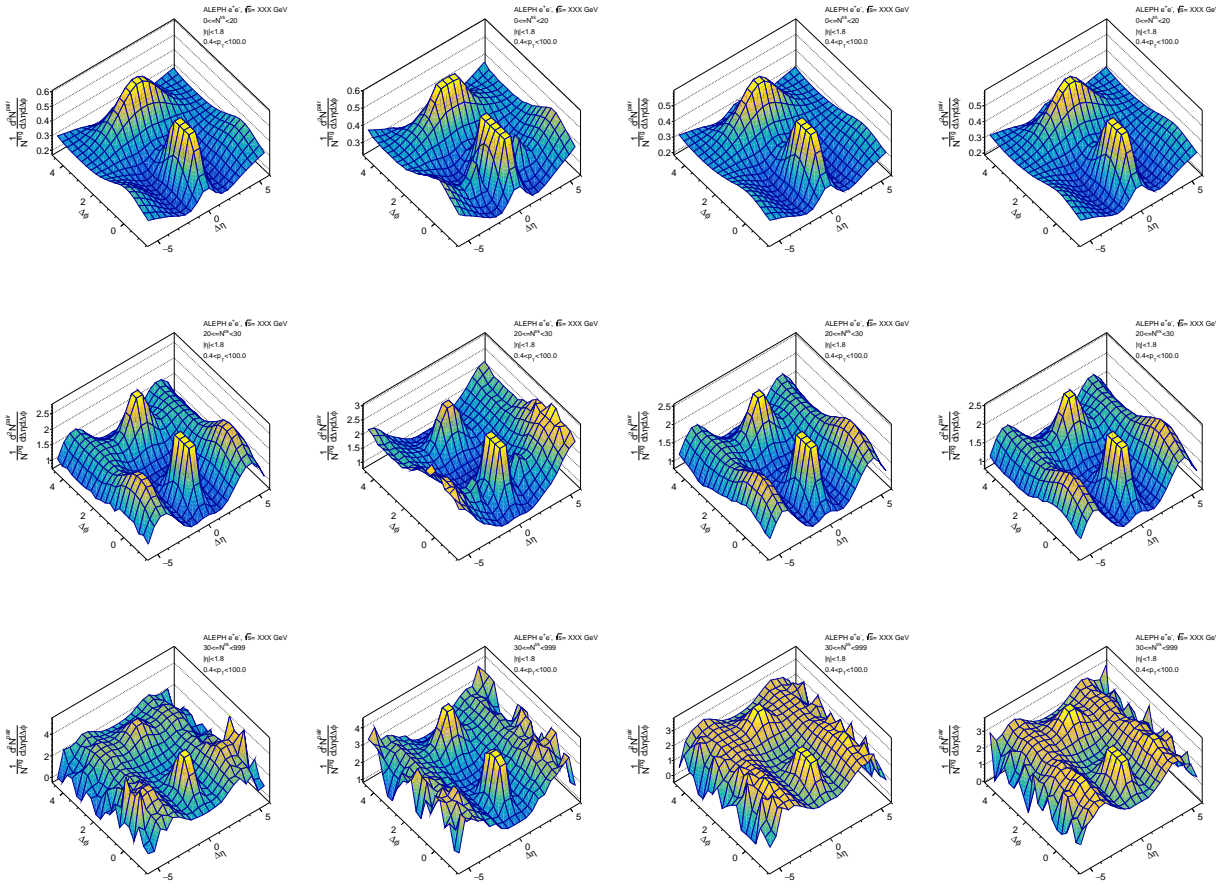


FIG. 69: Ratio function for thrust axis. Left to right: LEP1, LEP2, PYTHIA8, PYTHIA8 rope walk. Top to bottom: multiplicity 0-20, 20-30, 30-999.

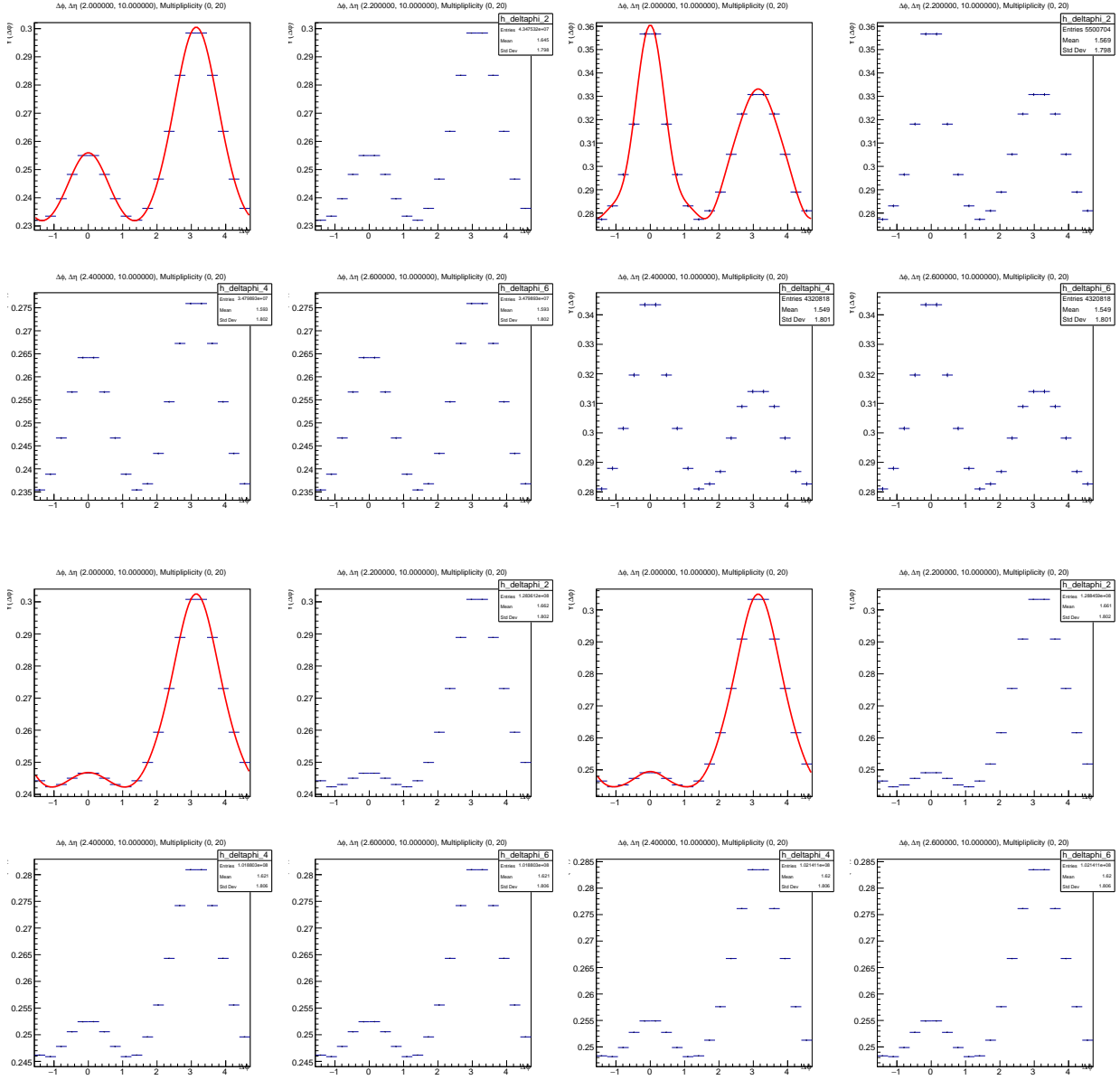
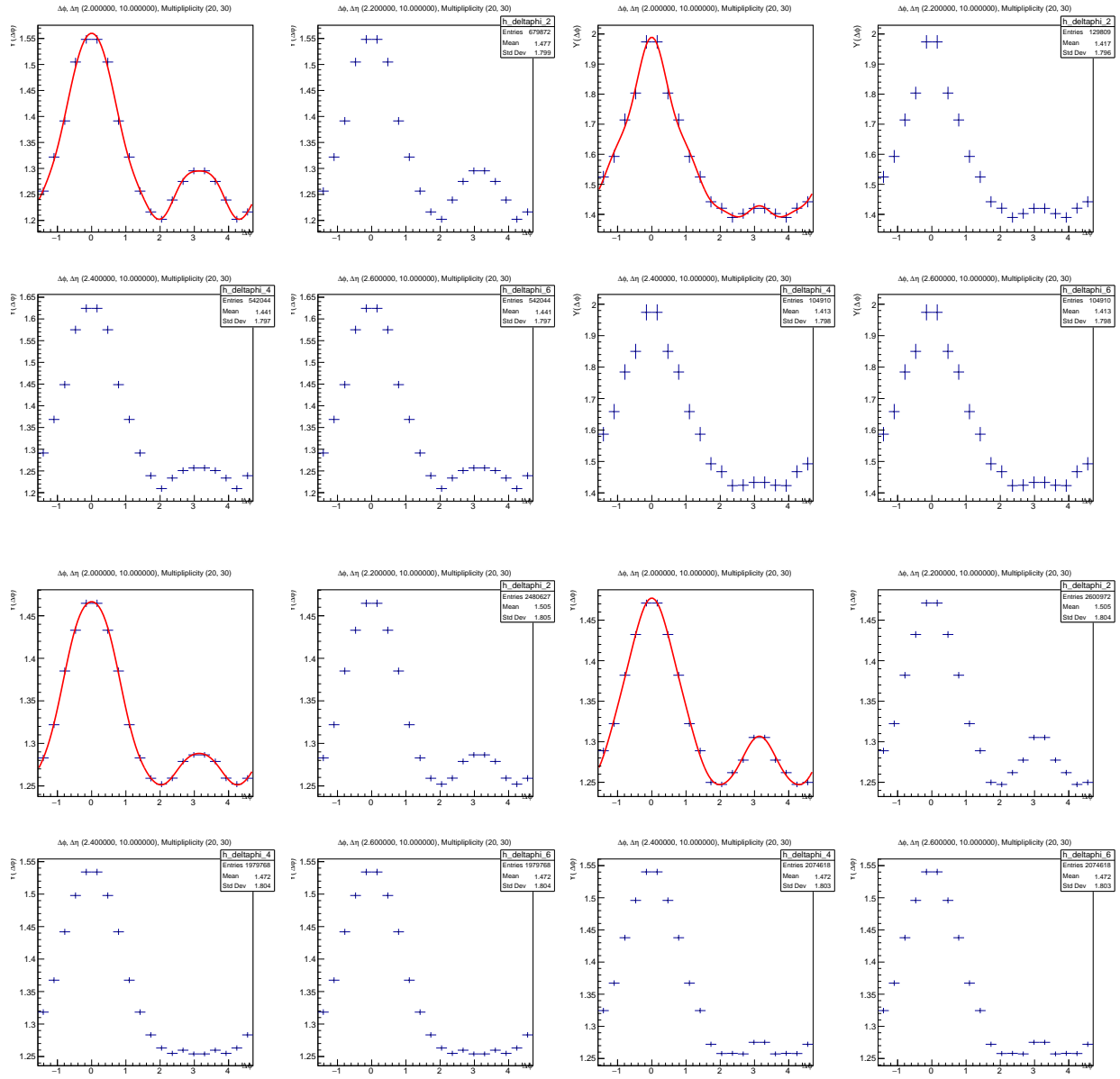


FIG. 70: Long range yield function for thrust axis. Top row is LEP1 and LEP2, bottom row PYTHIA8 and PYTHIA8 rope walk. Multiplicity 0-20.



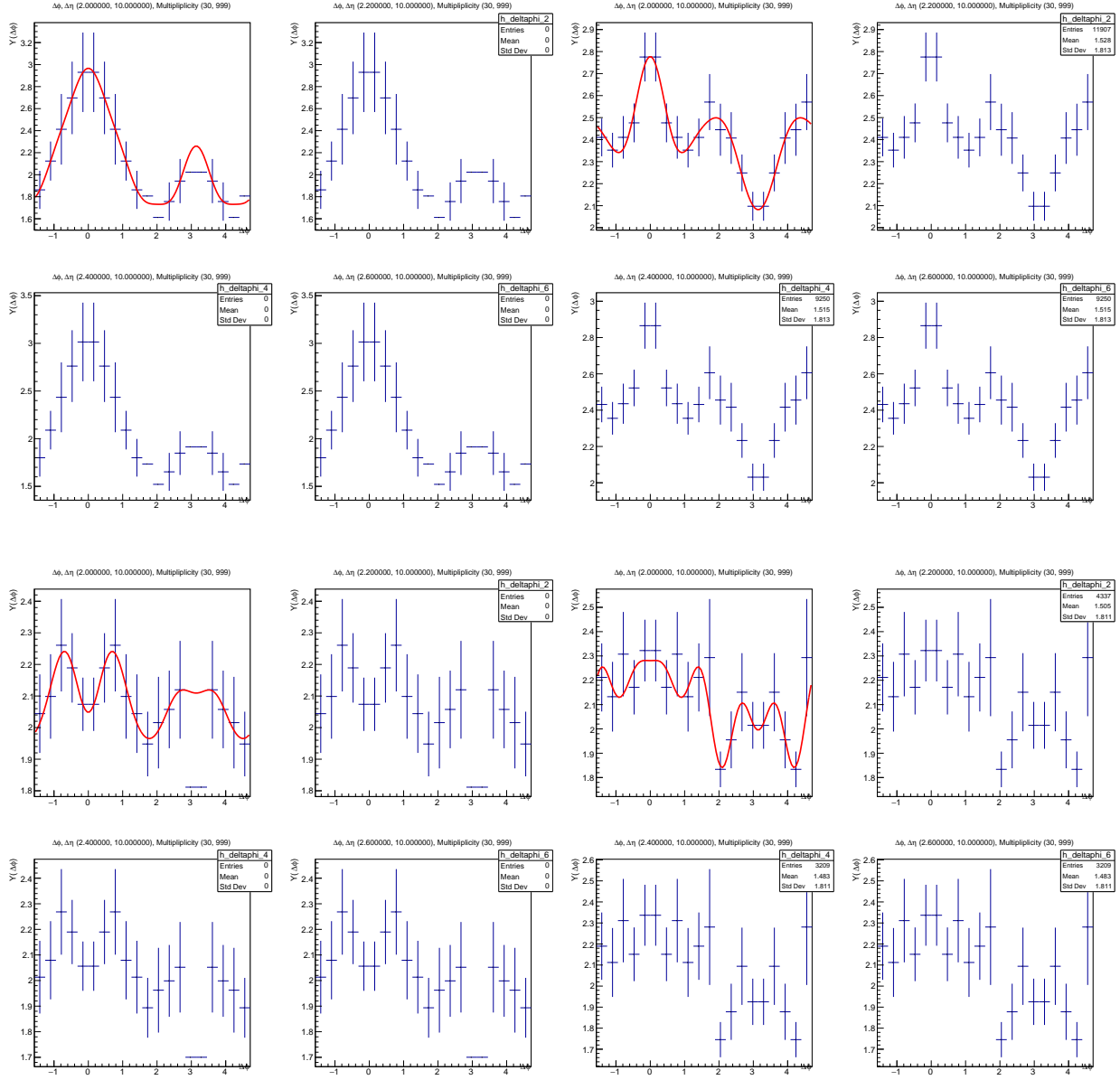


FIG. 72: Long range yield function for thrust axis. Top row is LEP1 and LEP2, bottom row PYTHIA8 and PYTHIA8 rope walk. Multiplicity 30-999.

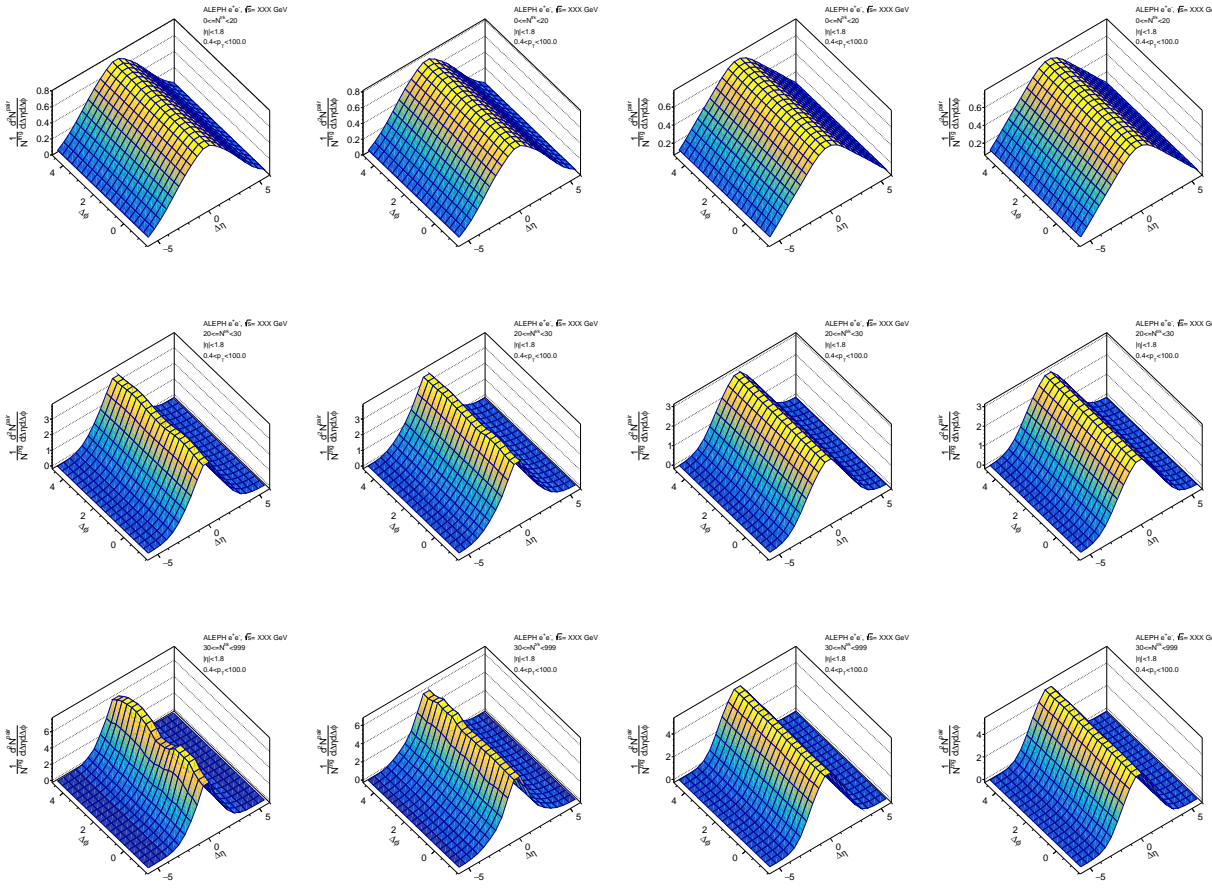


FIG. 73: Background function for WTA axis. Left to right: LEP1, LEP2, PYTHIA8, PYTHIA8 rope walk. Top to bottom: multiplicity 0-20, 20-30, 30-999.

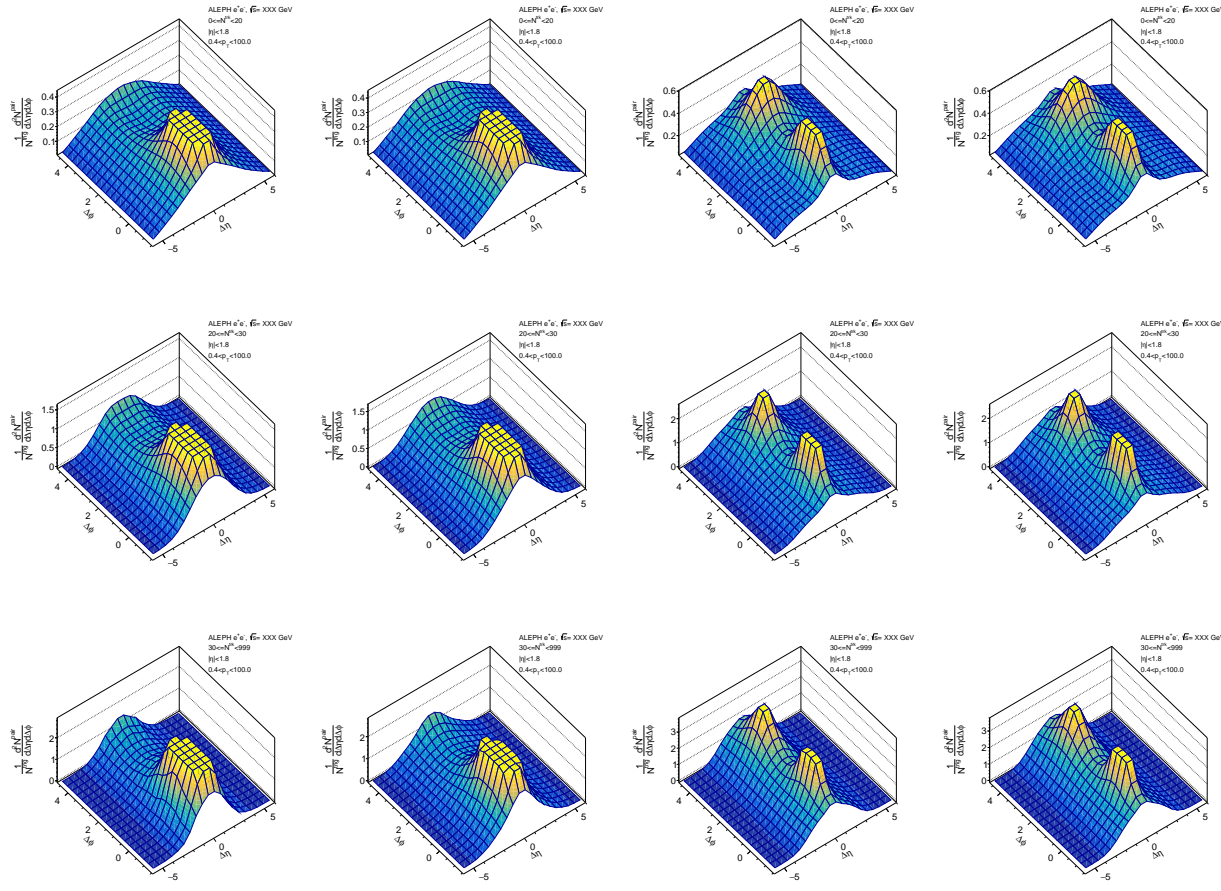


FIG. 74: Signal function for WTA axis. Left to right: LEP1, LEP2, PYTHIA8, PYTHIA8 rope walk. Top to bottom: multiplicity 0-20, 20-30, 30-999.

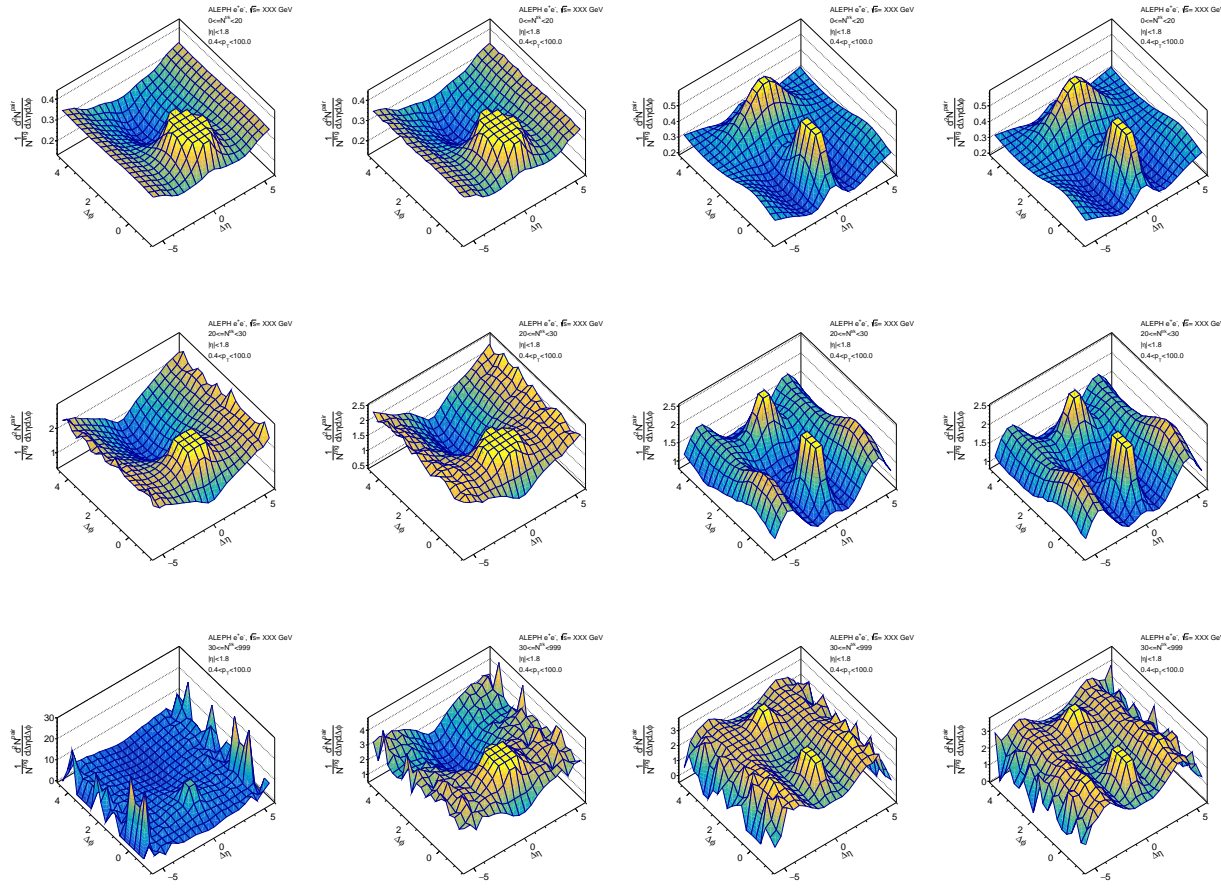


FIG. 75: Ratio function for WTA axis. Left to right: LEP1, LEP2, PYTHIA8, PYTHIA8 rope walk. Top to bottom: multiplicity 0-20, 20-30, 30-999. Note that the bottom left corner plot for LEP1 is zoomed out substantially from the plot to its right for LEP2 to show the difference in plotting that we may want to consider for the paper. The extremely high peaks at high $\Delta\eta$ and small $\Delta\phi$ are artifacts of the lack of a clear definition for the η cut in the WTA axis.

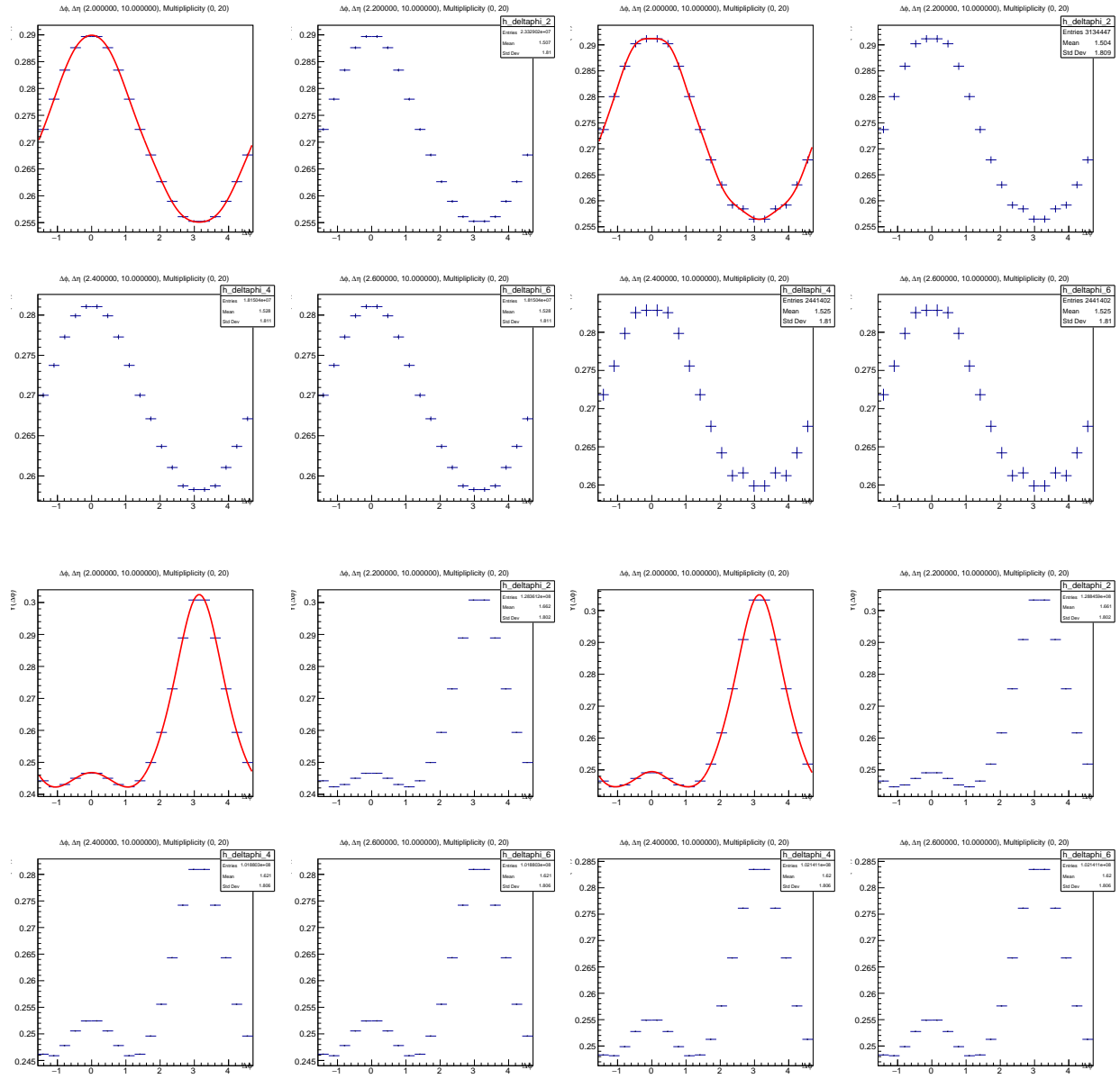


FIG. 76: Long range yield function for WTA axis. Top row is LEP1 and LEP2, bottom row PYTHIA8 and PYTHIA8 rope walk. Multiplicity 0-20.

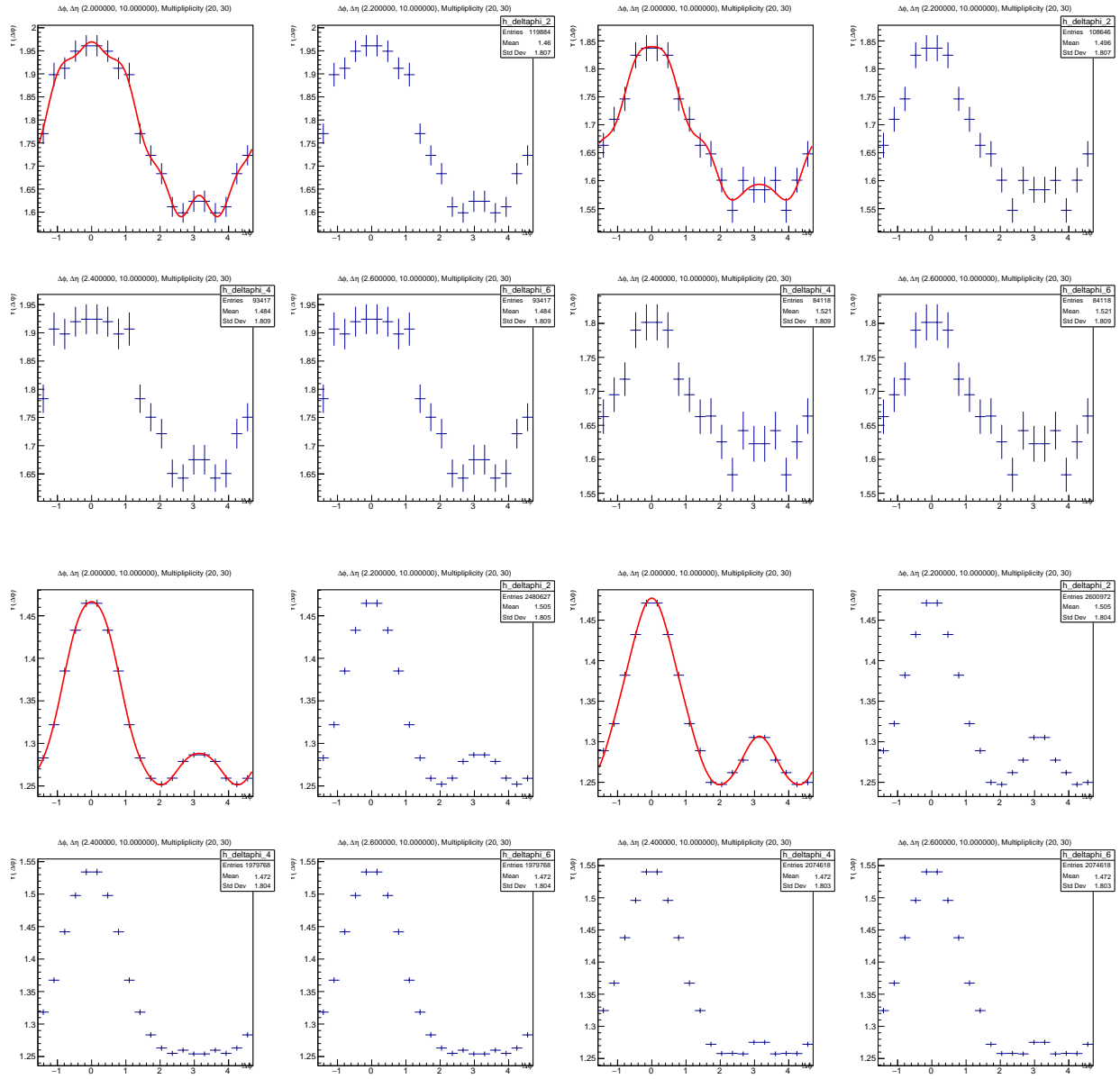


FIG. 77: Long range yield function for WTA axis. Top row is LEP1 and LEP2, bottom row PYTHIA8 and PYTHIA8 rope walk. Multiplicity 20-30.

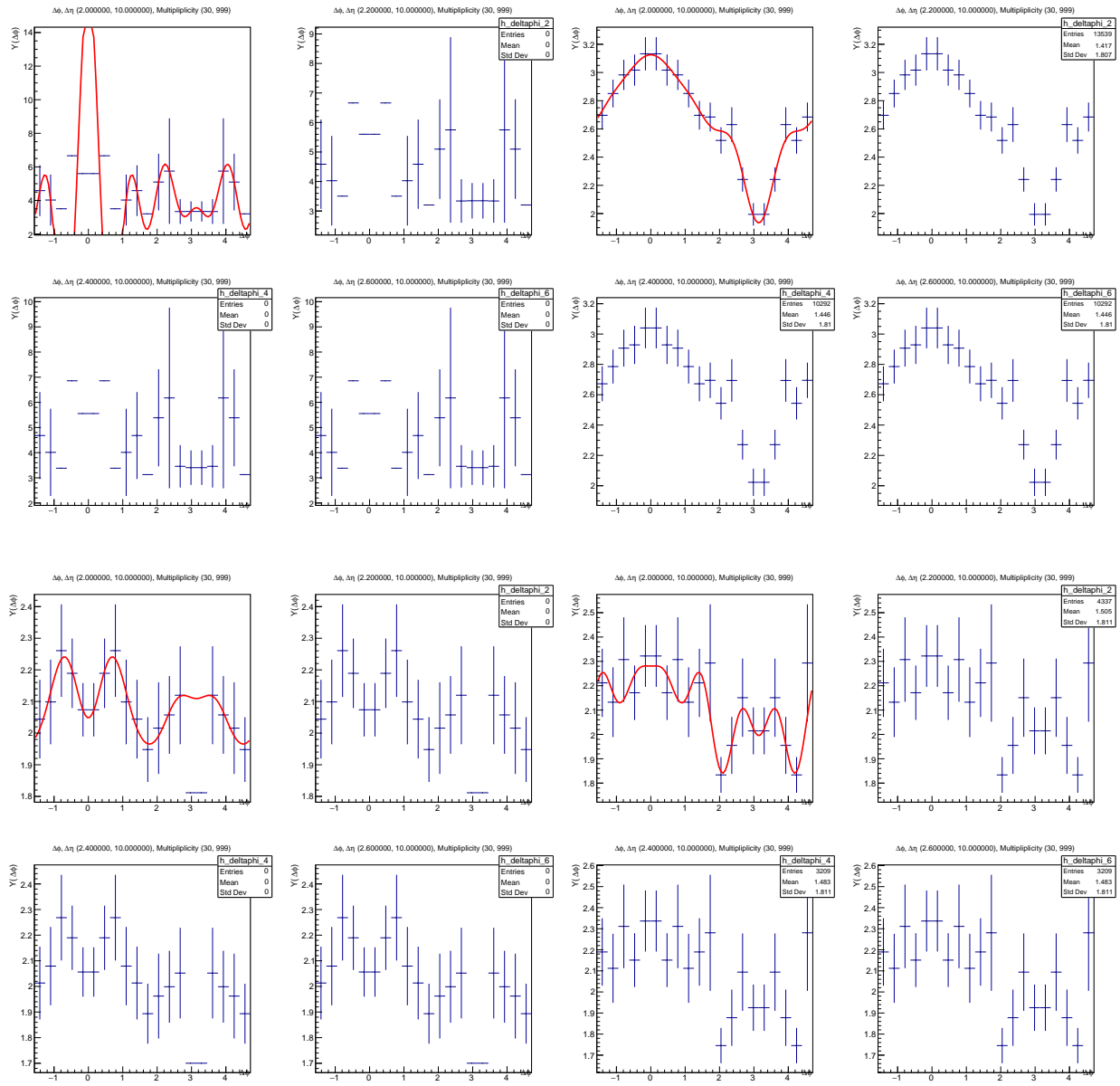


FIG. 78: Long range yield function for WTA axis. Top row is LEP1 and LEP2, bottom row PYTHIA8 and PYTHIA8 rope walk. Multiplicity 30-999.

B. Analysis for 2018.02.XX production

XII. SYSTEMATICAL UNCERTAINTIES

XIII. SUMMARY

The ALEPH archived data has been used to perform measurements of two-particle angular correlation functions for the first time.

XIV. APPENDIX

A. Cross-check analysis with independent macros

There are two independent analysis code used for correlation analyses and the cross check results are documented in this section. The cuts are specified in Table 1 and 2. The first column contains Anthony's analysis, the second contains Austin's cross-check, and the third contains the ratio of the two.

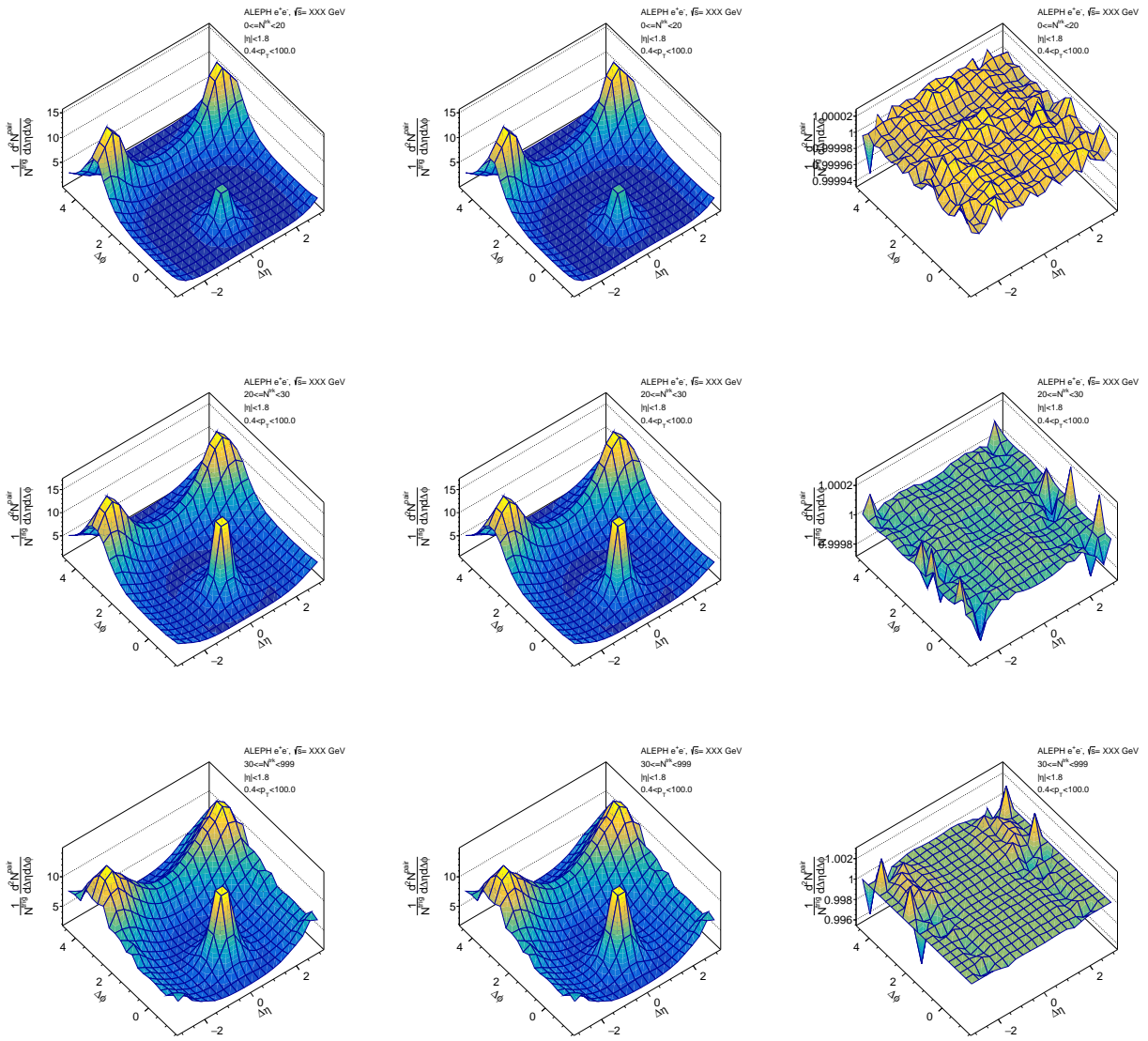


FIG. 79: Two particle correlation fuctions for the LEP1 data set analyzed in the beam axis.

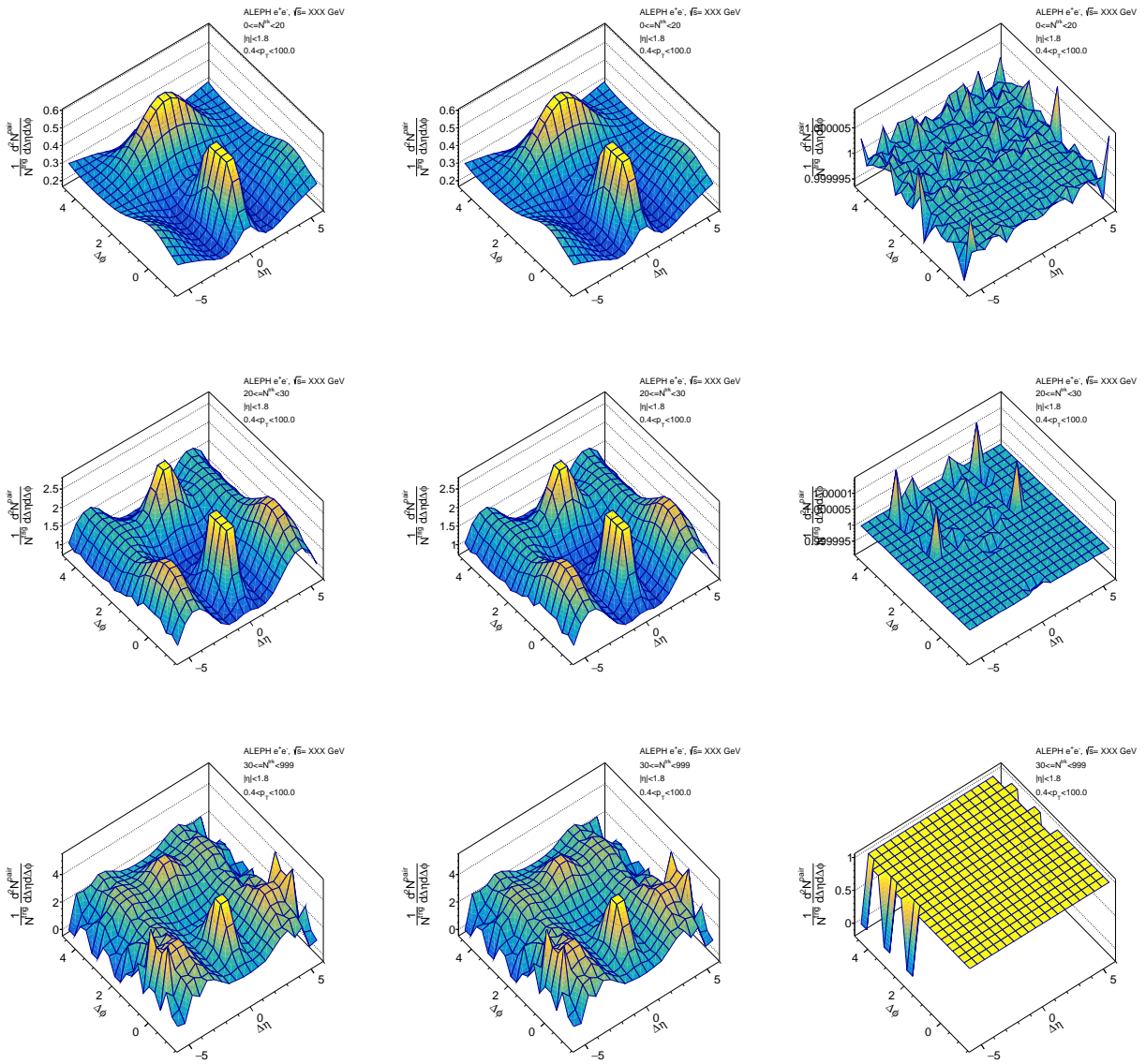


FIG. 80: Two particle correlation fuctions for the LEP1 data set analyzed in the thrust axis.

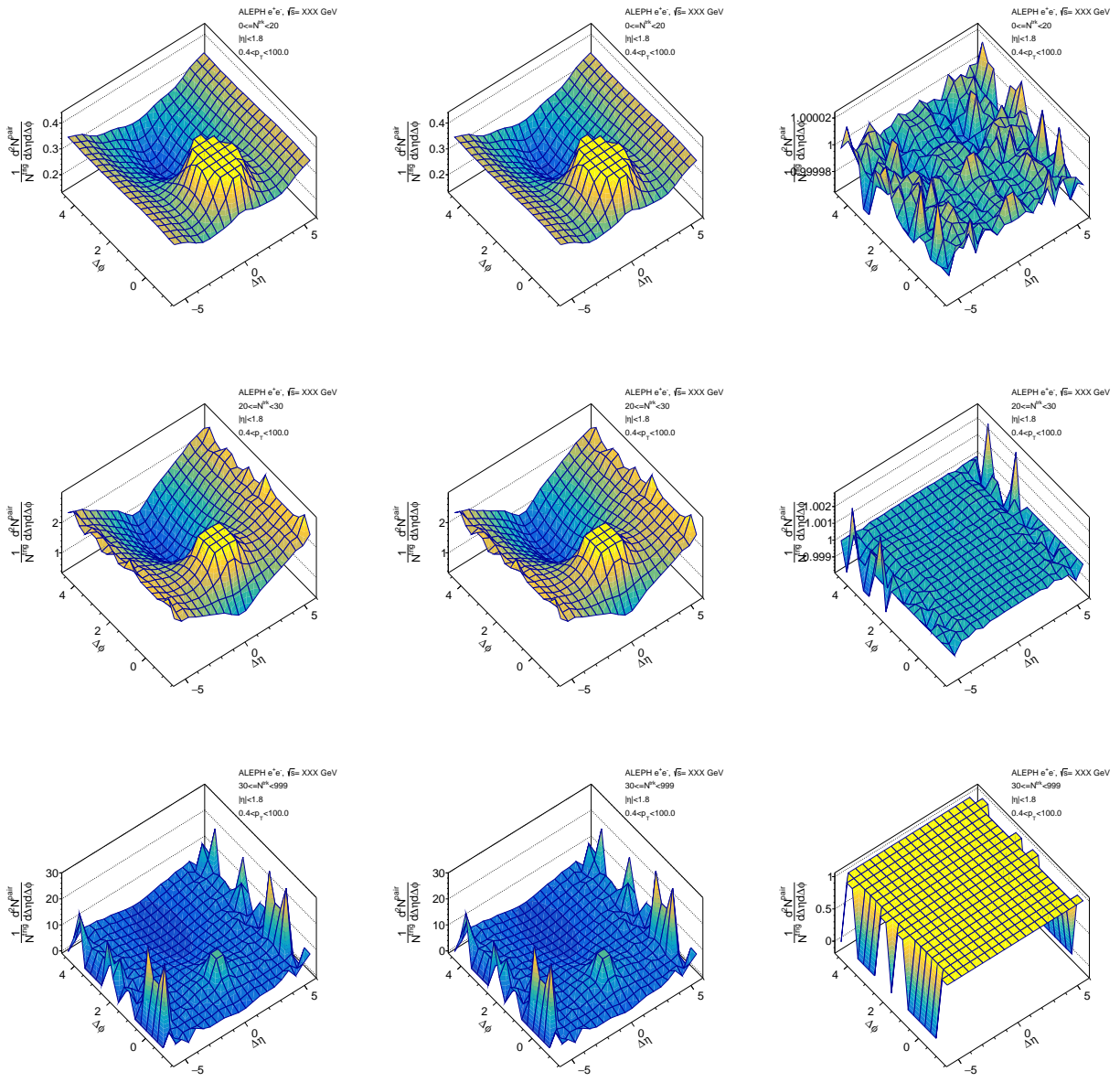


FIG. 81: Two particle correlation fuctions for the LEP1 data set analyzed in the WTA axis.

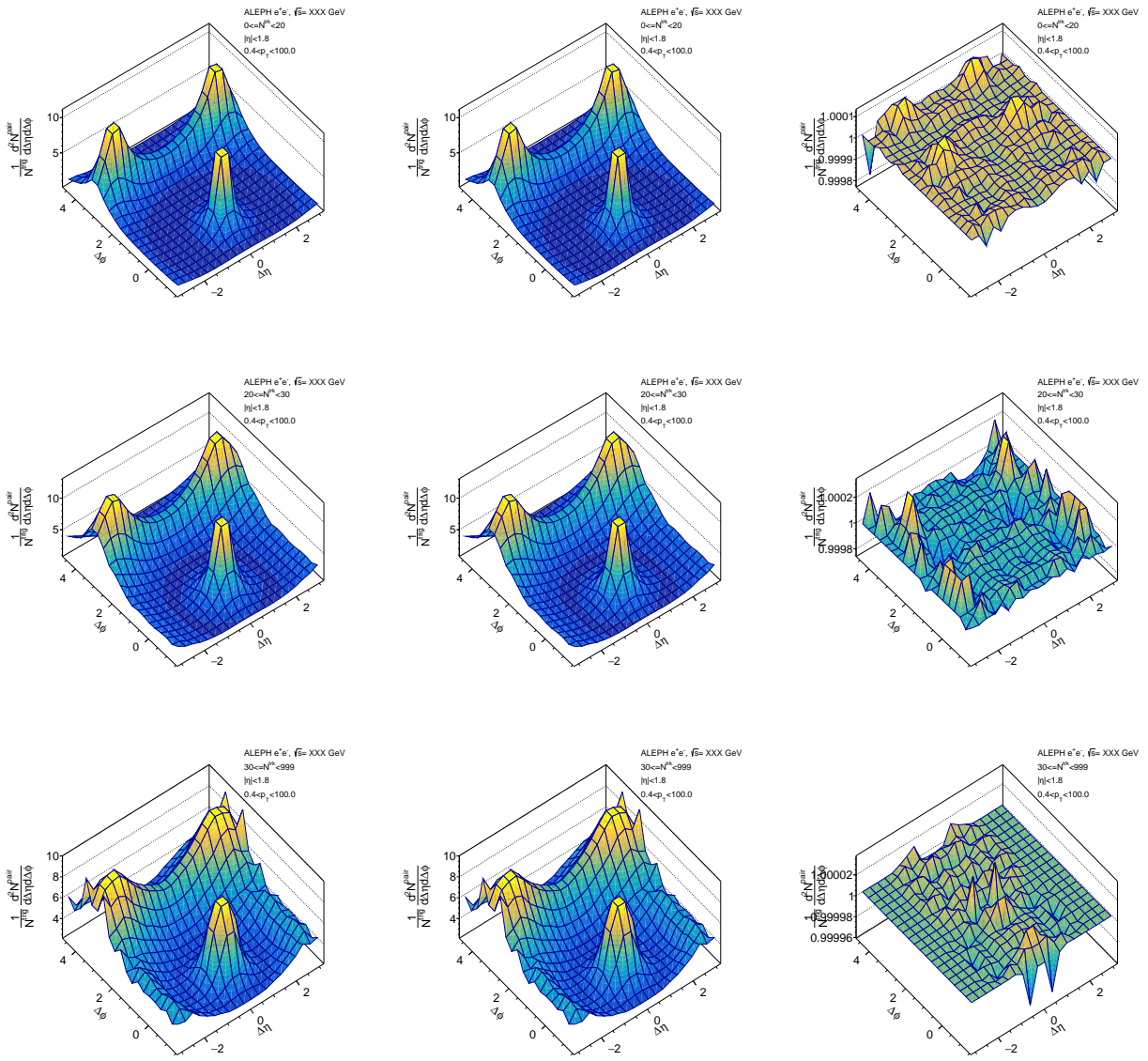


FIG. 82: Two particle correlation fuctions for the LEP2 data set analyzed in the beam axis.

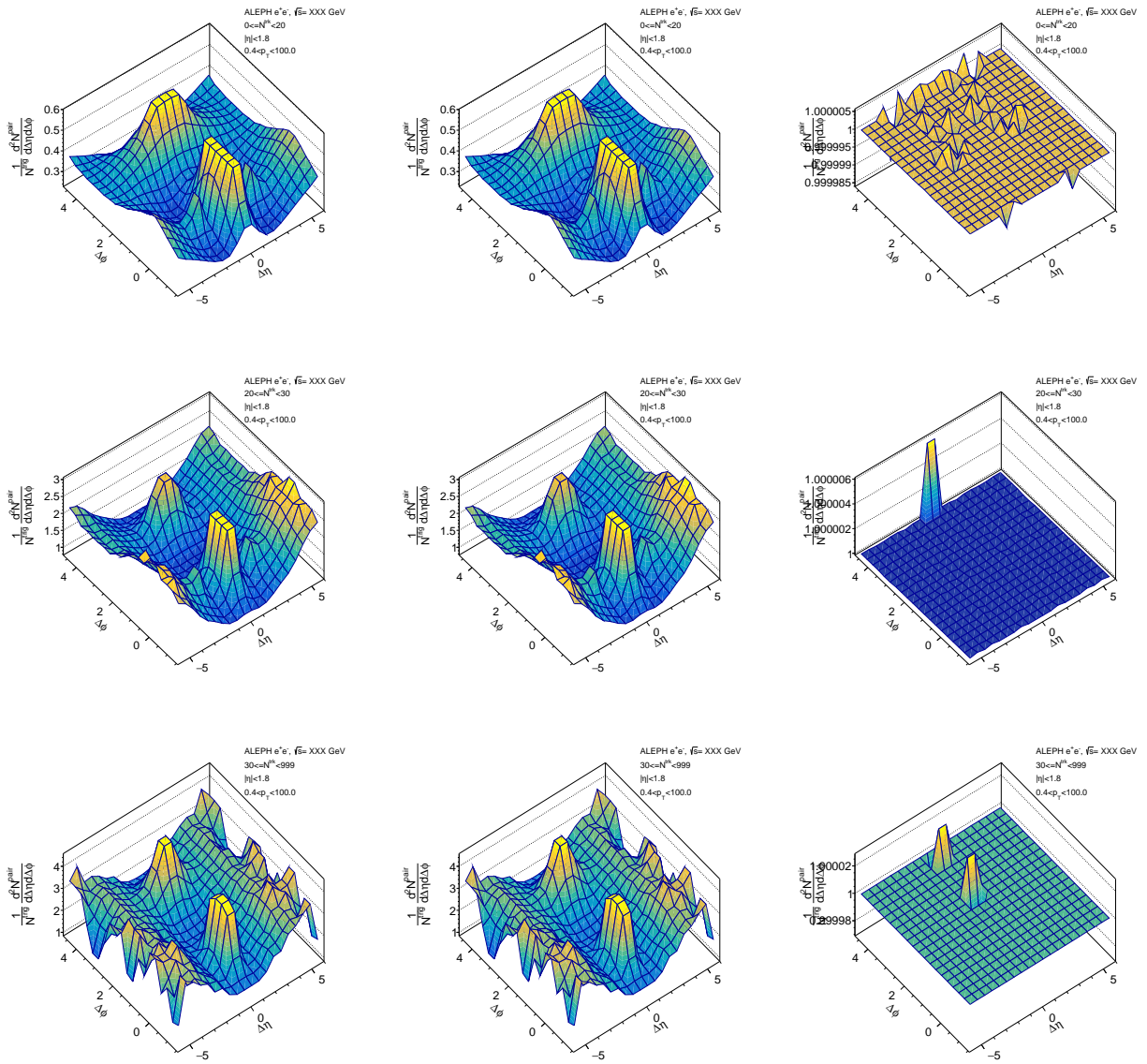
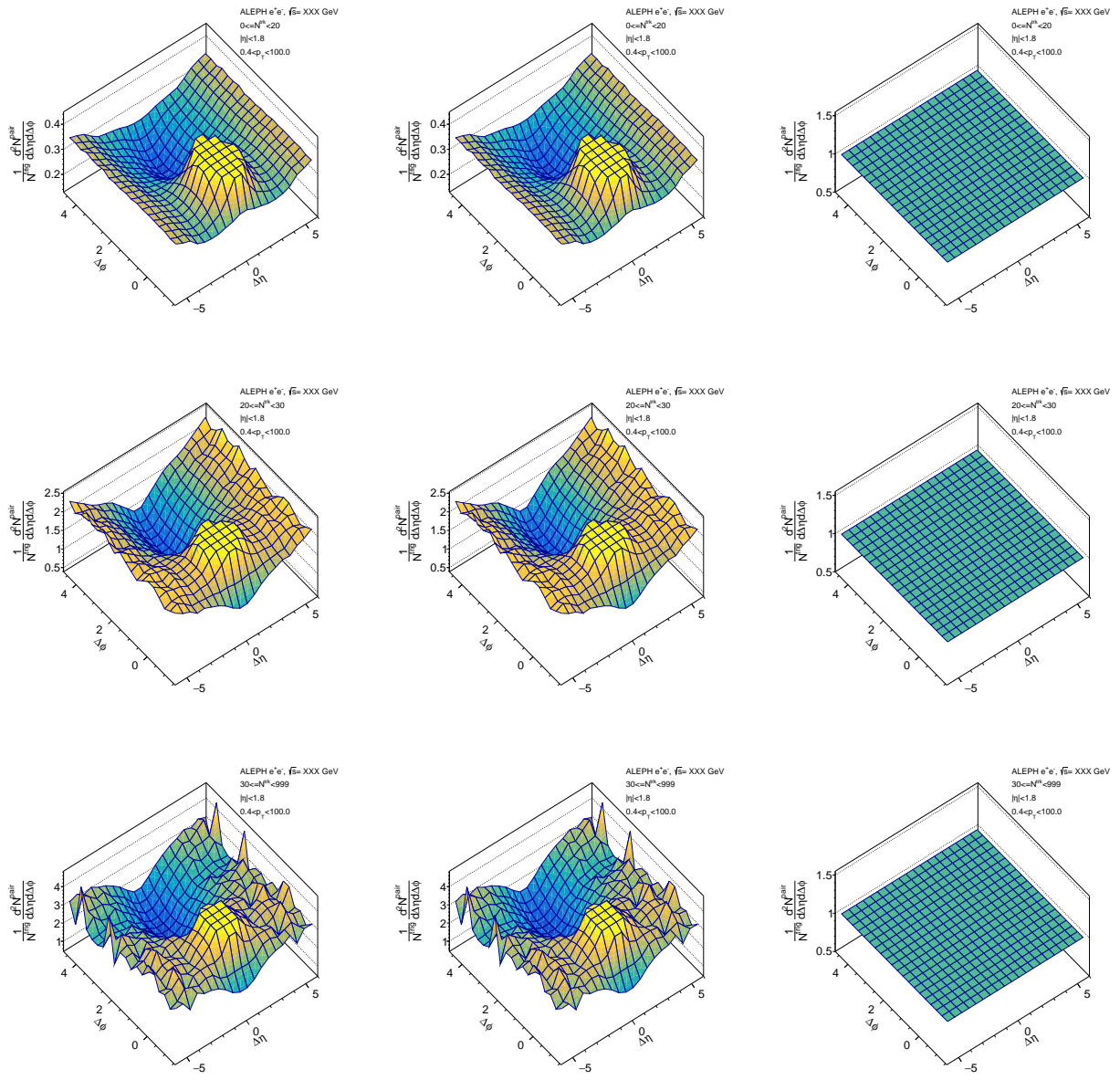


FIG. 83: Two particle correlation fuctions for the LEP2 data set analyzed in the thrust axis.



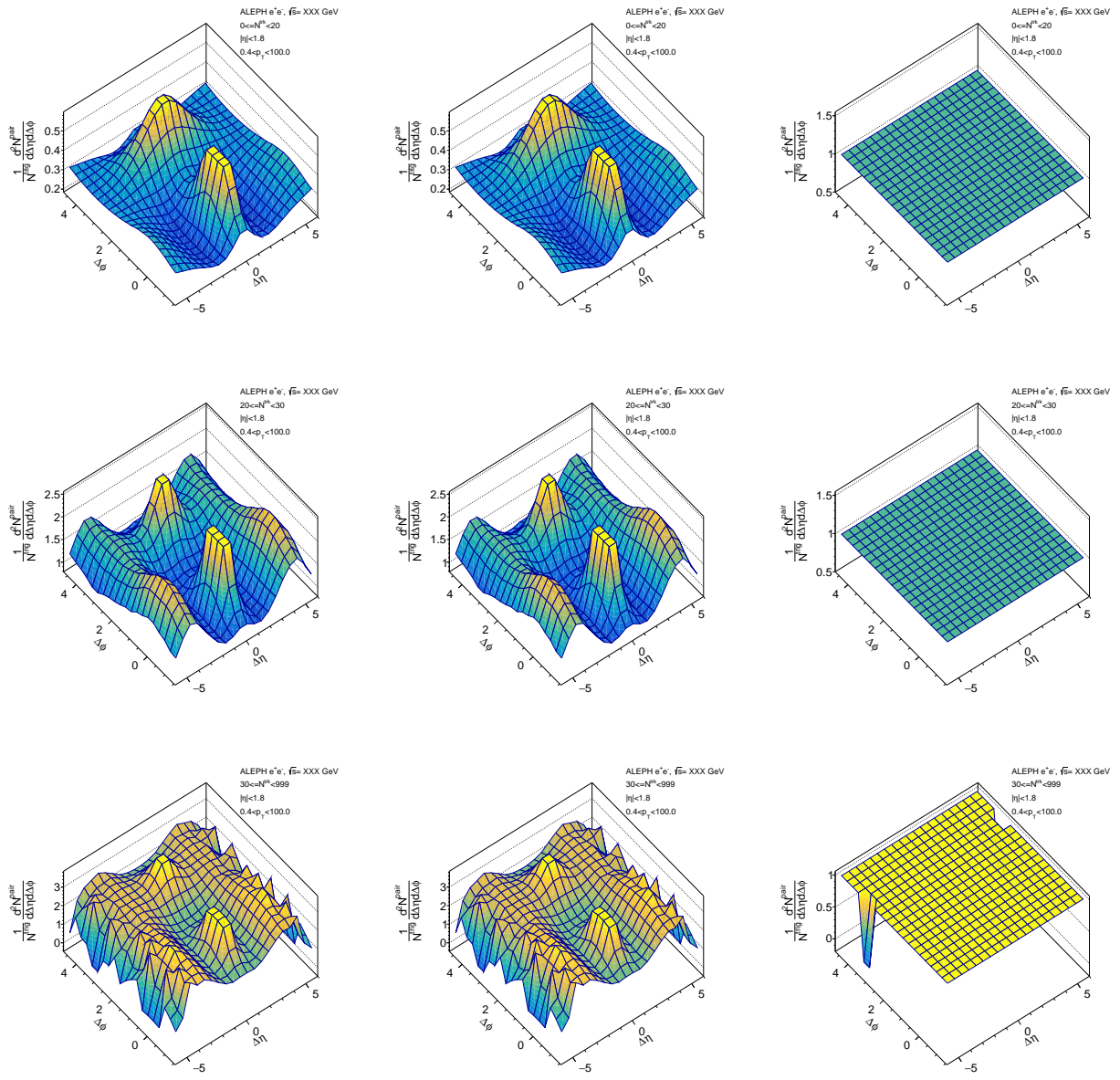


FIG. 85: Two particle correlation fuctions for the PYTHIA8 data set analyzed in the WTA axis.

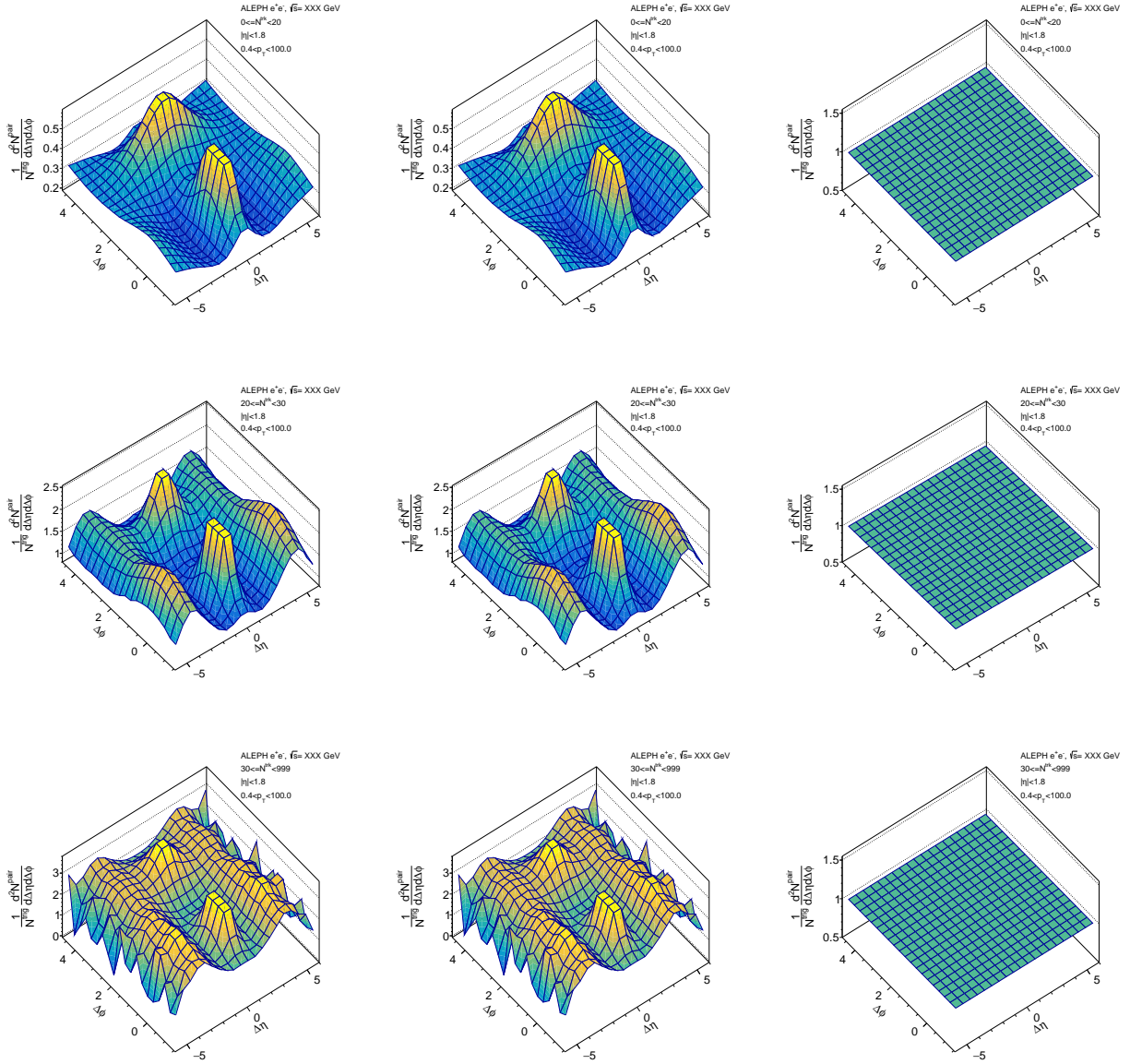


FIG. 86: Two particle correlation fuctions for the PYTHIA8 rope walk data set analyzed in the WTA axis.

B. Comparison of Raw Spectra

In this section, raw data spectra without event selection are compared to PYTHIA8 generator in order to study the possible noise, contribution of fake jets and fake tracks, and other possible experimental backgrounds. The results are shown in the figures below.

C. Raw data

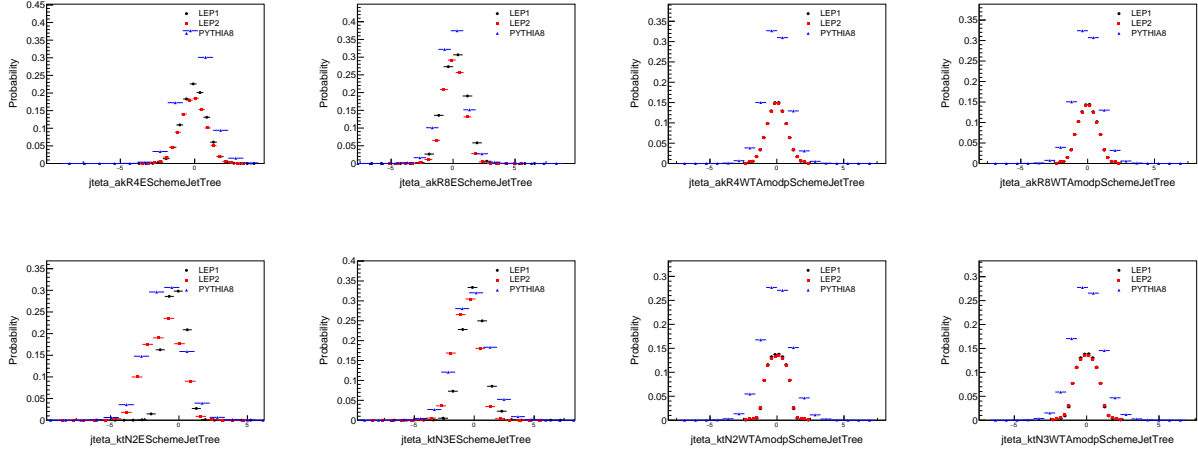


FIG. 87: Raw Data: LEP1, LEP2, Pythia8 no cuts. Jet η distributions. Top row: anti- k_t , left to right: $R = 0.4$, E scheme; $R = 0.8$, E scheme; $R = 0.4$, WTA mod p scheme; $R = 0.8$, WTA mod p scheme. Bottom row: k_t , left to right: $N = 2$, E scheme; $N = 3$, E scheme; $N = 2$, WTA mod p scheme; $N = 3$; WTA mod p scheme.

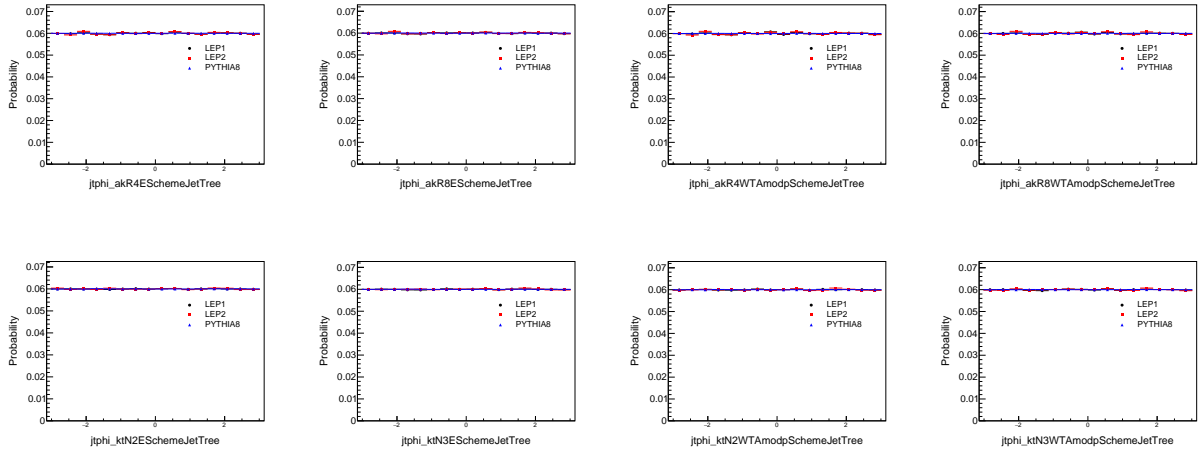


FIG. 88: Raw Data: LEP1, LEP2, Pythia8 no cuts. Jet ϕ distributions. Top row: anti- k_t , left to right: $R = 0.4$, E scheme; $R = 0.8$, E scheme; $R = 0.4$, WTA mod p scheme; $R = 0.8$, WTA mod p scheme. Bottom row: k_t , left to right: $N = 2$, E scheme; $N = 3$, E scheme; $N = 2$, WTA mod p scheme; $N = 3$; WTA mod p scheme.

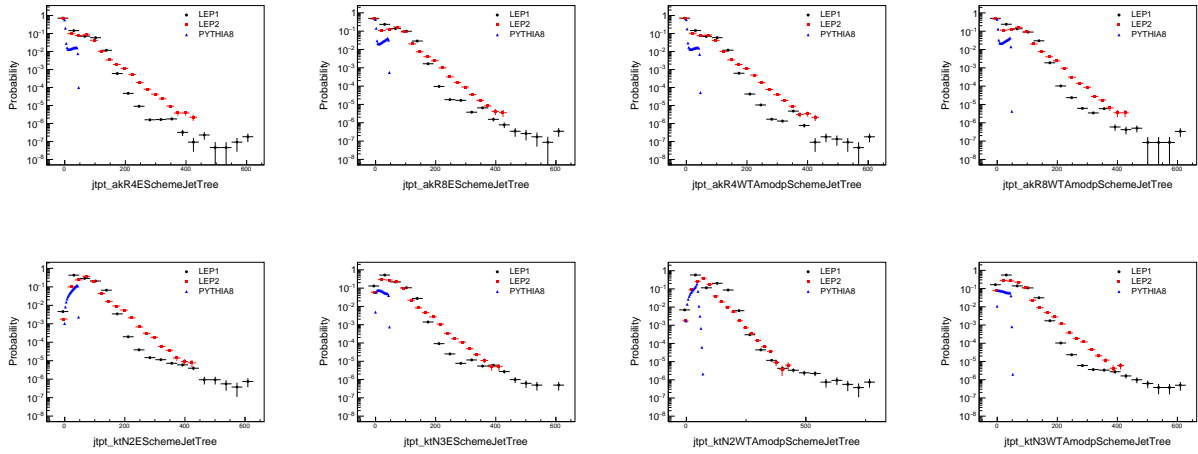


FIG. 89: Raw Data: LEP1, LEP2, Pythia8 no cuts. Jet p_t distributions. Top row: anti- k_t , left to right: $R = 0.4$, E scheme; $R = 0.8$, E scheme; $R = 0.4$, WTA mod p scheme; $R = 0.8$, WTA mod p scheme. Bottom row: k_t , left to right: $N = 2$, E scheme; $N = 3$, E scheme; $N = 2$, WTA mod p scheme; $N = 3$; WTA mod p scheme.

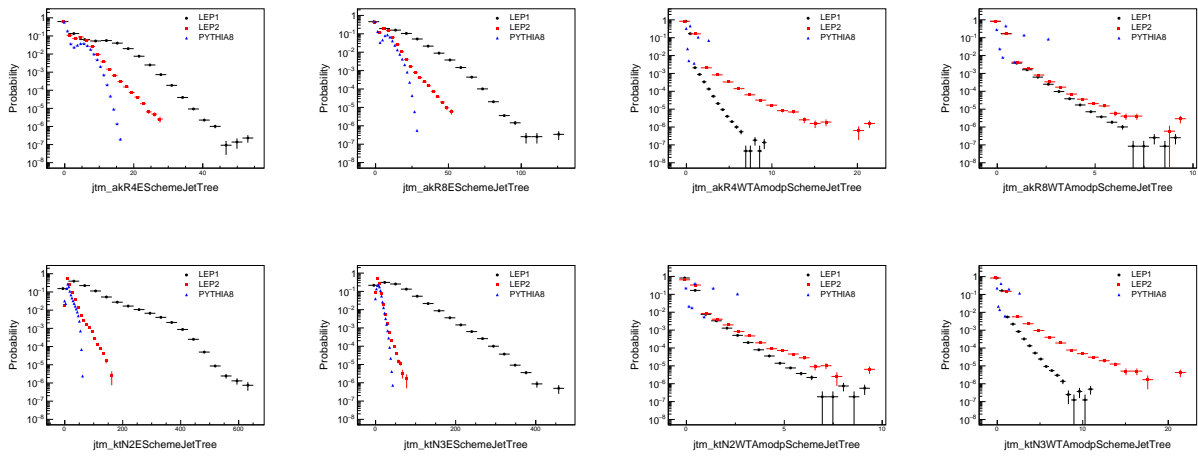


FIG. 90: Raw Data: LEP1, LEP2, Pythia8 no cuts. Jet mass distributions. Top row: anti- k_t , left to right: $R = 0.4$, E scheme; $R = 0.8$, E scheme; $R = 0.4$, WTA mod p scheme; $R = 0.8$, WTA mod p scheme. Bottom row: k_t , left to right: $N = 2$, E scheme; $N = 3$, E scheme; $N = 2$, WTA mod p scheme; $N = 3$; WTA mod p scheme.

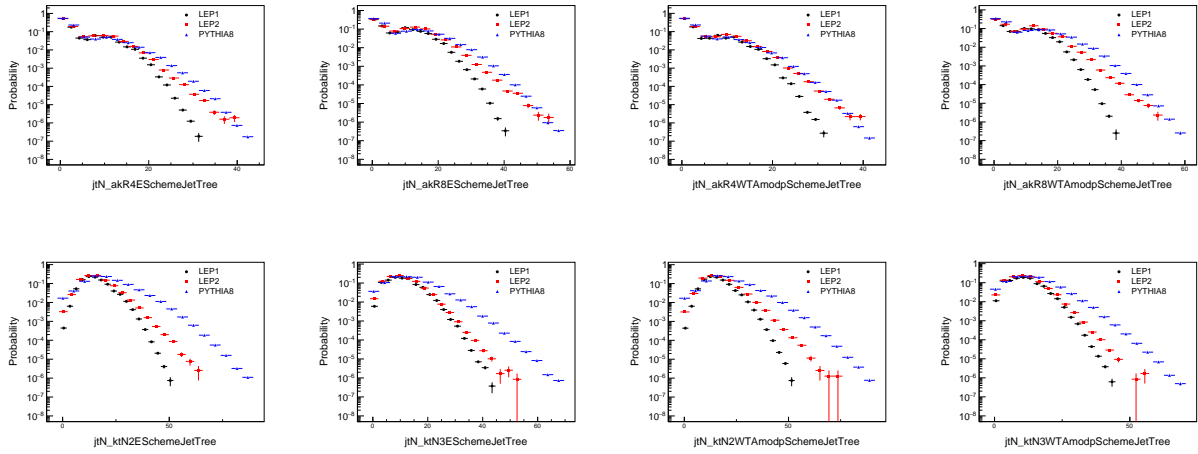


FIG. 91: Raw Data: LEP1, LEP2, Pythia8 no cuts. Jet N distributions. Top row: anti- k_t , left to right: $R = 0.4$, E scheme; $R = 0.8$, E scheme; $R = 0.4$, WTA mod p scheme; $R = 0.8$, WTA mod p scheme. Bottom row: k_t , left to right: $N = 2$, E scheme; $N = 3$, E scheme; $N = 2$, WTA mod p scheme; $N = 3$; WTA mod p scheme.

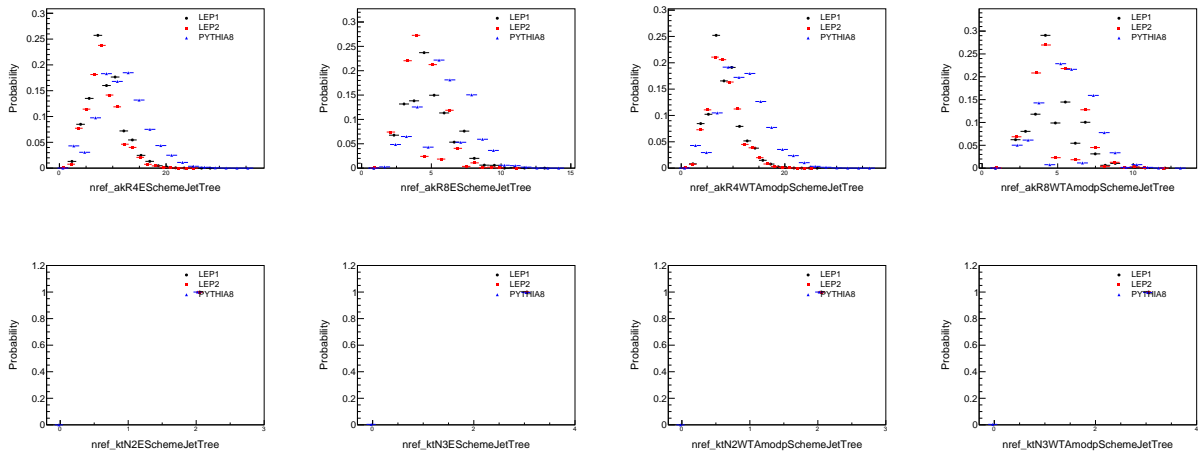


FIG. 92: Raw Data: LEP1, LEP2, Pythia8 no cuts. Jet nref distributions. Top row: anti- k_t , left to right: $R = 0.4$, E scheme; $R = 0.8$, E scheme; $R = 0.4$, WTA mod p scheme; $R = 0.8$, WTA mod p scheme. Bottom row: k_t , left to right: $N = 2$, E scheme; $N = 3$, E scheme; $N = 2$, WTA mod p scheme; $N = 3$; WTA mod p scheme.

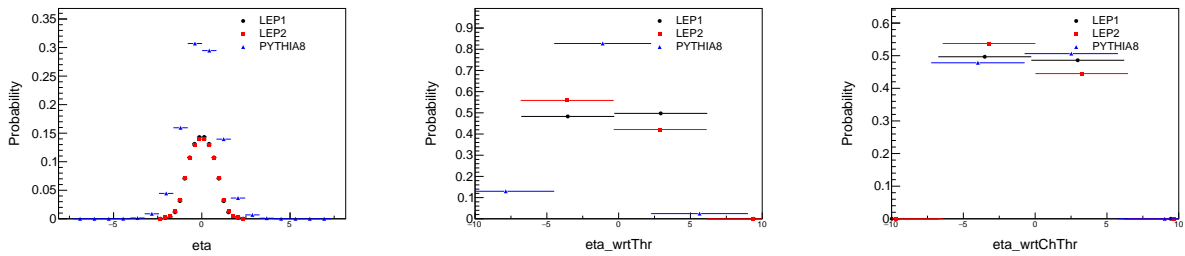


FIG. 93: Raw Data: LEP1, LEP2, Pythia8 no cuts. η distributions. Left to right: η ; η with respect to thrust axis; η with respect to charged thrust axis.

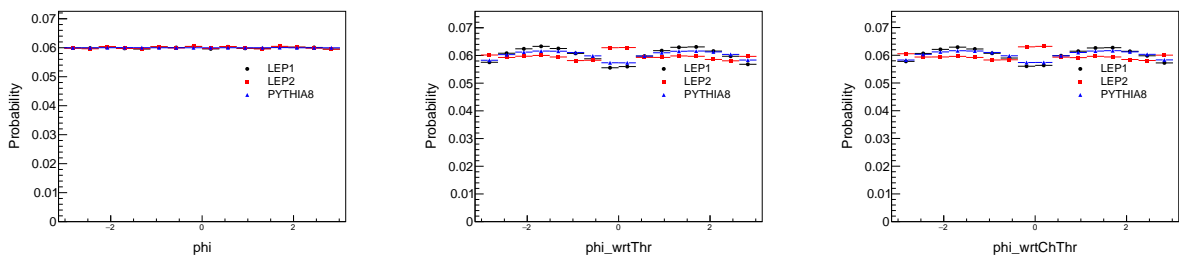


FIG. 94: Raw Data: LEP1, LEP2, Pythia8 no cuts. ϕ distributions. Left to right: ϕ ; ϕ with respect to thrust axis; ϕ with respect to charged thrust axis.

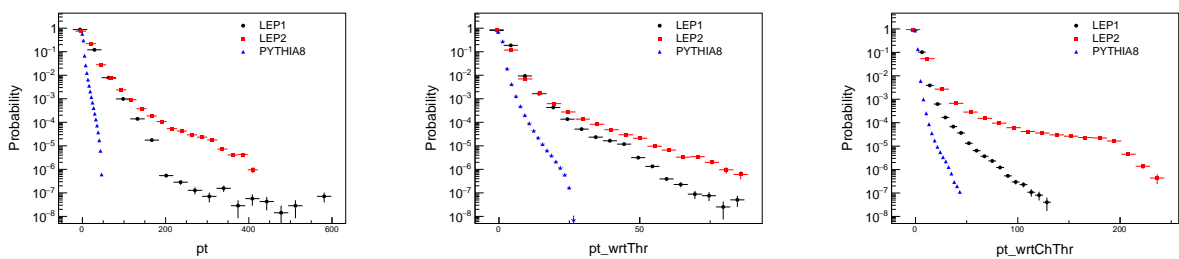


FIG. 95: Raw Data: LEP1, LEP2, Pythia8 no cuts. p_t distributions. Left to right: p_t ; p_t with respect to thrust axis; p_t with respect to charged thrust axis.

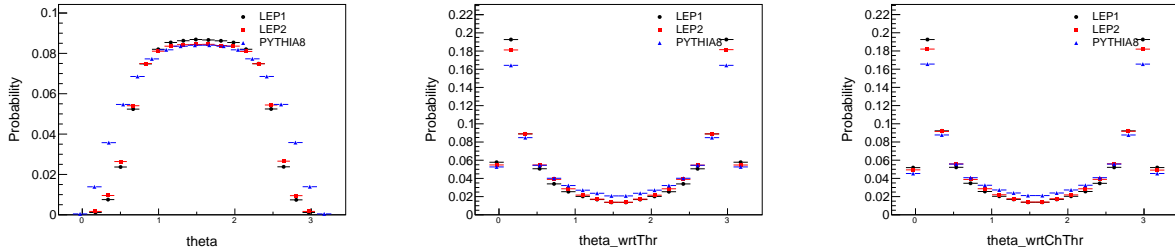


FIG. 96: Raw Data: LEP1, LEP2, Pythia8 no cuts. θ distributions. Left to right: θ ; θ with respect to thrust axis; θ with respect to charged thrust axis.

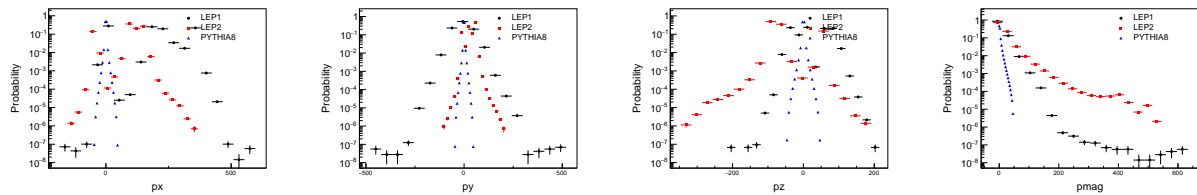


FIG. 97: Raw Data: LEP1, LEP2, Pythia8 no cuts. p_x , p_y , p_z , and $|\vec{p}|$ distributions.

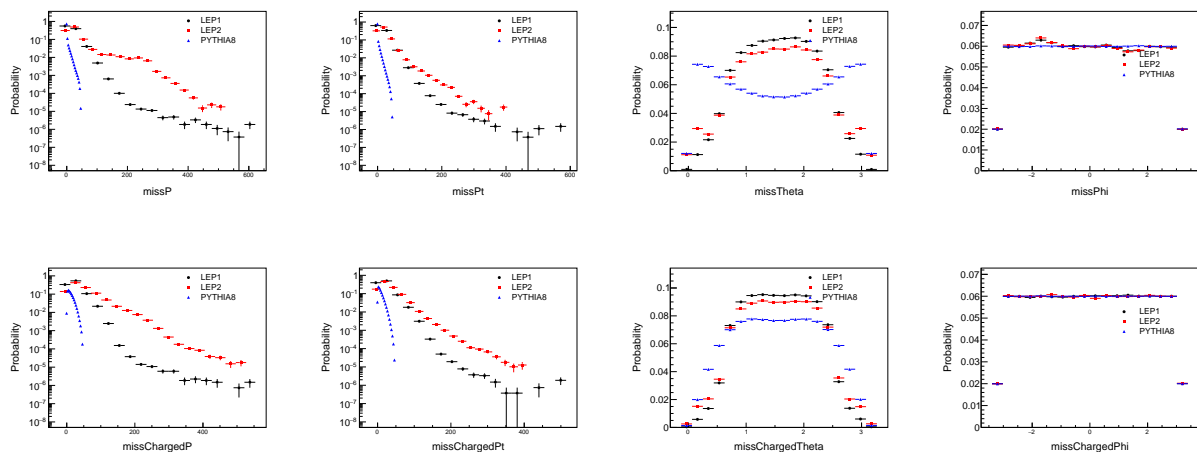


FIG. 98: Raw Data: LEP1, LEP2, Pythia8 no cuts. missing quantities distribution. Left to right: missing P ; missing p_t ; missing θ ; missing ϕ . Top to bottom: All; charged.

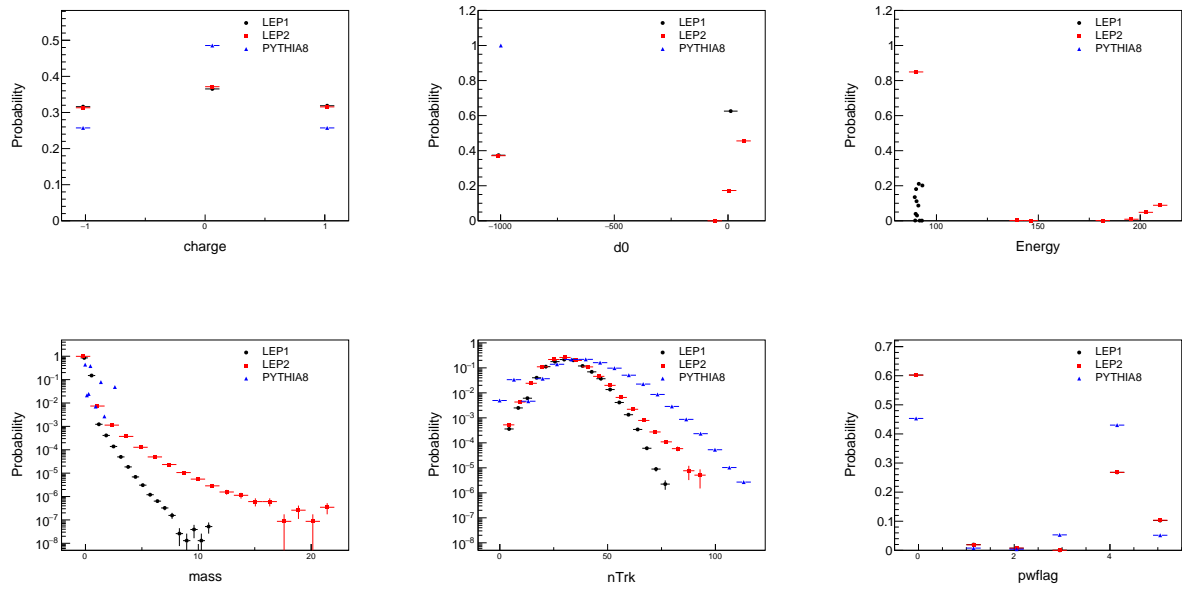


FIG. 99: Left to right: Top row: Raw Data: LEP1, LEP2, Pythia8 no cuts. charge, d_0 , and energy distributions. Bottom row: NoCut mass, particle multiplicity, and pwflag distributions.

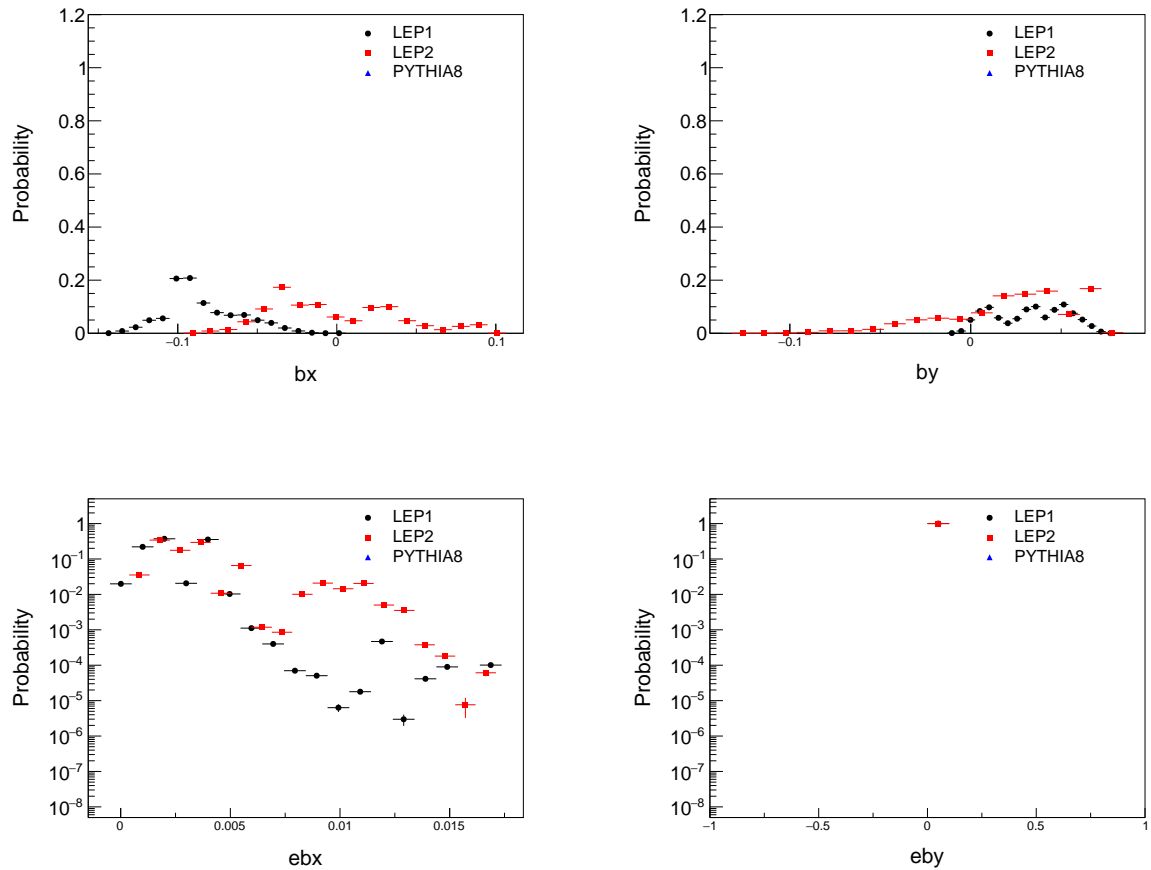


FIG. 100: Top row: Raw Data: LEP1, LEP2, Pythia8 no cuts. beamspot x and y . Bottom row: Error in beamspot x and y .

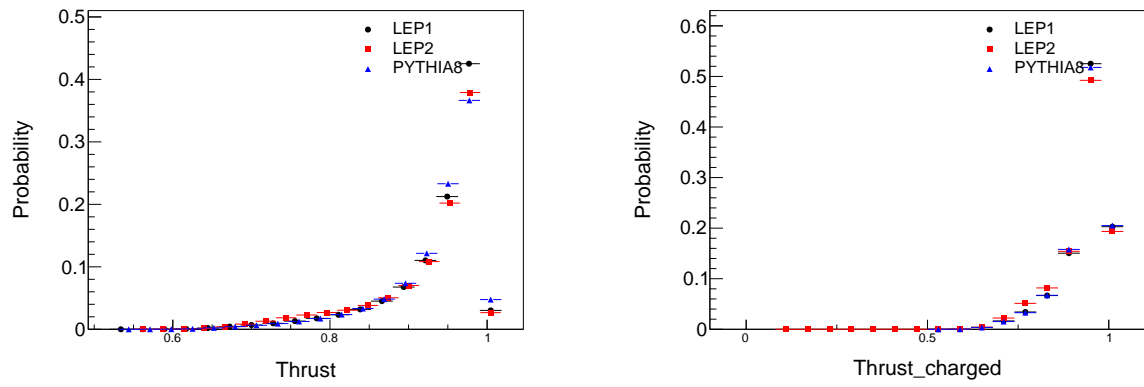


FIG. 101: Left: Raw Data: LEP1, LEP2, Pythia8 no cuts. thrust distribution. Right: Raw Data: LEP1, LEP2, Pythia8 no cuts. charged thrust distribution.

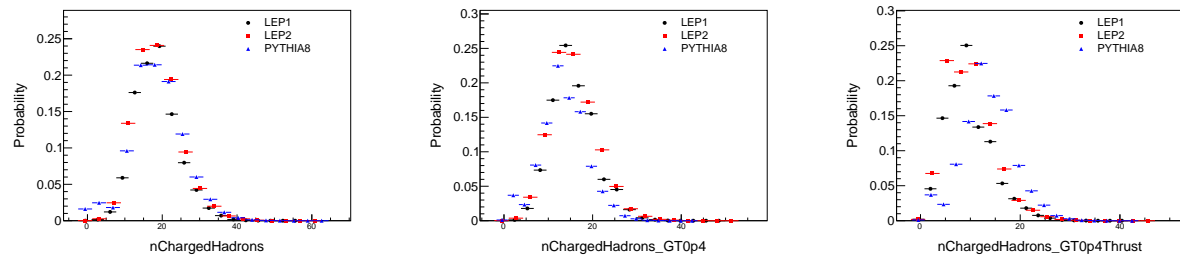


FIG. 102: Raw Data: LEP1, LEP2, Pythia8 no cuts. charged hadron multiplicity distributions. Left to right: charged hadron multiplicity; charged hadron multiplicity (GT0p4); charged hadron multiplicity (GT0p4Thrust).

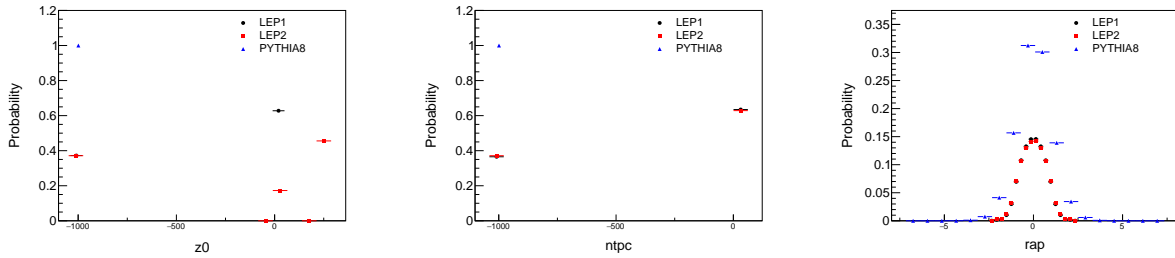


FIG. 103: Left: Raw Data: LEP1, LEP2, Pythia8 no cuts. z_0 distribution. Center: Raw Data: LEP1, LEP2, Pythia8 no cuts. TPC hits distribution. Right: NoCut rapidity distribution.

- [1] CMS Collaboration, “Observation of Long-Range Near-Side Angular Correlations in Proton-Proton Collisions at the LHC”, *JHEP* **09** (2010) 091, doi:10.1007/JHEP09(2010)091, [arXiv:1009.4122](https://arxiv.org/abs/1009.4122).
- [2] CMS Collaboration, “Observation of long-range near-side angular correlations in proton-lead collisions at the LHC”, *Phys. Lett. B* **718** (2013) 795–814, doi:10.1016/j.physletb.2012.11.025, [arXiv:1210.5482](https://arxiv.org/abs/1210.5482).
- [3] ALICE Collaboration, “Long-range angular correlations on the near and away side in p -Pb collisions at $\sqrt{s_{NN}} = 5.02$ TeV”, *Phys. Lett. B* **719** (2013) 29–41, doi:10.1016/j.physletb.2013.01.012, [arXiv:1212.2001](https://arxiv.org/abs/1212.2001).
- [4] ATLAS Collaboration, “Observation of Associated Near-Side and Away-Side Long-Range Correlations in $\sqrt{s_{NN}}=5.02$ TeV Proton-Lead Collisions with the ATLAS Detector”, *Phys. Rev. Lett.* **110** (2013), no. 18, 182302, doi:10.1103/PhysRevLett.110.182302, [arXiv:1212.5198](https://arxiv.org/abs/1212.5198).
- [5] ALICE Collaboration, “Elliptic flow of charged particles in Pb-Pb collisions at 2.76 TeV”, *Phys. Rev. Lett.* **105** (2010) 252302, doi:10.1103/PhysRevLett.105.252302, [arXiv:1011.3914](https://arxiv.org/abs/1011.3914).
- [6] CMS Collaboration, “Centrality dependence of dihadron correlations and azimuthal anisotropy harmonics in PbPb collisions at $\sqrt{s_{NN}} = 2.76$ TeV”, *Eur. Phys. J. C* **72** (2012)

- 2012, doi:10.1140/epjc/s10052-012-2012-3, [arXiv:1201.3158](#).
- [7] B. B. Back et al., “The PHOBOS perspective on discoveries at RHIC”, *Nucl. Phys.* **A757** (2005) 28–101, doi:10.1016/j.nuclphysa.2005.03.084, [arXiv:nucl-ex/0410022](#).
- [8] BRAHMS Collaboration, “Quark gluon plasma and color glass condensate at RHIC? The Perspective from the BRAHMS experiment”, *Nucl. Phys.* **A757** (2005) 1–27, doi:10.1016/j.nuclphysa.2005.02.130, [arXiv:nucl-ex/0410020](#).
- [9] PHENIX Collaboration, “Formation of dense partonic matter in relativistic nucleus-nucleus collisions at RHIC: Experimental evaluation by the PHENIX collaboration”, *Nucl. Phys.* **A757** (2005) 184–283, doi:10.1016/j.nuclphysa.2005.03.086, [arXiv:nucl-ex/0410003](#).
- [10] STAR Collaboration, “Experimental and theoretical challenges in the search for the quark gluon plasma: The STAR Collaboration’s critical assessment of the evidence from RHIC collisions”, *Nucl. Phys.* **A757** (2005) 102–183, doi:10.1016/j.nuclphysa.2005.03.085, [arXiv:nucl-ex/0501009](#).
- [11] J.-Y. Ollitrault, “Anisotropy as a signature of transverse collective flow”, *Phys. Rev.* **D46** (1992) 229–245, doi:10.1103/PhysRevD.46.229.
- [12] B. Alver and G. Roland, “Collision geometry fluctuations and triangular flow in heavy-ion collisions”, *Phys. Rev.* **C81** (2010) 054905, doi:10.1103/PhysRevC.81.054905, [arXiv:1003.0194](#). [Erratum: *Phys. Rev.* C82, 039903(2010)].
- [13] A. Bzdak, B. Schenke, P. Tribedy, and R. Venugopalan, “Initial state geometry and the role of hydrodynamics in proton-proton, proton-nucleus and deuteron-nucleus collisions”, *Phys. Rev.* **C87** (2013), no. 6, 064906, doi:10.1103/PhysRevC.87.064906, [arXiv:1304.3403](#).
- [14] K. Dusling, W. Li, and B. Schenke, “Novel collective phenomena in high-energy proton?proton and proton?nucleus collisions”, *Int. J. Mod. Phys.* **E25** (2016), no. 01, 1630002, doi:10.1142/S0218301316300022, [arXiv:1509.07939](#).
- [15] STAR Collaboration, “Inclusive charged hadron elliptic flow in Au + Au collisions at $\sqrt{s_{NN}} = 7.7 - 39$ GeV”, *Phys. Rev.* **C86** (2012) 054908, doi:10.1103/PhysRevC.86.054908, [arXiv:1206.5528](#).
- [16] F. Gelis, E. Iancu, J. Jalilian-Marian, and R. Venugopalan, “The Color Glass Condensate”, *Ann. Rev. Nucl. Part. Sci.* **60** (2010) 463–489, doi:10.1146/annurev.nucl.010909.083629, [arXiv:1002.0333](#).

- [17] K. Dusling and R. Venugopalan, “Comparison of the color glass condensate to dihadron correlations in proton-proton and proton-nucleus collisions”, *Phys. Rev.* **D87** (2013), no. 9, 094034, doi:10.1103/PhysRevD.87.094034, [arXiv:1302.7018](https://arxiv.org/abs/1302.7018).